# DESIGN, FABRICATION, AND CHARACTERIZATION OF ORGANIC ELECTRONIC DEVICES FOR THERMOELECTRIC APPLICATIONS

Joshua David Yablonski

A dissertation submitted to the faculty at the University of North Carolina at Chapel Hill in partial fulfillment of the requirements for the degree of Doctor of Philosophy in the Department of Chemistry.

Chapel Hill
2015

Approved by:

Wei You

Joseph Templeton

Cynthia Schauer

Matthew Lockett

John Papanikolas

## ABSTRACT

Joshua David Yablonski: Design, Fabrication, and Characterization of Organic Electronic Devices for Thermoelectric Applications
(Under the direction of Wei You)

Thermoelectric devices are an emerging application for conducting organic materials. Translating between heat and electricity, these materials could help to meet the energy needs of the future. Organic materials are advantageous because of their flexibility, processability, low toxicity, and cost. However, organic thermoelectric devices are presently lower efficiency than their inorganic counterparts, due to their lower electrical conductivities. This work seeks to progress towards higher-efficiency organic thermoelectric devices using several different approaches. First, poly(3,4-ethylenedioxythiophene) (PEDOT) thin-films were polymerized electrochemically onto a surface using galvanostatic, potentiostatic, and potentiodynamic techniques. It was determined that the surface morphologies of the potentiostatic and galvanostatic films are quite similar, but the potentiodynamic morphology is markedly different. An electrochemical dedoping process was developed for these films, and the degree of dedoping was monitored with UV-Vis and XPS. The oxidation levels in the films were found to vary between 11.7 and 33%. The electrical conductivity, Seebeck coefficient, and thermoelectric power factor of the PEDOT films were measured, and a maximum value of 13.6 $\mu W\ m^{-1}\ K^{-2}$ was obtained.

Second, two analogous polymers, HTAZ and FTAZ, were studied for future thermoelectric use. The polymers were chemically doped with $FeCl_3$, the degree of doping was monitored with UV-Vis, and the doping stabilities of both polymers were recorded. The electrical conductivity was also measured and related to the doping level. Despite the space-charge limited current (SCLC) mobility of FTAZ being nearly an order of magnitude higher than HTAZ, the conductivities were nearly identical.

Finally, as a way to increase mobility and conductivity in future organic thermoelectric devices, a novel metal-molecule-metal junction was designed and fabricated using an adapted transfer-printing technique. Patterned gold contacts were transferred onto poly(3-methylthiophene) (P3MT) brushes anchored to an ITO electrode. The junctions were electrically characterized via conducting AFM to determine charge transport behavior, and the SCLC mobility was extracted from the current-voltage curves. The polymer brush devices could be improved by annealing before transfer of the top gold contacts, and this led to a maximum increase of two orders of magnitude in device mobility.

To James Dodge, Todd Davis, and Edward Rajaseelan, thank you for helping me discover and grow my interest in science. This would not be written without any of you.

## ACKNOWLEDGEMENTS

I first would like to thank my advisor, Prof. Wei You. Wei, I greatly appreciate you allowing me to do research and grow as a scientist under your direction for the last five years. I know that you have always been available to answer my questions, to listen to my ideas, and to inject a spirited optimism into my work when necessary. I will always be grateful for your enthusiasm, even when things were not going as well as we hoped.

I would like to thank my collaborators. Travis LaJoie, Robert Bruce, Elizabeth Keenan, and Mark Moog, you have all been integral to the work I've accomplished, and I appreciate all of the ideas I've bounced off of you through the years. I would also like to thank the staff at CHANL for all of the help with instrumentation.

I am especially grateful to all of the members of the You Group that I've worked with over my time at UNC. You have all helped me at some point with ideas, problems, and solutions, and I have truly enjoyed engaging with all of you. I will miss our spirited discussions, our Friday lunches, and I consider myself especially fortunate to have been a part of our group.

I would not be where I am without my family. To my parents, my brother and sister, my grandparents, and everyone else, thank you for your love and support throughout the years.

Finally, I would like to thank Kaitlin. There is no way I would have made it through these five years without you. I realize how incredibly lucky I am to have your support, especially considering the distance between us. I'm so glad you took a chance on me.

## TABLE OF CONTENTS

## LIST OF FIGURES

**Figure**

## LIST OF TABLES

**Table**

## LIST OF EQUATIONS

**Equation**

## LIST OF ABBREVIATIONS AND SYMBOLS

| | |
|---|---|
| A | Ampere |
| Å | Angstrom |
| AFM | Atomic force microscopy |
| Sb | Antimony |
| β | Beta parameter |
| Bi | Bismuth |
| $k_B$ | Boltzmann constant |
| Bmim $PF_6$ | 1-Butyl-3-methylimidazolium hexafluorophosphate |
| °C | Degrees Celsius |
| cm | Centimeter |
| n | Charge carrier density |
| μ | Charge mobility |
| Cr | Chromium |
| cAFM | Conducting atomic force microscopy |
| I | Current |
| J | Current density |
| ε | Dielectric constant |
| DMSO | Dimethyl sulfoxide |
| σ | Electrical conductivity |
| EPoly | Electropolymerization |
| q | Elementary charge |
| eV | Electron volt |
| $E_g$ | Energy band gap |

| | |
|---|---|
| G | Energy release rate |
| $G_c$ | Energy release rate (critical) |
| EDOT | Ethylene dioxythiophene |
| EGaIn | Eutectic gallium indium alloy |
| $E_F$ | Fermi level |
| Au | Gold |
| g | Gram |
| HOMO | Highest-occupied molecular orbital |
| hr | Hour |
| HF | Hydrofluoric Acid |
| ITO | Indium tin oxide |
| K | Kelvin |
| KTP | Kinetically-controlled transfer printing |
| LAME | Large area molecular electronics |
| LUMO | Lowest-unoccupied molecular orbital |
| Pb | Lead |
| l | Length |
| MMM | Metal molecule metal |
| m | Meter |
| μA | Microampere |
| μm | Micrometer |
| μV | Microvolt |
| mbar | Millibar |
| mL | Milliliter |
| mm | Millimeter |
| mmol | Millimole |

| | |
|---|---|
| Mtoe | Million of tonnes of oil equivalent |
| mW | Milliwatt |
| M | Molarity |
| ME | Molecular electronics |
| nm | Nanometer |
| nTP | Nano-transfer printing |
| NASA | National Aeronautics and Space Administration |
| OFET | Organic field-effect transistor |
| OLED | Organic light-emitting diode |
| OPV | Organic photovoltaic |
| Pd | Palladium |
| PFPE | Perfluoropolyether |
| pm | Picometer |
| Pt | Platinum |
| P3HT | Poly(3-hexylthiophene) |
| P3MT | Poly(3-methylthiophene) |
| PEDOT | Poly(3,4-ethylenedioxythiophene) |
| PProDOT | Poly(3,4-propylenedioxythiophene) |
| PDMS | Poly(dimethylsiloxane) |
| PPV | Poly(phenylene vinylene) |
| PSS | Polystyrene sulfonate |
| p-n | Positive-type / negative-type semiconducting junction |
| Π | Peltier coefficient |
| R | Resistance |
| RPM | Revolutions per minute |
| RMS | Root-mean square |

| | |
|---|---|
| PF | Thermoelectric power factor |
| SCLC | Space-charge limited current |
| SEM | Scanning electron microscopy |
| STM | Scanning tunneling microscope |
| s | Second |
| S | Seebeck coefficient |
| S | Siemens |
| SAM | Self-assembled monolayer |
| $R_s$ | Sheet Resistance |
| Si | Silicon |
| $SiO_2$ | Silicon oxide |
| Ag | Silver |
| $AgNO_3$ | Silver Nitrate |
| S | Sulfur |
| SI-KCTP | Surface-initiated Kumada catalyst-transfer polycondensation |
| Te | Tellurium |
| T | Temperature |
| $TBAPF_6$ | Tetrabutylammonium hexafluorophospahte |
| κ | Thermal conductivity |
| TE | Thermoelectric |
| TEG | Thermoelectric generator |
| t | Thickness |
| TWh | Terawatt-hour |
| Tos | Tosylate |
| UV | Ultraviolet |
| UV-Vis | Ultraviolet-visible Spectroscopy |

| | |
|---|---|
| $v$ | Peel velocity |
| $v_c$ | Peel velocity (critical) |
| $v_o$ | Peel velocity (reference) |
| V | Voltage |
| ZT | Thermoelectric figure of merit |
| XPS | X-ray Photoelectron Spectroscopy |

# *Chapter 1*
# INTRODUCTION TO THERMOELECTRIC ENERGY AND ORGANIC ELECTRONIC MATERIALS

## 1.1 Background

On or around October 31, 2011, the global population exceeded 7 billion people.[1] This number is expected to continue to increase and in 2050 will most likely be over 9 billion. An increasing population, coupled with a rapid rise in access to industry and technology in developing countries, has led to a massive expansion of energy use around the world. In fact, energy consumption has increased 92% from 1973 to 2012, and current energy usage is approximately 9,000 Mtoe (1 Mtoe = 11.6 TWh).[2] Regrettably, only 3.5% of this consumption is currently derived from renewable energy sources (solar, wind, heat, and geothermal). Clearly the proportion of energy derived from these technologies will need to increase if we are to meet the needs of a growing populace in the face of severe environmental concerns.

One major way to increase the use of renewables is to capture and utilize heat as an energy source. Of the energy produced in the United States today, close to 60% is wasted in the form of heat.[3] Examples of heat waste include automobile exhaust systems, manufacturing, and primary energy production. Thermoelectric (TE) materials are able to convert directly between heat and electricity, and thus could be an extremely useful way to exploit wasted heat. These materials contain no moving parts, and because


**Figure 1.1.** Examples of thermoelectric applications

Clockwise from top left: A wine fridge using a thermoelectric cooling element, a dehumidifier using a thermoelectric condenser, an automobile seat heating/cooling system, the NASA Curiosity rover which is powered by a thermoelectric generator.

of this they are extremely light, quiet, and reliable. They have found their way into several applications, some of which are shown in **Figure 1.1**.[4–7] However, despite intense research into TE materials over the last two decades, commercial applications have been limited so far to niche markets in which solid-state devices are required. This is because thermoelectrics have modest efficiency numbers compared with other energy and cooling technologies, as well as a high cost of production. Current TE technologies employ inorganic semiconducting alloys as the working material. These alloys are typically composed of some combination of bismuth, lead, antimony, selenium, and tellurium, which are both expensive and toxic for the environment. In addition to these drawbacks, the best performing TE device architectures require complicated fabrication processes, which generally involve depositing several atomically-thin layers of material. These manufacturing intricacies further increase the final device cost.

To mitigate some of the costs and complexities of inorganic materials, researchers have turned to organic electronics since the turn of the century, and have made exceptional progress in this field. These materials are carbon-based polymers or small molecules that can conduct charge, and they are often ideally suited to either complement or replace more traditional inorganic-based systems. They are lightweight, flexible, synthetically tunable, cheap, and relatively non-toxic to the environment. Organic electronics are currently being used for solar energy, electronic displays, logic devices, and electrochromic devices.[8] Although they often have lower performance than their inorganic analogues, they continue to push into markets traditionally held by silicon-based electronics, thanks to the ease of manufacturing and low materials cost. Examples of organic electronic devices can be seen in **Figure 1.2**.[9,10]

**Figure 1.2.** Examples of organic electronic devices

Top: Heliatek OPV manufactured device. Bottom: Samsung OLED TV manufactured device.

More recently, organic electronic materials have emerged as candidates for TE devices. The low cost of raw materials and ease of processability should lead to cheapdevices that can hopefully be used in several new applications. Before these goals can be realized, however, the efficiency of organic-based TEs must increase. Thus, the focus of this work is to explore several different materials for use in organic thermoelectric devices. By developing relationships between composition, morphology, and performance, new materials can be made to meet the world's growing energy demand.

## 1.2 Principles of Thermoelectric Effects

### *1.2.1 Discovery of Thermoelectricity*

Two main effects will be of interest to this work, the Seebeck effect and the Peltier effect. These effects are named after their discoverers, Thomas Johann Seebeck, and Jean Charles Athanase Peltier, respectively. In 1820, Seebeck observed that if two dissimilar metals were joined in a closed loop, and a temperature gradient was applied so that the two metals were connected thermally in parallel, a compass needle was deflected. He posited that the temperature gradient through the metal loop created a magnetic field and thus termed this phenomenon *thermomagnetism*. However, Hans Christian Oersted later correctly proposed that the temperature difference creates an electric current in the loop, which induces a magnetic field. He was the first to use the term *thermoelectricity*.[11] The Seebeck effect is described by

$$\Delta V = S \times \Delta T \tag{1}$$

Where the *Seebeck coefficient (thermopower),* S, is the measure of how well a material can generate electric power for a given temperature difference.

Fourteen years later, in 1834, Peltier discovered the complementary effect. He noticed that when current is passed through a closed loop of two different conductors, a thermal gradient is generated at the junction of the two materials. Whether the thermal effect is heating or cooling depends on the direction of current flow through the loop.[12] The Peltier effect is given in (2), and the *Peltier coefficient,* Π, relates how much heat is carried by the charges in a material at a certain current.

$$Q = \Pi \times I \tag{2}$$

The Seebeck and Peltier coefficients can then be related through (3), the Kelvin relation.

$$\Pi = ST \tag{3}$$

*1.2.2 Thermoelectric Devices and the Figure of Merit*

Today, almost all TE devices employ semiconductors, specifically a pair of n-type and p-type semiconductors connected electrically in series and thermally in parallel. If one side of the device is heated, charges will migrate from the hot side to the cool side, and a voltage that can power a load resistor will be generated via the Seebeck effect. Devices that use the Seebeck effect to generate power are known as thermoelectric generators (TEGs). Thermocouples are also based on the Seebeck effect, but rather than powering a resistor, the voltage generated (thermovoltage) is measured by a voltmeter and converted into a temperature. An example of a TEG is shown in **Figure 1.3a**.

Alternatively, if a power source is connected to the p-n connection instead of a load resistor, current will flow through the circuit and carry heat from one side to the

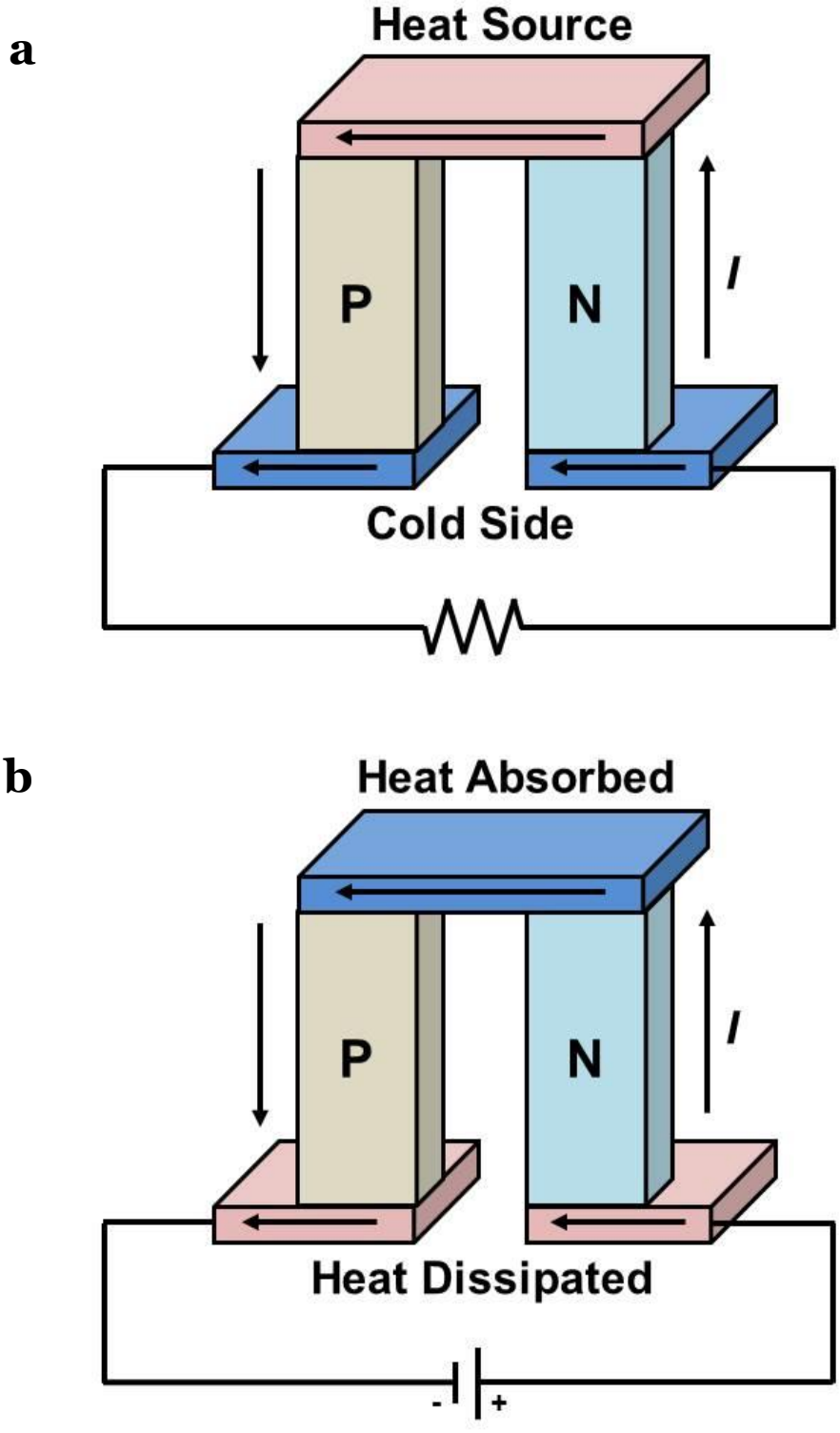


**Figure 1.3.** Semiconductor thermoelectric devices

*(a)* TEG. *(b)* Peltier Cooler.

other based on the Peltier effect. This creates a temperature gradient along the length of the semiconducting legs, having a cold side where the heat is absorbed, and a heat sink where it is dissipated. This device is known as a Peltier cooler (**Figure 1.3b**) and is useful in refrigeration applications.[13]

Due to the relatively low thermovoltages generated by a semiconducting p-n pair, often on the order of several microvolts, many pairs are connected in series to increase the operating voltage of TEGs. However, the thermovoltage quantity is not the only concern in evaluating the performance of a TE system. The unitless figure of merit ZT is used to compare between TE materials, and also to relate the efficiencies of the best TE materials with those of other energy generation sources. ZT is

$$ZT = \frac{S^2\sigma}{\kappa}T \tag{4}$$

Where σ is the electrical conductivity and κ is the thermal conductivity. The numerator of the ZT equation ($S^2\sigma$) is known as the power factor (PF) and is also a useful performance metric. Most commercial TE applications have a ZT value near 1. However, if efficiencies close to those of other power generation sources are desired, an increase in ZT to above 4 will be necessary.[14]

It is immediately apparent that in order to achieve a high ZT the electrical conductivity (σ) and thermopower (S) should be maximized, while the thermal conductivity should be minimized. This has proven extremely difficult because of the interrelation between σ, S, and κ in the ZT equation. Though insulating materials have extremely high thermopowers, their inability to carry charge renders them useless. Conversely, metallic systems have high conductivities due to their large number of free

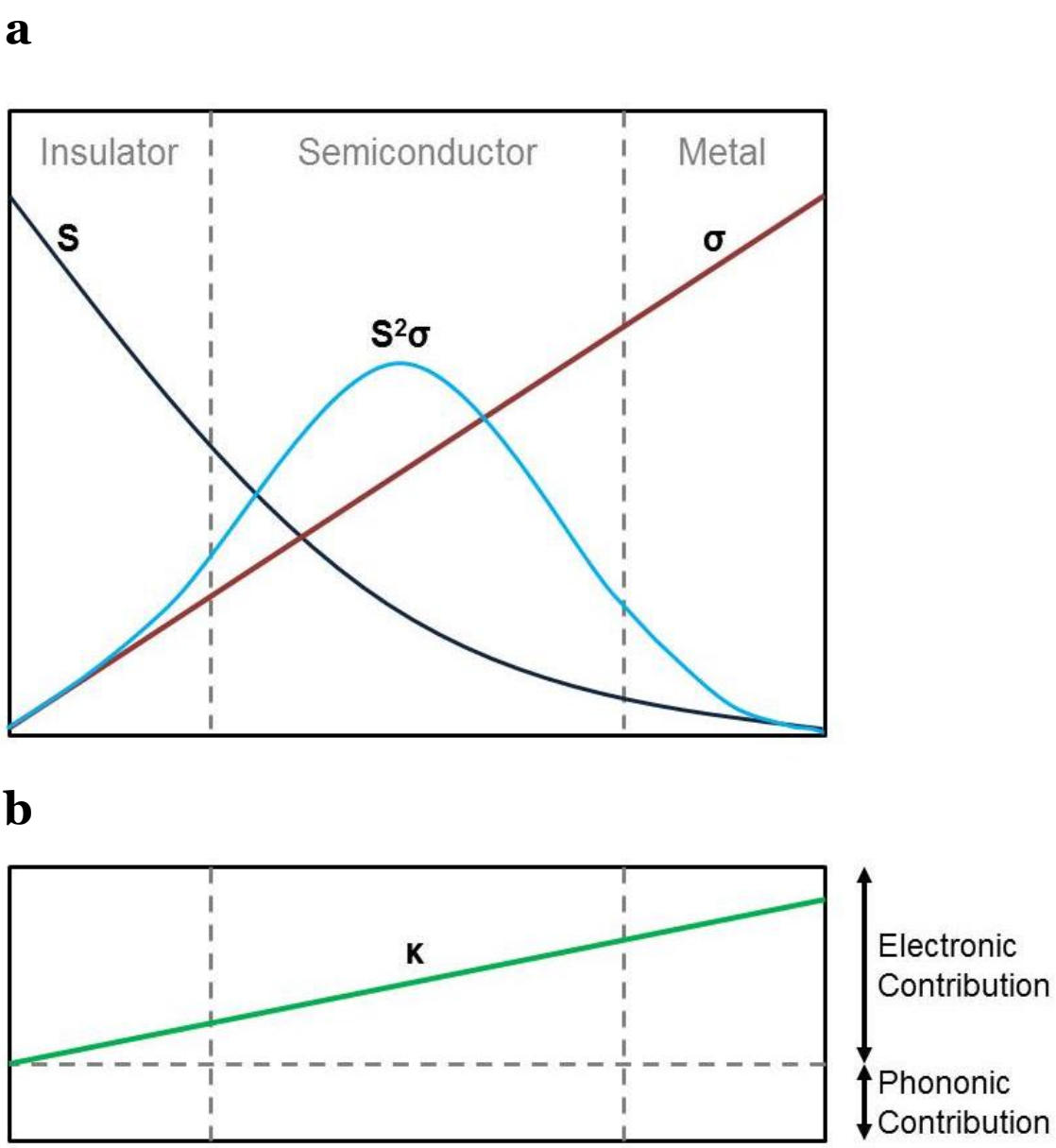


**Figure 1.4.** Thermoelectric figure of merit parameter relationships

*(a)* Trade-off between electrical conductivity and Seebeck coefficient as a function of carrier density. *(b)* Dependency of thermal conductivity on electronic and phononic components as a function of carrier density.

carriers, but these carriers lower the Seebeck coefficient which lowers performance. By controlling charge carrier density, the power factor can be maximized as seen in **Figure 1.4a**. The relationship between σ and κ is also disadvantageous. Thermal transport can be divided into a lattice contribution (phonons) and an electronic contribution Figure **1.4b**). The main heat carriers in metals are electrons, and therefore σ and κ are directly proportional to each other as described by the Wiedemann-Frantz Law. In semiconductors and insulators phonons are the main heat transporters.

Taken together, the interplay among ZT parameters means that the best performing TE materials are semiconductors with a bandgap around 6 – 10 $k_BT$.[15–17] The current state of the art at the laboratory scale involves fabricating superlattices of inorganic semiconductor alloys, including $Bi_2Te_3/Sb_2Te_3$, PbSeTe/PbTe, and AgPb/SbTe.[18–21] Both the alloying of different elements and the creation of superlattices leads to a decrease in the thermal conductivity of the devices, well below what would be found in a bulk material. The ZT values of these types of devices can be well over 2.[18,19] However, this type of fabrication does not alleviate concerns of materials cost or environmental toxicity, and in fact it becomes extraordinarily difficult to mass produce these types of nanostructures. Moving to more abundant elemental sources and simplifying fabrication may be a different way forward to mass production of TE devices.

## 1.3 Principles of Organic Electronics

### *1.3.1 Discovery of Organic Electronics*

Though polyaniline was discovered as the first organic conducting material in the middle 19$^{th}$ century,[22] it was not until nearly 100 years later in 1958 that the first organic

electronic device was fabricated as a small molecule OPV.[23] This was followed by a period of rapid discovery in the 1960s and 1970s when several new conjugated polymers were synthesized, including polyphenylene,[24] polypyrrole,[25] poly(p-phenylene vinylene),[26] and polyacetylene.[27] It was also revealed during this time that organic materials intrinsically have very low conductivity, but this can be increased by doping.[27] In 1987 the first OLED was made by Eastman-Kodak using a small molecule (8-hydroxyquinilone aluminum) as the active emitting material.[28] That same year Mitsubishi Electric Corporation fabricated the first OFET via a polythiophene channel.[29]

The field sustained growth into the 1990s as researchers continued to learn the importance of structure and morphology on device performance. In 2000 Alan Heeger, Alan McDiarmid, and Hideki Shirakawa were awarded a Nobel Prize "for the discovery and development of conductive polymers."[30] In the 15 years since 2000, organics have started to reach commercial applications in the cell phone, television, and solar energy markets, and their influence is only continuing to grow.

### *1.3.2 Conductivity and Charge Transport in Organic Polymers*

In saturated polymers, $sp^3$ orbitals form the molecular backbone, leaving no delocalized electrons to carry charge. In conjugated polymers however, unsaturated $sp^2$ orbitals create delocalized π-orbitals. These π-orbitals are capable of charge transport along polymer chains while maintaining structural stability, though breaks in conjugation often occur through ring twisting, chain termination, and structural defects. It is most accurate to imagine an electron in a conjugated polymer as being delocalized across several units, but not throughout the entire system. These types of polymers exist as semiconductors rather than conductors because of chain distortions from alternating

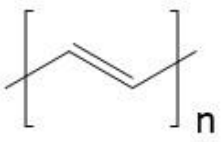

trans-polyacetylene

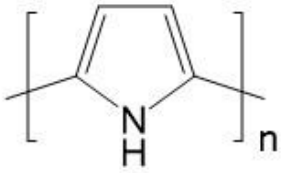

polypyrrole

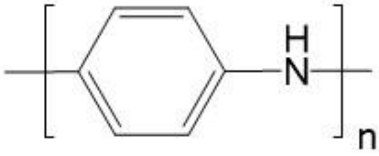

polyaniline

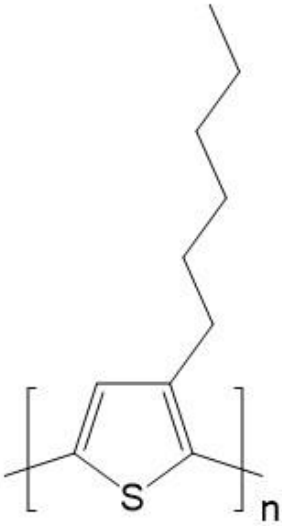

poly(3-hexylthiophene)
(P3HT)

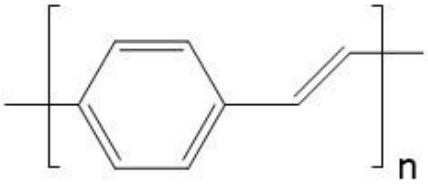

poly(p-phenylene vinylene)
(PPV)

**Figure 1.5.** Examples of conjugated polymers.

single and double bonds, and their band gaps are usually between 1 and 4 eV. Several structures are given in **Figure 1.5**.

The electrical conductivity of a material can be described as (5)

$$\sigma = nq\mu \tag{5}$$

where $n$ is the charge carrier density, $q$ is the elementary charge, and $\mu$ is charge mobility which is a measure of how quickly charges transport through a material. Because conjugated polymers intrinsically have low charge carrier densities, they must be doped in order to conduct, and this doping can occur either chemically or electrochemically. In chemical doping, a p-type polymer is exposed to an oxidizing agent that oxidizes the polymer into the doped state (positively charged), and the dopant becomes a counter anion to neutralize charge. Examples of chemical dopants are iodine vapor,[31] and ferric salts.[32,33] In electrochemical doping, a p-type polymer is placed in contact with an electrode in an electrolytic solution. When a potential above the ionization energy of the polymer is applied to the electrode, oxidation occurs, and anions in the electrolyte will then diffuse into the film to balance the positive charges. It is also possible to oxidatively polymerize certain monomers, directly forming a fully doped polymer. The carrier densities in these types of polymers can be controlled via reduction, either chemically or electrochemically.

When polymers are doped, the free charge carriers can manifest in one of three different forms; solitons, polarons, and bipolarons. While solitons exist exclusively in polyacetylene, polarons and bipolarons can be found in several different conjugated polymer systems. In general, a polaron is a radical cation with increased quinoid

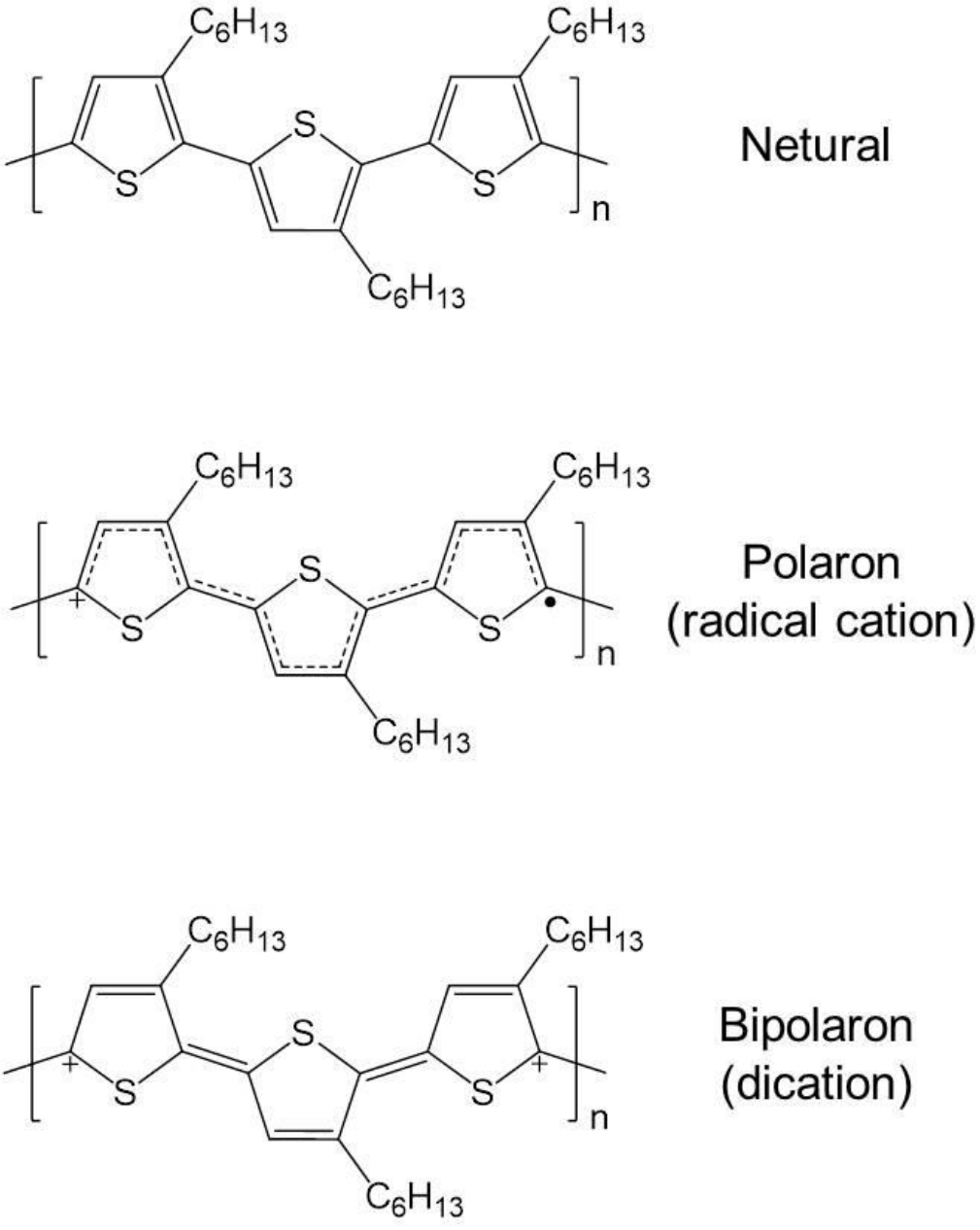


**Figure 1.6.** Different charge transport modes in P3HT.

character when compared with a neutral chain, while a bipolaron is a dication with a clear quinoid structure (**Figure 1.6**). How polarons and bipolarons transport through conducting polymers depends on a variety of factors, including crystallinity, doping concentration, molecular design, and chain conformations. In general, most conjugated polymers transport electrons by nearest-neighbor hopping, where the electrons are localized to certain sites and must overcome an energy barrier to travel between sites. Doping lowers these energy barriers, and thus increases the conductivity.

## 1.4 Thermoelectricity in Organic Materials

### *1.4.1 Motivation and Early Efforts*

As mentioned in 1.2.2, a material must possess a high electrical conductivity, high Seebeck coefficient, and low thermal conductivity in order to maximize thermoelectric performance. When organic conducting materials were developed, it was discovered that their thermal conductivities were a fraction of some of the best inorganic TE materials, such as $Bi_2Te_3$.[34,35] This led to interest in the thermoelectric properties of these polymers. Polyacetylene was found to have a power factor of 0.1 mW $m^{-1}$ $K^{-2}$, only one order of magnitude lower than $Bi_2Te_3$.[36] Unfortunately polyacetylene is environmentally unstable and not a good candidate for TE devices.

Research continued on several processable polymers, including polyaniline (ZT = $10^{-5}$),[37] and PPV (PF = 30 μW $m^{-1}$ $K^{-2}$).[38] In these early studies it was shown that although the thermal properties of polymers were ideal for TEs, excepting polyacetylene their electrical conductivities were lower than inorganic semiconductors by several orders of magnitude. These electrical conductivities led to much lower power factors and ZT values for conjugated polymers. Fortunately, Seebeck coefficients in polymeric

systems are often quite large, with S > 100 μV/K not uncommon, and researchers began work on increasing electrical conductivity by improving polymer morphology.

### *1.4.2 Recent Advances*

In the last several years, research in organic thermoelectrics has begun to include other various conjugated polymer structures. In polycarbazole derivatives, the electrical conductivity has been increased from 0.1 S/cm to 500 S/cm by enhancing organization between chains.[39,40] In poly(3-alkylthiophenes), it has been demonstrated that the power factor decreases as the alkyl side-chains are lengthened.[41] Daoben Zhu investigated several benchmark donor-acceptor type polymers and discovered that an increase in mobility led to better TE performance.[42] Efforts have also focused on blending different polymers together. Blends of poly(3-butylthiophene) and insulating polystyrene actually enhance electrical conductivity by driving the formation of crystallization of the thiophene chains.[43] Two different polythiophenes with different HOMO levels can enhance Seebeck coefficients through an intentional mismatch in the density of states at the Fermi level.[44] Finally, blends of polyselenophene with poly(3-methylthiophene) show incredibly high Seebeck coefficients of over 4000 μV/K, most likely from the effects of the selenium atom.[45]

The best performing conducting polymer for thermoelectric applications has been poly(ethylenedioxythiophene) (PEDOT). PEDOT can be oxidatively polymerized into its fully doped state, and it is often stabilized by the polymeric anion polystyrene sulfonate (PSS). This PEDOT:PSS is commercially available as a dispersion in water that can be easily processed into thin films by drop-casting, spin-casting, inkjet printing, or other similar processing techniques. The structures of both PEDOT and PEDOT:PSS are

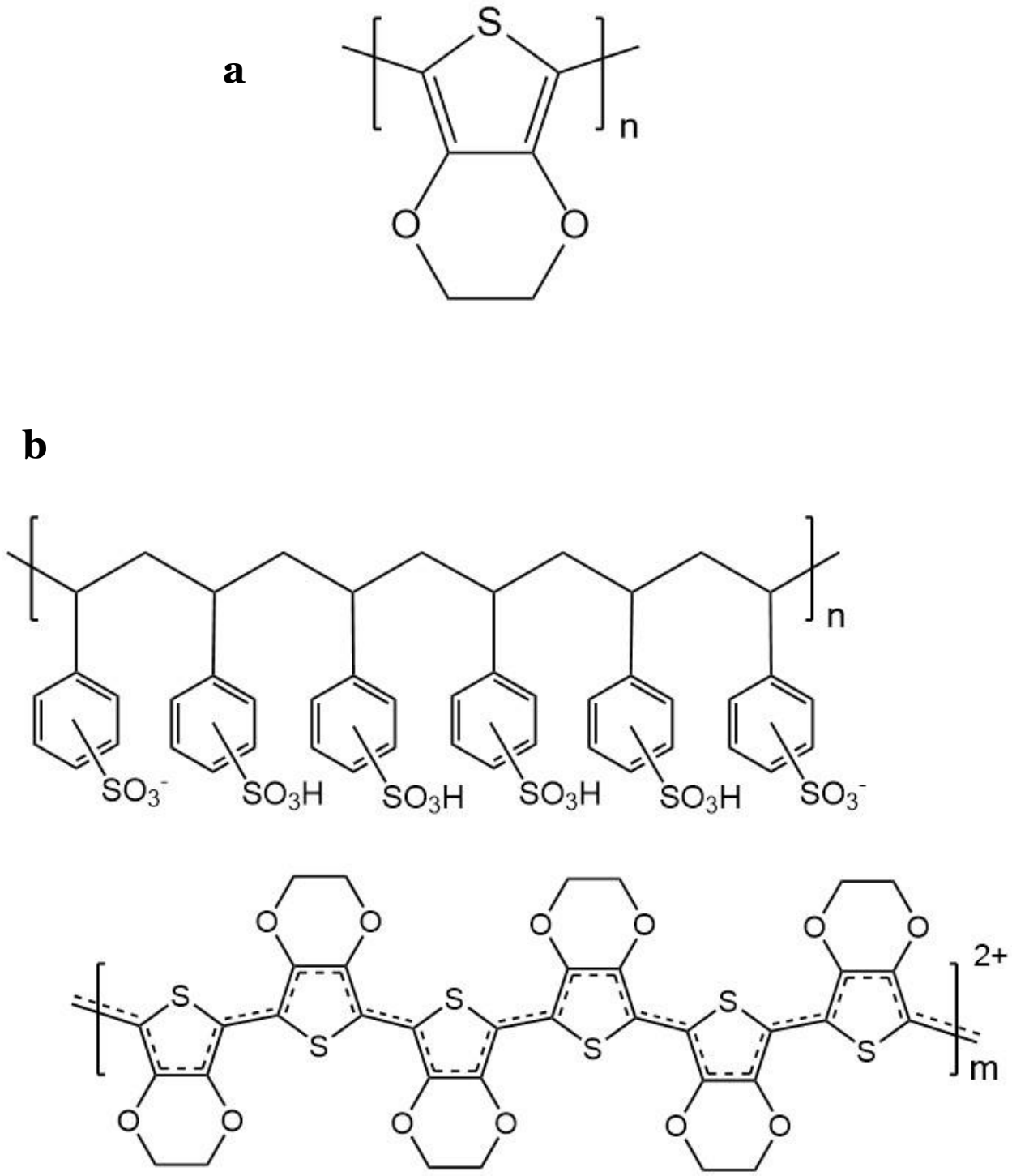


**Figure 1.7.** PEDOT polymers.

*(a)* PEDOT. *(b)* PEDOT:PSS.

represented in **Figure 1.7**. As-prepared PEDOT:PSS films are quite conductive (> 1 S/cm), but the conductivity can be greatly increased (> 500 S/cm) by adding secondary dopants such as DMSO or ionic liquids to the dispersion.[46,47] Because of its large conductivity value, PEDOT:PSS was used in several thermoelectric studies. Once a high conductivity film was formed, carrier concentration could be controlled by a post-coating dedoping process, using a reducing agent to neutralize the oxidized PEDOT chains.[48–51] As a result, the power factor was optimized to > 100 $\mu W\ m^{-1}\ K^{-2}$ in some cases.

A major advance occurred when Pipe et. al. determined that neutral PSS led to decreased thermoelectric performance.[52] Pristine PEDOT:PSS often contains mass ratios of 1:3 to enable high carrier concentrations in the final blend. However, these neutral PSS chains decrease the mobility of the PEDOT, and the high carrier concentrations lead to low Seebeck coefficients. Pipe discovered that by post-treating the films in either DMSO or ethylene glycol, the neutral PSS chains were removed, and both the electrical conductivity and Seebeck coefficient increased. This led to a ZT value of 0.42, the highest reported polymer value of ZT to date (**Figure 1.8a**). Since the work by Pipe et. al., other researchers have also observed high performance by removing neutral PSS via similar strategies.[53,54]

Though PEDOT:PSS is an excellent TE material, the necessary removal of neutral PSS chains adds extra complexity to device fabrication. This has encouraged work involving PEDOT polymers that are stabilized by small molecule counterions such as tosylate (Tos).[55,56] EDOT monomer is oxidatively polymerized and subsequently casted

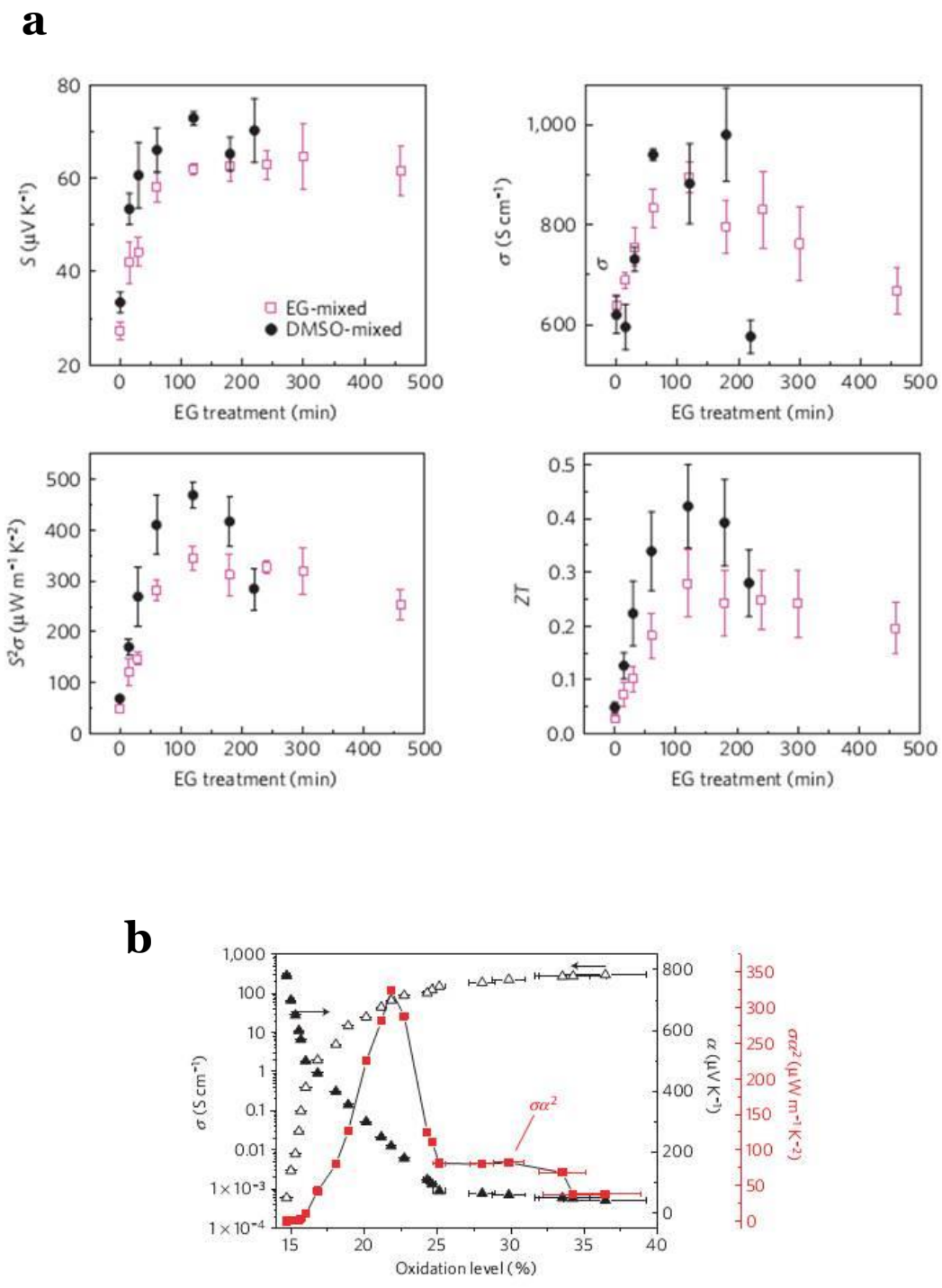


**Figure 1.8.** Thermoelectric performance of PEDOT-based materials.

*(a)* PEDOT:PSS treated with ethylene glycol to remove neutral PSS chains. *(b)* Oxidatively polymerized PEDOT:Tos dedoped with tetrakis(dimethylamnio)ethylene.

Reprinted from Reference 52 ©2013, and reference 55 ©2011

into films; the small molecule counterion exists solely as a charged species, and thus conductivity is not sacrificed by electrically inactive components as it is in PEDOT:PSS (recently Crispin et. al. revealed that PEDOT:Tos is a semi-metal, due to its bipolaronic charge carriers and high degree of order[57]). These types of polymers have also exhibited high TE performance, achieving ZT = 0.25 (**Figure 1.8b**). Further efforts are needed to explore the thermoelectric properties of other PEDOT-based materials not involving the PSS polyanion.

Clearly, polymer-thin-film organic materials are promising candidates for low-temperature, low-cost, environmentally-friendly TE applications, and several of these types of materials will be discussed in this dissertation. However, many polymer thin films suffer from relatively low mobility, and because mobility is directly proportional to conductivity as described in equation (5), lower mobility results in lower TE performance. Low mobility in polymer systems occurs when a high degree of inter-chain charge hopping is needed to transport electrons, as it is much faster for electrons to travel down single chains than to hop between chains.[58] A possible solution to mitigate these inter-chain hops is to design a device in which a single conjugated chain is sandwiched between two electrodes. This type of metal-molecule-metal (MMM) junction is an example of a molecular electronic device, and has been fabricated using many different types of small molecules.

## 1.5 Molecular Electronics

### *1.5.1 Introduction to Molecular Electronics*

Molecular electronics (ME) as a concept originated in 1974 when Aviram and Ratner proposed that a diode could be made by connecting a single molecule between

two electrodes,[59] and this idea has captured incredible amounts of attention in the 40 years since its proposal. The possibility of a single molecule device was incredibly avant-garde for the time period, and it was in over 20 years later that the first single molecule junction was made by James Tour in 1995.[60] These studies demonstrated the possibility of forming devices out of single molecules, and with the advent of the new millennium the field of ME greatly rose in popularity.[61–63] That electronics could be shrunk down to a series of single molecules, and that these molecules could individually impart desired functionality onto a device, remains a pioneering thought in the minds of chemists, physicists, materials scientists, and engineers.

A molecular electronic device can be thought of as having five different components (**Figure 1.9**): electrode 1, interface 1, molecule spacer, interface 2, and electrode 2. Each of these components will affect the electrical behavior of the junction, and each can be individually controlled. The combined perturbation of these five components leads to a practically infinite number of junction possibilities. One major area of research in ME is probing many different types of devices in order to gain information on how charge transport through single molecules happens. Also, if molecules hope to transition into commercial devices, it is essential that they are able to interface with electrodes quickly and reliably. As such, the other major area of ME research involves engineering devices to make reproducible contact to one or many molecules.

### *1.5.2 Types of Metal-Molecule-Metal Junctions*

Early MMM junctions formed temporary contact to either single or few molecules and measured their resistance. Tour's junction is a type of break junction, made by

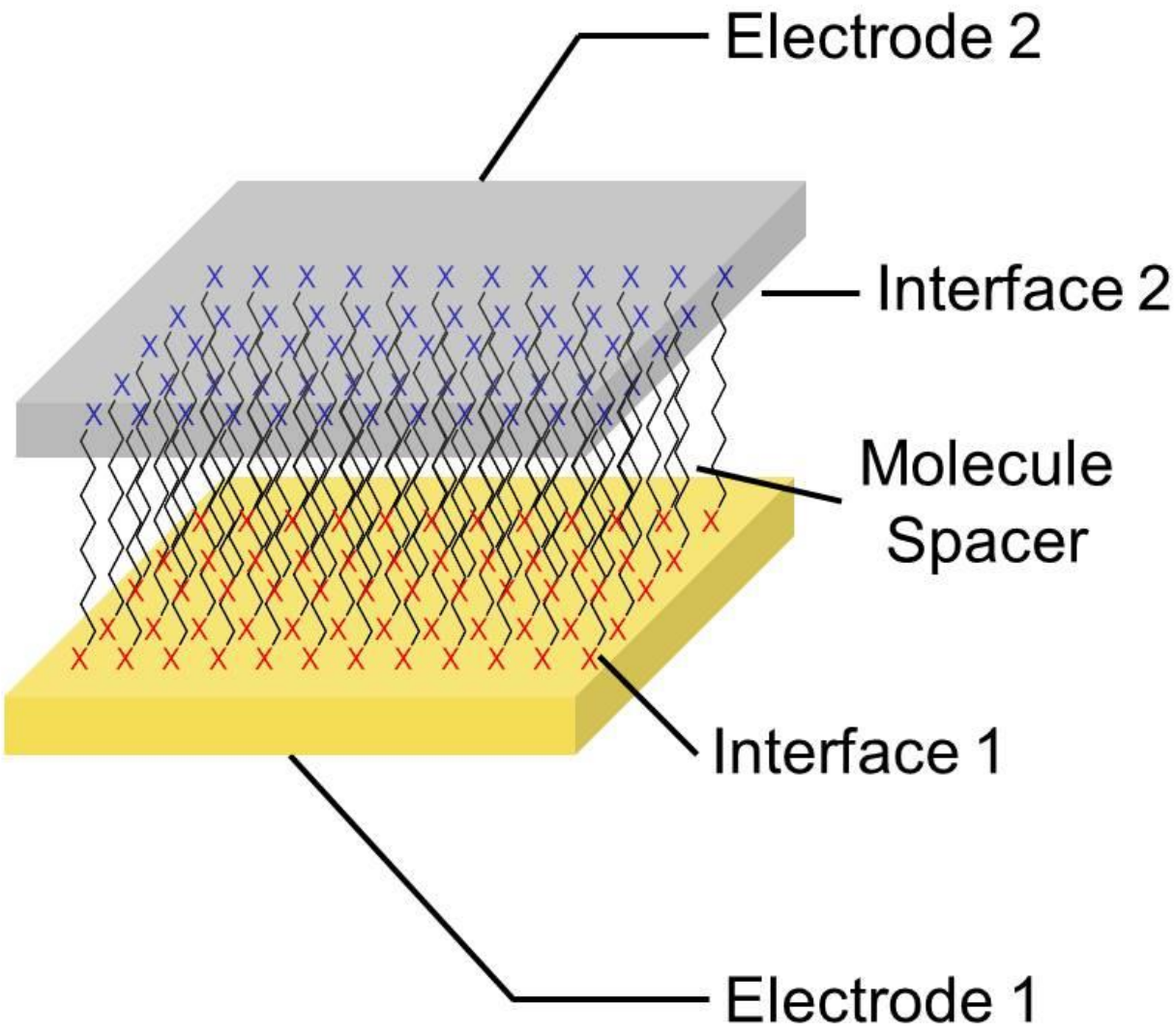


**Figure 1.9.** Diagram of a generic aliphatic MMM junction.

carefully fracturing a metal wire in the presence of a molecule; the molecule can then bridge the nanometer-sized gap and form the junction. Another common method to make single molecule junctions is to form a break junction using an STM tip.[64–67] In STM break junctions, a metal-coated STM tip is placed extremely close to a molecule-functionalized surface. A junction is formed between the tip and a molecule, and conductance is measured as the tip is retracted away from the surface. This is done until a "break" occurs (there is no longer a molecule between the tip and the surface), and the conductance value immediately before the break is recorded. However, because these single molecule junctions are extremely high variance measurements they must be repeated many times, usually > 1000, in order to achieve statistically reliable results. A way to mitigate this is by contacting many molecules simultaneously, which are known as large area molecule electronic (LAME) junctions.

The most common method to form analytical LAME junctions is conducting AFM (cAFM).[68–70] This is a variation of AFM in which the tip is coated with a conducting material (gold, platinum, etc.), and a bias is applied between the tip and a conducting surface. If a self-assembled monolayer (SAM) bridges the tip and the surface, a LAME junction is formed, and its area is defined by the area of the metal-coated tip. These types of junctions measure $10^3$ to $10^4$ molecules at once, thus eliminating much of the statistical noise associated with STM junctions. Another common method to form analytical LAME junctions is using an alloy of liquid eutectic gallium and indium (EGaIn), which can be dispersed directly on top of a monolayer.[71–73] Break junctions, STM junctions, cAFM junctions, and EGaIn junctions all have unique advantages and disadvantages, and all are presently used to look at new molecules and molecular

effects. Yet none of these techniques are permanent and able to be integrated into finished devices.

Forming permanent contact to SAMs is incredibly difficult because of the fragile nature of molecular layers.[74] Typical device fabrication techniques such as metal evaporation, sputtering, and etching, prove to be incompatible with SAMs, forming pinholes that short finished devices (**Figure 1.10a**). The most common way to avoid these pitfalls is to use a conducting buffer layer between the SAM and the metal top contact, such as PEDOT:PSS[75–77] or graphene[78–81] (**Figure 1.10b & c**). This strategy allows for a high percentage of working devices (>90%), but is not entirely desirable as it adds in additional interfaces, which complicates device behavior.[82] Recently, our group reported a way to form large-area MMM junctions via a transfer printing method using patterned polymeric stamps (**Figure 1.11**).[83,84] This eliminates the extra interfaces found in devices with buffer layers, making it an ideal solution for device fabrication and testing.

### *1.5.3 Thermoelectricity in Molecular Junctions*

Thermoelectricity in MMM junctions was first measured in 2007 by Majumdar et. al. when they reported the Seebeck coefficient of a series of bezenedithiol molecules using an STM.[85] It is often difficult to probe the electronic structure of a molecular junction, so this work was useful not only for possible energy conversion technologies, but also to identify the location of $E_F$ with respect to the HOMO and LUMO levels of the molecule by observing the sign and magnitude of the Seebeck coefficient. Thermopower measurements using an STM face the same types of difficulties as electrical measurements, so other measurements were developed using a cAFM instead to

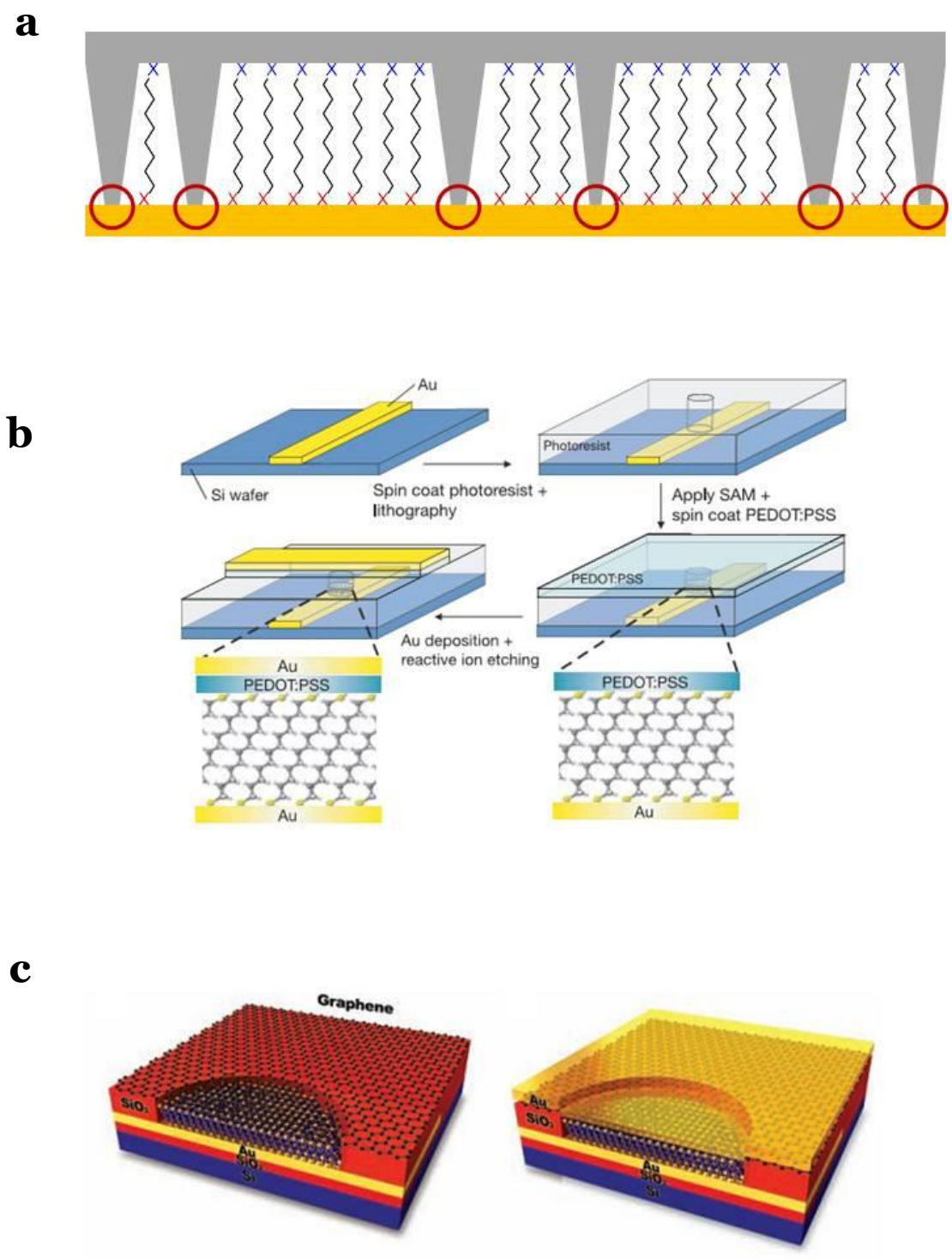


**Figure 1.10.** Permanent LAME Junctions.

*(a)* Directly deposited top metal contacts lead to SAM pinholes. *(b)* PEDOT as a buffer layer to protect SAM from top contact deposition. *(c)* Graphene as a buffer layer.

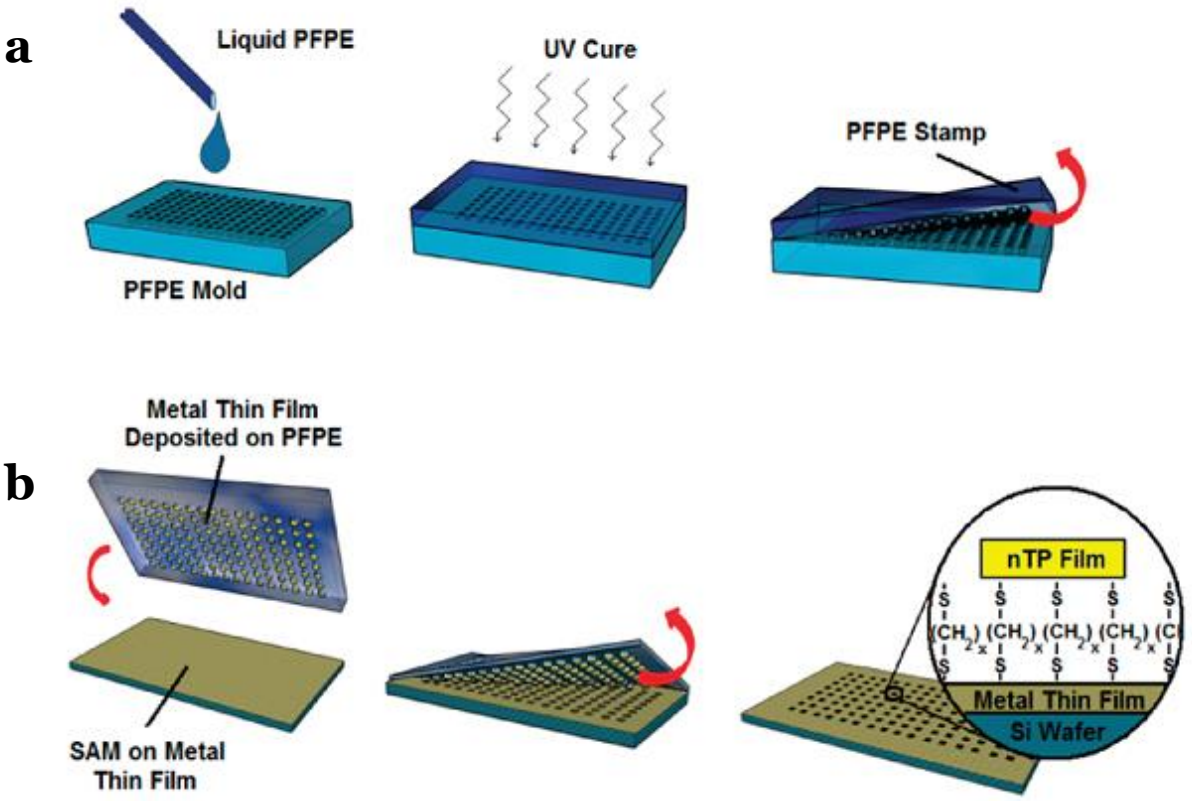


**Figure 1.11.** Nano-transfer printing (nTP) process.

*(a)* A patterned perfluoropolyether (PFPE) stamp is casted from a PFPE mold and UV cured. *(b)* A metal thin film is deposited onto the patterned stamp, and the film is transferred onto a SAM receiving substrate to form a MMM junction.

measure the Seebeck coefficient.[86,87] The STM and cAFM approaches allowed for the measurement of several different types of molecules, including conjugated[65,88,89] and fullerene-based[90] systems.

The above studies demonstrated that changing any of the electrodes, interfaces, or molecule spacers, affect the magnitude and sign of the Seebeck coefficient. It was also observed that in almost all cases, the thermopower increased as the length of the molecule spacer increased. However, the longest molecules measured to date in these types of MMM junction thermoelectric setups are only several repeat units, thus it will be necessary to measure the thermopower of molecules more than a few nanometers in length to observe if this value is further increased in longer molecules.

## 1.6 Research Overview

Though an incredible amount of effort has already been undertaken towards realizing successful polymer-based and molecular thermoelectric devices, there is still much to investigate in both of these areas. A better understanding of molecular structure/property relationships needs to be developed, more work needs to be done with high ZT-type materials, and the length of the molecules in MMM thermoelectric junctions needs to be increased.

This dissertation seeks to add to the already substantial body of work in organic and molecular thermoelectrics in the above three areas. First, PEDOT films are grown electrochemically from a conducting surface using galvanostatic, potentiostatic, and potentiodynamic methods, and their morphology is investigated by SEM, AFM, and UV-Vis. The conductivity of the PEDOT is controlled via electrochemical doping and measured in a 4-point probe setup, and the thermoelectric properties of the films is

measured at various doping levels. Second, doping methods are developed for two similar donor-acceptor type polymers, doping stability is recorded, and their conductivity is measured via 4-point probe. Finally, a transfer printing approach is adapted in order to form MMM junctions on top of monolayers. This approach is then used to fabricate novel molecular electronic devices on top of thiophene-based polymer brushes. These brushes are electrically characterized and assessed as a potential future thermoelectric material.

# *Chapter 2*
# ELECTROPOLYMERIZED PEDOT THIN FILMS AS A PROSPECTIVE ORGANIC THERMOELECTRIC MATERIAL

## 2.1 Introduction to General Electropolymerization Methods

### *2.1.1 Background*

The introduction to this dissertation demonstrated the importance of conductive polymers, including PEDOT, for future thermoelectric applications. Because PEDOT mixed with the polyanion PSS is stable and commercially available, it is by far the most widely used PEDOT system for TE devices. However, the PSS portion is electrically insulating and is actually the major component in most commercial blends in order to make the PEDOT:PSS processable.[46] The PSS thus needs to be selectively removed to achieve high performance, which requires additional processing and complicated device fabrication. Some researchers have started to work with other PEDOT-based materials such as PEDOT-Tos,[55,57,91] and these materials have been found to be among the best organic TE materials. These polymers are fabricated oxidatively from solution and subsequently cast into thin films onto a surface, and their small counterions lead to large electrical conductivities. An alternative method for PEDOT TE device fabrication is to polymerize PEDOT-based polymers from solution directly onto a surface. Electropolymerization (EPoly) methods are one way to accomplish this task.

### *2.1.2 Introduction to Electropolymerization*

Electropolymerization is a method that uses an electrical potential to drive polymer formation.[92] Although in principle both electrical oxidation and reduction can

produce polymer films, this work will focus exclusively on oxidative EPoly. Here, a solution of monomer is placed into a standard 3-electrode cell with some electrolyte. Either a positive potential above the oxidation potential ($E_{pol}$) of the monomer, or a current is applied to the working electrode. This causes the monomer to polymerize into a film at the electrode surface. Conjugated polymers that are polymerized in this manner do so in a linear fashion, maintaining their conjugation,[93] and they include polypyrrole,[94,95] polyaniline,[96,97] and several polythiophenes.[98–100] The working electrode can be any material that does not oxidize below $E_{pol}$, and materials such as stainless steel, glassy carbon, ITO, and Au have been used.

The specific mechanism of EPoly in the PEDOT case is given in **Figure 2.1**.[101,102] The first step is a one-electron oxidation of the 3,4-ethylenedioxythiophene (EDOT) monomer to produce a radial cation. Another one-electron oxidation of an additional monomer is followed by radical dimerization. Loss of two protons forms the conjugated dimer species, which can undergo a further one-electron oxidation to form a radical cation dimer derivative. The dimer radical cation can combine with a monomer to form the trimer, and through subsequent oxidation and combination steps the polymer chains grow. At a certain chain length, the EDOT oligomers become insoluble and will then deposit onto the surface. It is possible to have charged oligomers that will undergo further oxidation after they become insoluble, but most chain extension occurs in the solution phase. Also of note, the electrolyte in solution with the monomer will infiltrate the polymer film and serve as a counterion to balance the positive charges. Thus an EPoly PEDOT film is p-doped and its charge is balanced by the electrolyte anions.

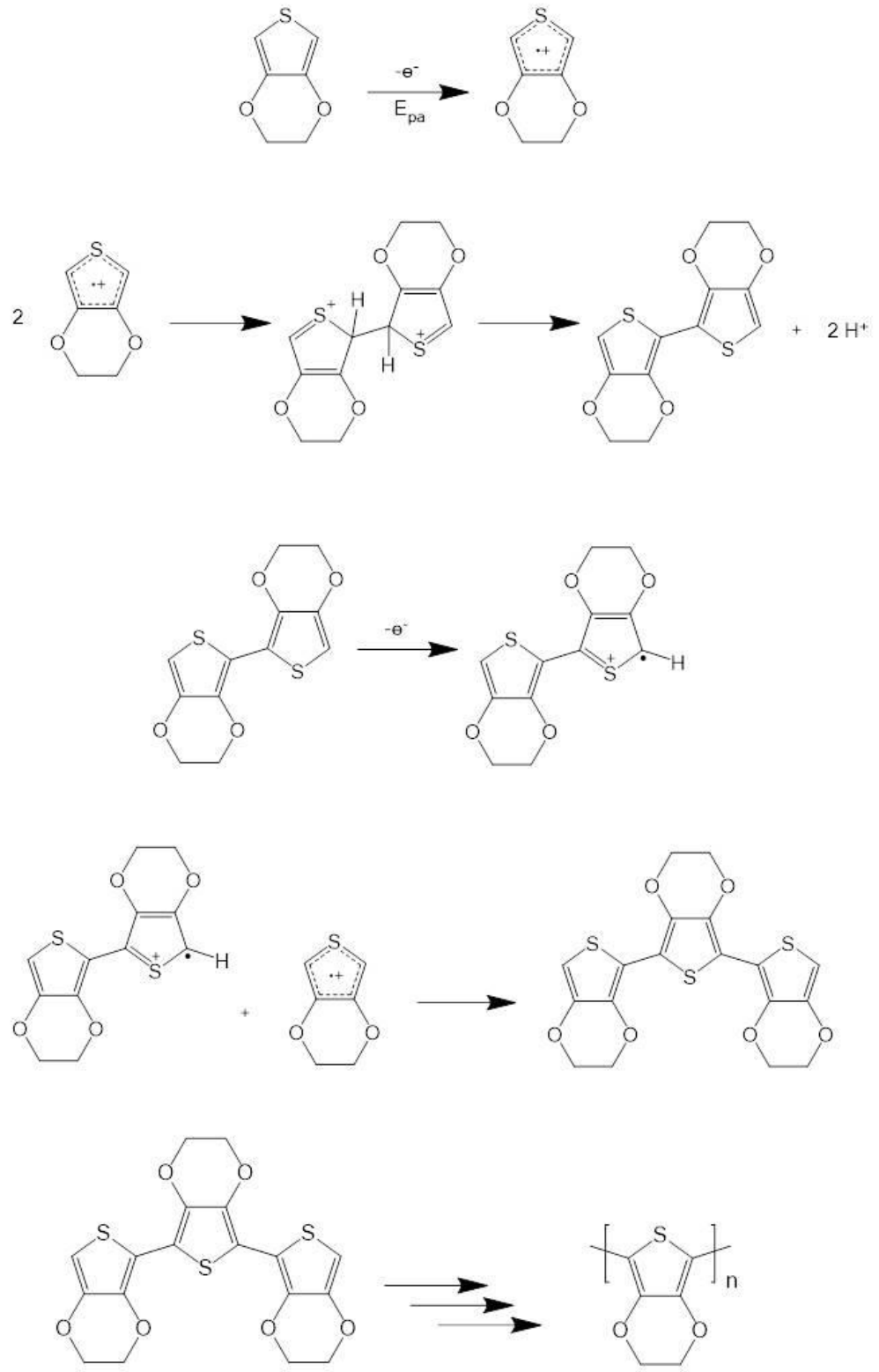


**Figure 2.1.** PEDOT electropolymerization mechanism

The morphology of these EPoly PEDOT films is affected by numerous factors, including the type and magnitude of the potential or current being applied to the working electrode, the concentration of the monomer, the concentration of the electrolyte, and the identity of the electrolyte.[103–105] Many of these factors will change the rate of polymerization, and in general, a slower polymerization rate will lead to smoother and less porous films.

### *2.1.3 Electropolymerization for Thermoelectric Applications*

EPoly films for thermoelectric devices are relatively rare in the literature, but there have been a few examples. Selenophene and 3-methylthiophene have been electropolymerized into a copolymer which enhances TE properties when compared with pure polyselenophene.[45] Electrodeposited polypyrrole has also been shown to have modest TE properties (maximum PF 4 $\mu W\ m^{-1}\ K^{-2}$).[94] PEDOT has been electropolymerized into nanowires by using a patterned working electrode,[106] and also into films whose morphologies can be controlled via counterion incorporation.[107] These examples indicate some interest in TE devices using EPoly-based materials, but more work needs to be done in order to draw conclusions on their viability.

In this Chapter PEDOT films are polymerized electrochemically via several methods, and they are evaluated electrically, morphologically, and thermoelectrically. Their thermoelectric properties are optimized through electrochemically dedoping, and comparisons are made between the different polymerization conditions.

## 2.2 Results and Discussion

### *2.2.1 Types of PEDOT Electropolymerization*

Three types of electropolymerizations were chosen for this study: galvanostatic, potentiostatic, and potentiodynamic. In galvanostatic polymerizations, a constant current is applied through monomer solution and voltage at the working electrode is measured as a function of time. In potentiostatic polymerzations, a constant voltage is applied to the working electrode and current is measured vs. time. Finally, in potentiodynamic polymerizations, the voltage is swept through a series of values and current is measured. Both linear sweeps and cyclic sweeps can be done, but cyclic voltammetry is more common and was chosen here. All polymerizations were carried out in an acetonitrile solvent, using a 1-Butyl-3-methylimidazolium hexafluorophosphate (Bmim $PF_6$) electrolyte, a $Ag/AgNO_3$ pseudo-reference electrode, and a Pt counter electrode.

### *2.2.2 Film Thickness and Polymerization Rate Effects*

As mentioned previously, several factors affect the final morphology, and thus the final properties, in EPoly-type films. These factors affect either the polymerization rate or the final film thickness. Though each of these variables could be tuned individually, to save time experiments were instead conducted to directly examine the effect of film thickness and polymerization rate on film morphology.

For film thickness, PEDOT films were electropolymerized potentiostatically on ITO for 30 s, 60 s, 90 s, and 120 s, and subsequently examined via SEM (**Figure 2.2**). In all polymer cases, wrinkling is seen in the film which occurs during the post-polymerization rinse. Despite this, clear differences emerge in the images. In the 30 s

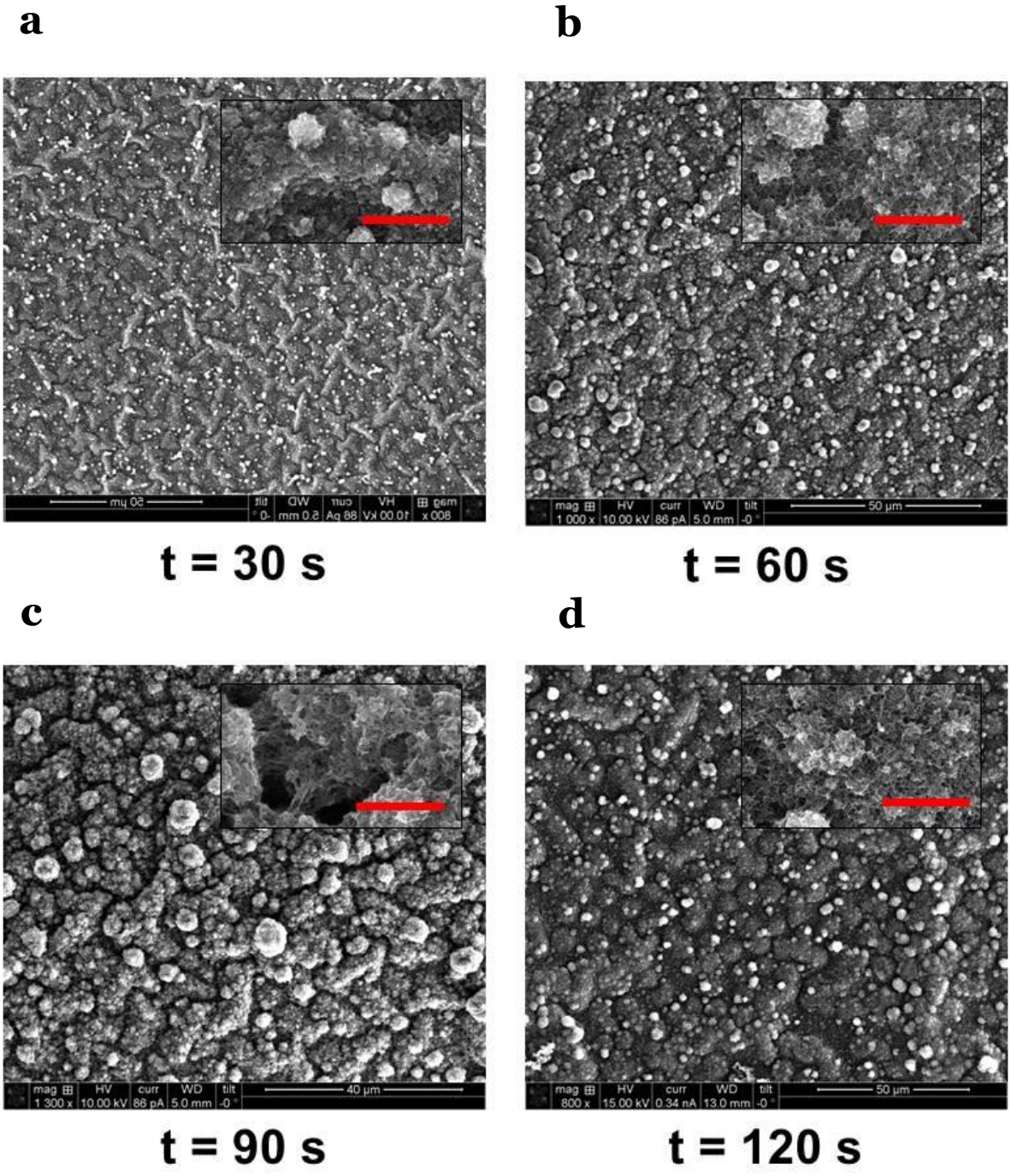


**Figure 2.2.** EPoly PEDOT morphological dependence on film thickness

*(a)* 30 s polymerization. *(b)* 60 s polymerization. *(c)* 90 s polymerization. *(d)* 120 s polymerization. Inset scale bar in all cases is 3 µm

case, morphology is relatively smooth and net-like, with some small globules forming on the surface. At 60 s, the size and number of the globules have increased, though they are still present on only a small portion of the surface. As the time is increased to 90 s and 120 s, the number of globules remains relatively constant, but the porosity in the film appears to increase, as evidenced by the insets in **Figure 2.2**.

The effect of polymerization rate on morphology was studied by polymerizing PEDOT potentiostatically at two different voltages, 900 mV for 420 s, and 1500 mV for 20 s. The polymerization time was varied so that the final film thicknesses were both near 120 nm. These films were characterized via SEM as well. In the low-bias case (**Figure 2.3a**) the film is exceptionally homogenous, showing an even size and spatial distribution of dense PEDOT regions at the surface of the film. These regions are connected together in a web-like network, which appears to become more dense deeper into the film. In the high-bias case (**Figure 2.3b**), the dense surface PEDOT regions are larger and unevenly distributed in both size and space. The web-like connections here are much more pronounced because of the larger surface regions, and the underlying film appears very similar to the low-bias case.

Ideally, the PEDOT EPoly process would create a film that is smooth, non-porous, and homogenous in composition. However, through these thickness and rate experiments, it is clear that this is not the case. Because the polymerization process is imperfect, a thicker film will lead to greater roughness and increased surface inhomogeneity over a thinner film, due to the increased reaction time in the thicker film. Likewise, polymerizing at a faster rate forces polymer to form less evenly on the surface when compared with a slower rate, which creates large clumps at the surface of

**a**

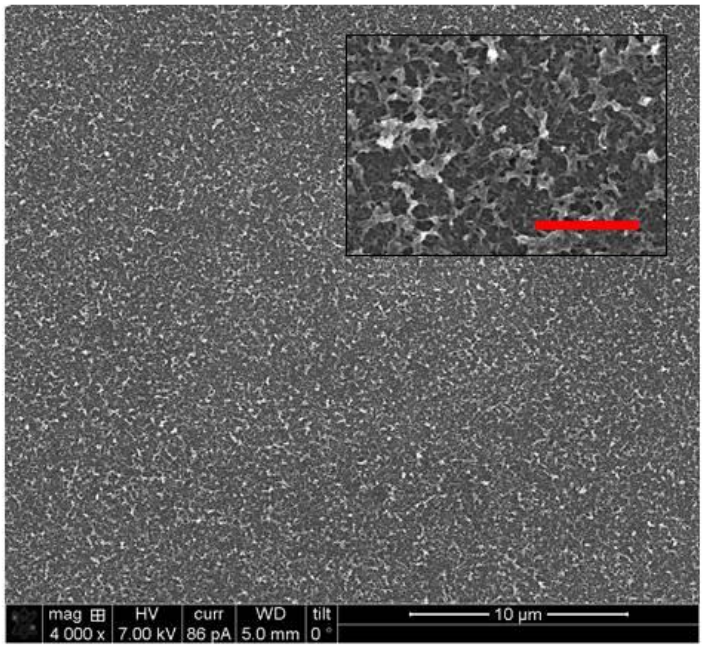


**b**

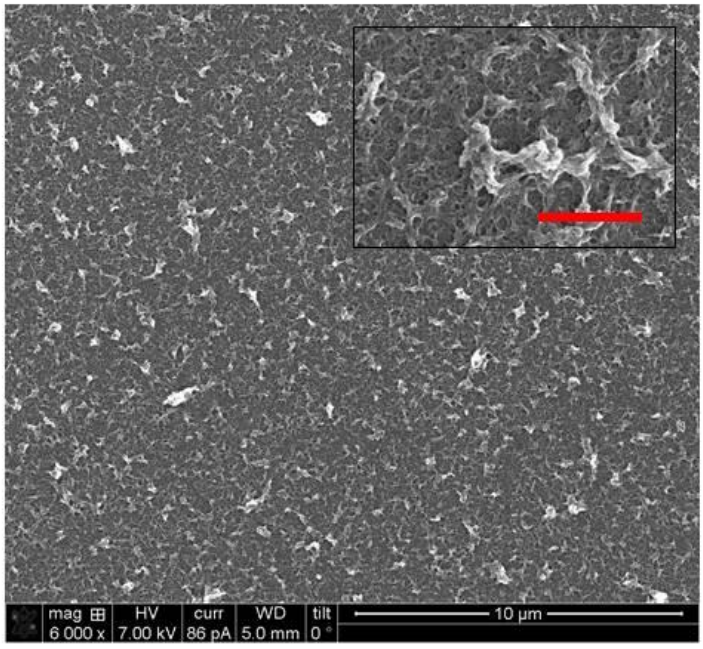


**Figure 2.3.** EPoly PEDOT morphological dependence on polymerization rate

*(a)* Potentiostatic polymerization of PEDOT at 900 mV for 420 s. *(b)* Potentiostatic polymerization of PEDOT at 1500 mV for 20 s.

the film as it grows. We have determined that to minimize roughness and porosity, the polymerization rate should be sufficiently slow (~ 1 nm/s), and films should be < 150 nm thick. Once this had been determined, films could be polymerized via several different methods.

*2.2.3 Potentiostatic EPoly PEDOT Films*

Potentiostatic films are polymerized onto 20 nm of gold at an EDOT and Bmim $PF_6$ concentration of 0.01 M, and they are polymerized for 120 s at 1025 mV. In these experiments the current increases as a function of time, and the rate of this increase is greatest immediately after starting the polymerization (**Figure 2.4a**). This current increase is directly attributed to the oxidation of EDOT monomers and oligomers at the surface of the working electrode, forming the PEDOT film. Because there is possibly significant sample-to-sample variation in electropolymerized films, error bands representing 95% confidence are added to these curves.

The polymer films are characterized via UV-Vis absorbance spectroscopy (**Figure 2.4b**). There are three main absorption bands attributed to PEDOT thin films. The bipolaron band exists in the near-infrared, beyond the wavelengths of this spectrum, the polaron band is at around 900 nm, and the neutral band is around 600 nm. There is a broad absorbance band in the potentiostatic PEDOT spectrum, indicating bipolarons, polarons, and neutral regions. The specific ratios of these carriers are unknown, but because there are no clear peaks at either 900 nm or 600 nm it is presumed that the PEDOT is heavily oxidized.

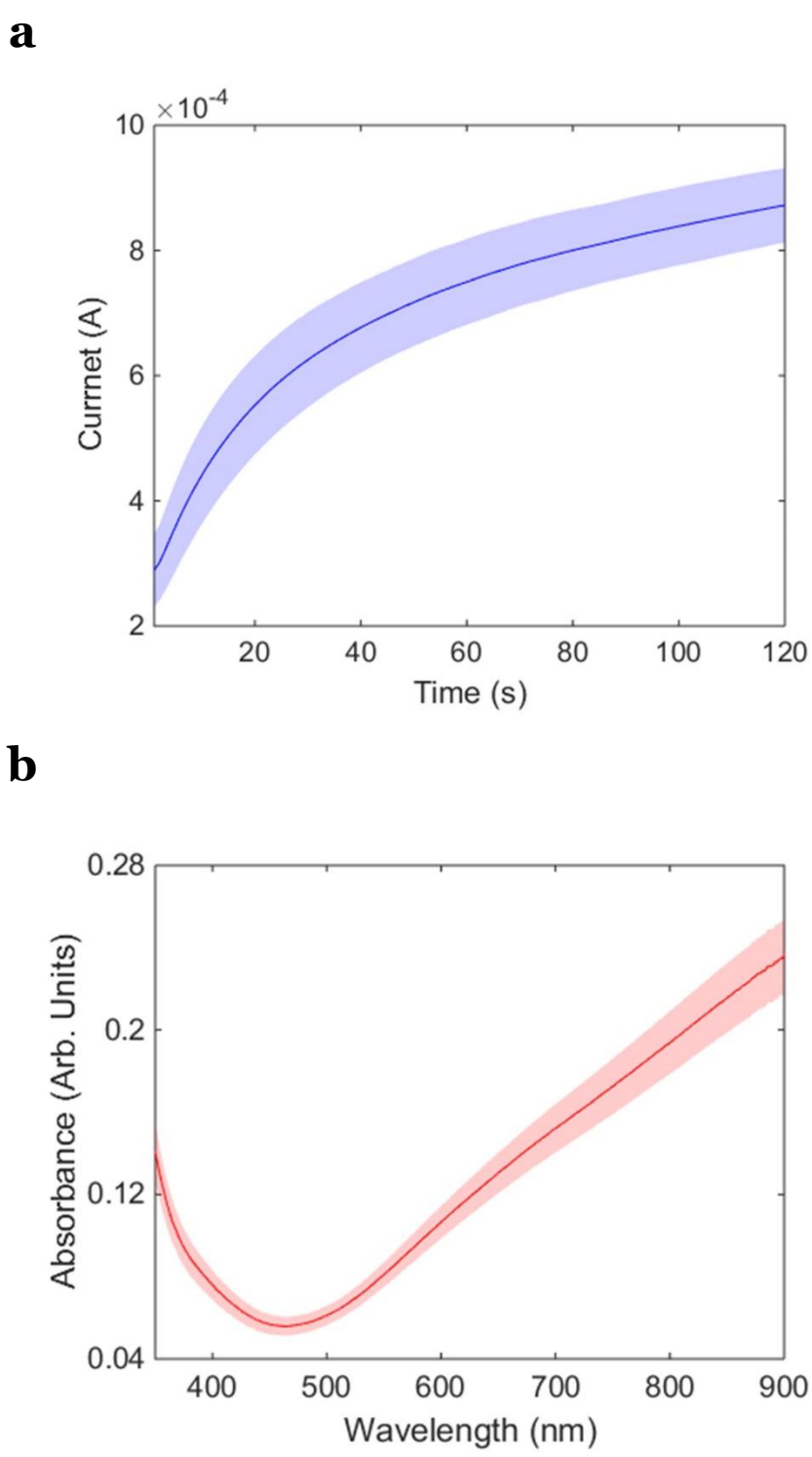


**Figure 2.4.** Potentiostatic electropolymerization of PEDOT

*(a)* Average current vs. polymerization time. *(b)* Average UV-Vis spectra for the polymerized films. Shaded bands are 95% confidence intervals.

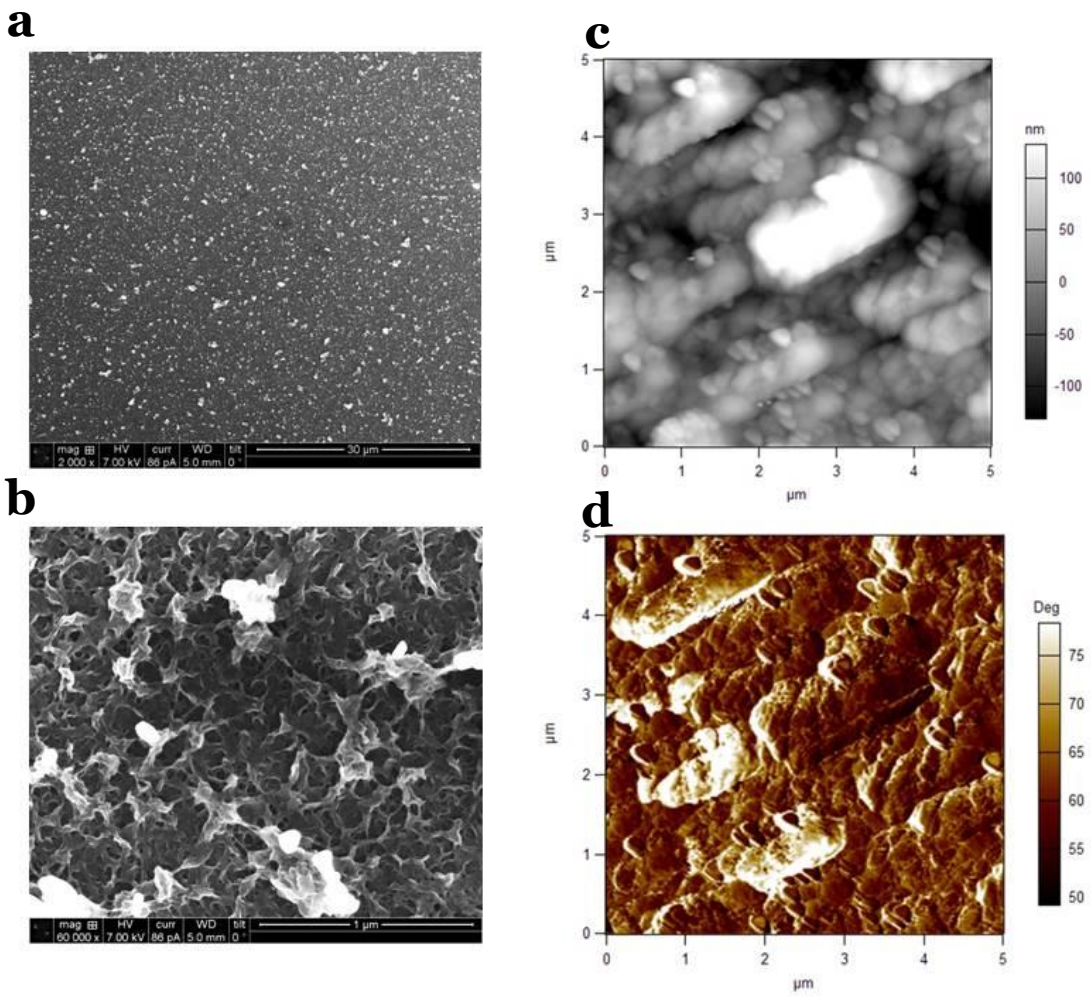


**Figure 2.5.** Film morphology of potentiostatic electropolymerized PEDOT

SEM images at low *(a)* and high *(b)* magnification. *(c)* AFM height image. *(d)* AFM phase image

Morphology is characterized via SEM (**Figure 2.5a & b**) and AFM (**Figure 2.5b & c**). The polymer structure in the SEM images is similar to that of the low-bias PEDOT in section 2.2.2, with dense clusters on the surface of the film connected to a relatively homogenous underlying layer. The AFM height image details the magnitude of one of these surface clusters, which is over 100 nm above the median image height. In fact, the RMS roughness of this film is 64 nm, which is 76% of the average film thickness (84 nm, measured via profilometry). Despite the large surface roughness, the AFM phase at the cluster is nearly identical to the rest of the image. Phase images in AFM are used to determine differences in material properties such as adhesion and viscoelasticity, and a comparable phase most likely means that the surface clusters are compositionally similar to the underlying film.

### *2.2.4 Galvanostatic EPoly PEDOT Films*

Galvanostatic electropolymerizations are performed using an identical gold working electrode, supporting electrolyte concentration, and monomer concentration to the potentiostatic films. A current of 0.75 mA is applied through the cell for 120 s, and the voltage is measured as a function of time (**Figure 2.6a**). At the start of the polymerization an average voltage of approximately 1.13 V is measured at the working electrode. As the polymerization progresses this value decreases, reaching a minimum near 1.02 V at the finish. This is complementary to the potentiostatic case, and the decrease in measured voltage during the experiment indicates that polymer does form on the surface. The UV-Vis spectrum for galvanostatic PEDOT films (**Figure 2.6b**) is nearly identical to that of the potentiostatic PEDOT films, containing one broad absorbance band, indicating a heavily oxidized PEDOT

**a**

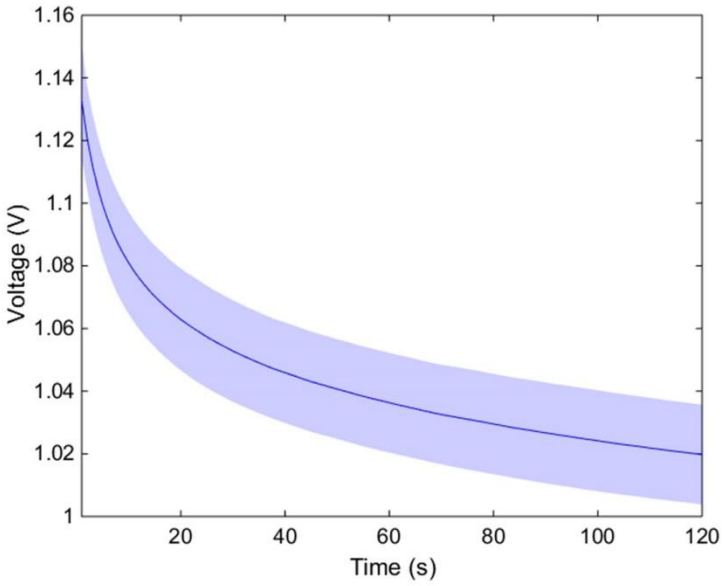


**b**

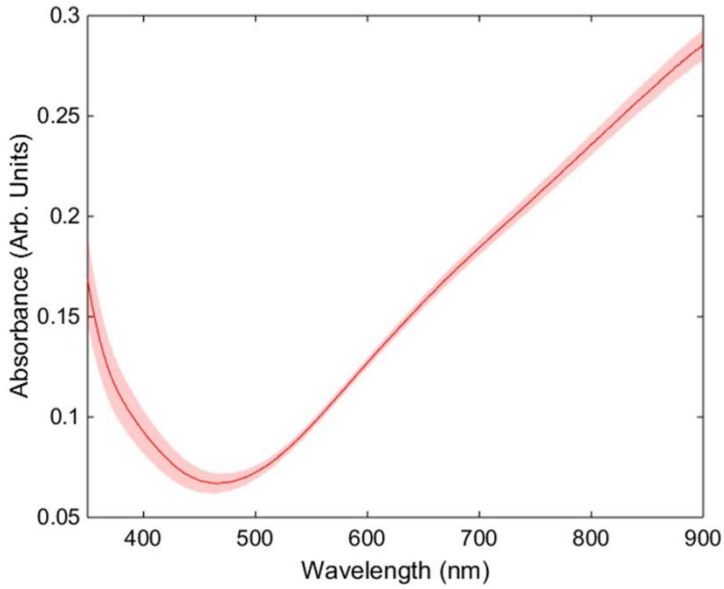


**Figure 2.6.** Galvanostatic electropolymerization of PEDOT

*(a)* Average voltage vs. polymerization time. *(b)* Average UV-Vis spectra for the polymerized films. Shaded bands are 95% confidence intervals.

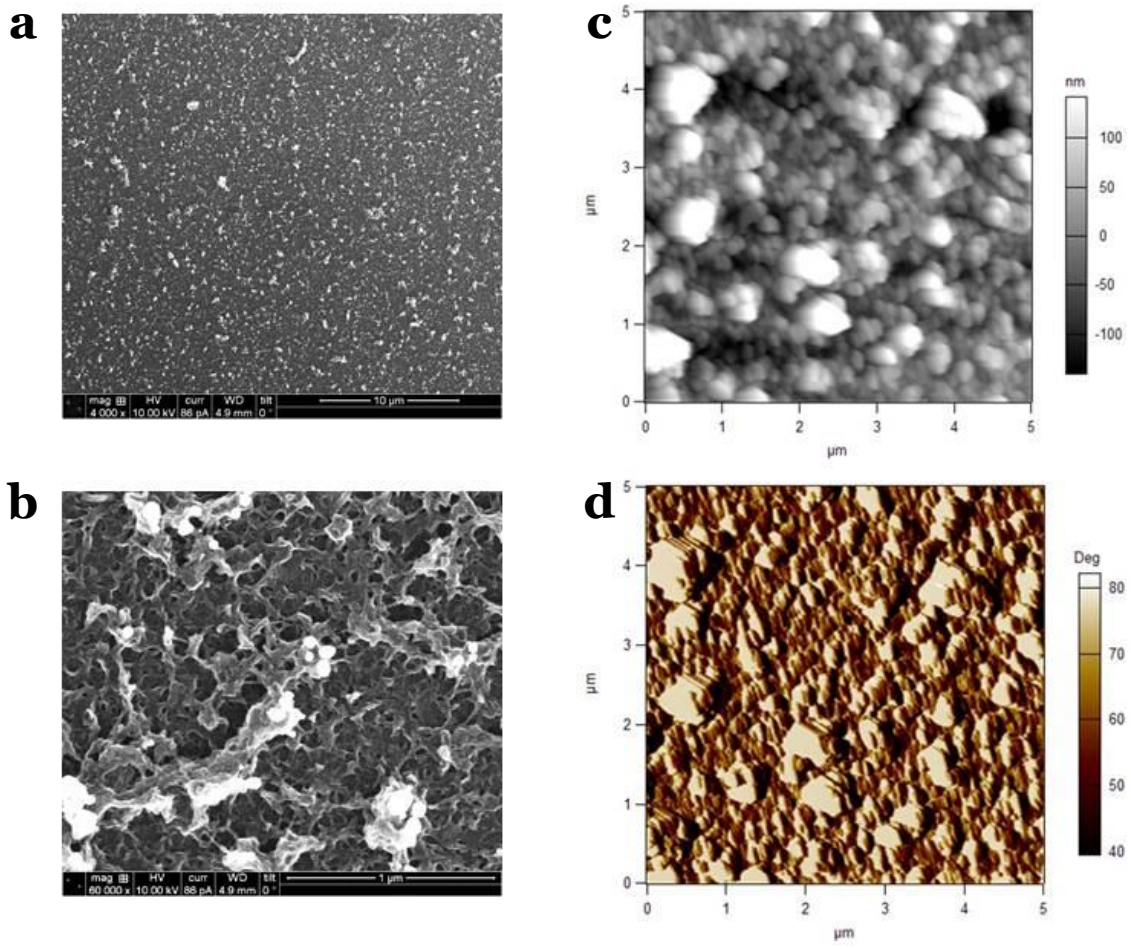


**Figure 2.7** Film morphology of galvanostatic electropolymerized PEDOT

SEM images at low *(a)* and high *(b)* magnification. *(c)* AFM height image. *(d)* AFM phase image.

species. It is also noted that the consistency in the absorbance spectra between samples is greater in the galvanostatic films, though the reason is unknown.

Morphologically, the galvanostatic PEDOT films are extremely similar to the potentiostatic films. SEM images (**Figure 2.7a & b**) illustrate the same type of film structure, containing densely packed surface clusters on top of a semi-porous layer. There appear to be no major differences in the AFM images either **(Figure 2.7c & d**). Although the clusters do appear smaller in the AFM height and phase images when compared with the galvanostatic films, this is most likely due random variations in film structure at these sorts of microscales, and the clusters in the SEM images over larger areas are comparably sized.

*2.2.5 Potentiodynamic EPoly PEDOT Films*

Potentiodyanmic polymerizations are performed in the same experimental setup as the potentiostatic and galvanostatic polymerizations. However, rather than defining a constant electrical value (either voltage or current) and a polymerization time, the voltage is cycled through a series of values for a certain number of repetitions. For the potentiodynamic EPoly PEDOT films, the voltage is swept forward from 0 mV to 1200 mV and returned to 0 mV at a rate of 60 mV/s, and this process is repeated for 10 total cycles (**Figure 2.8a**). On the first cycle oxidation, begins at the working electrode around 900 mV, though this oxidation onset is lowered to approximately 800 mV by the final cycle (**Figure 2.8b**). There also exists an additional oxidation that occurs in later cycles from 0 mV to 200 mV. This is due to a partial reduction in the film during the return sweep, which is then re-oxidized during the subsequent forward sweep. The average UV-Vis spectrum (**Figure 2.8c**) is comparable to the potentiostatic

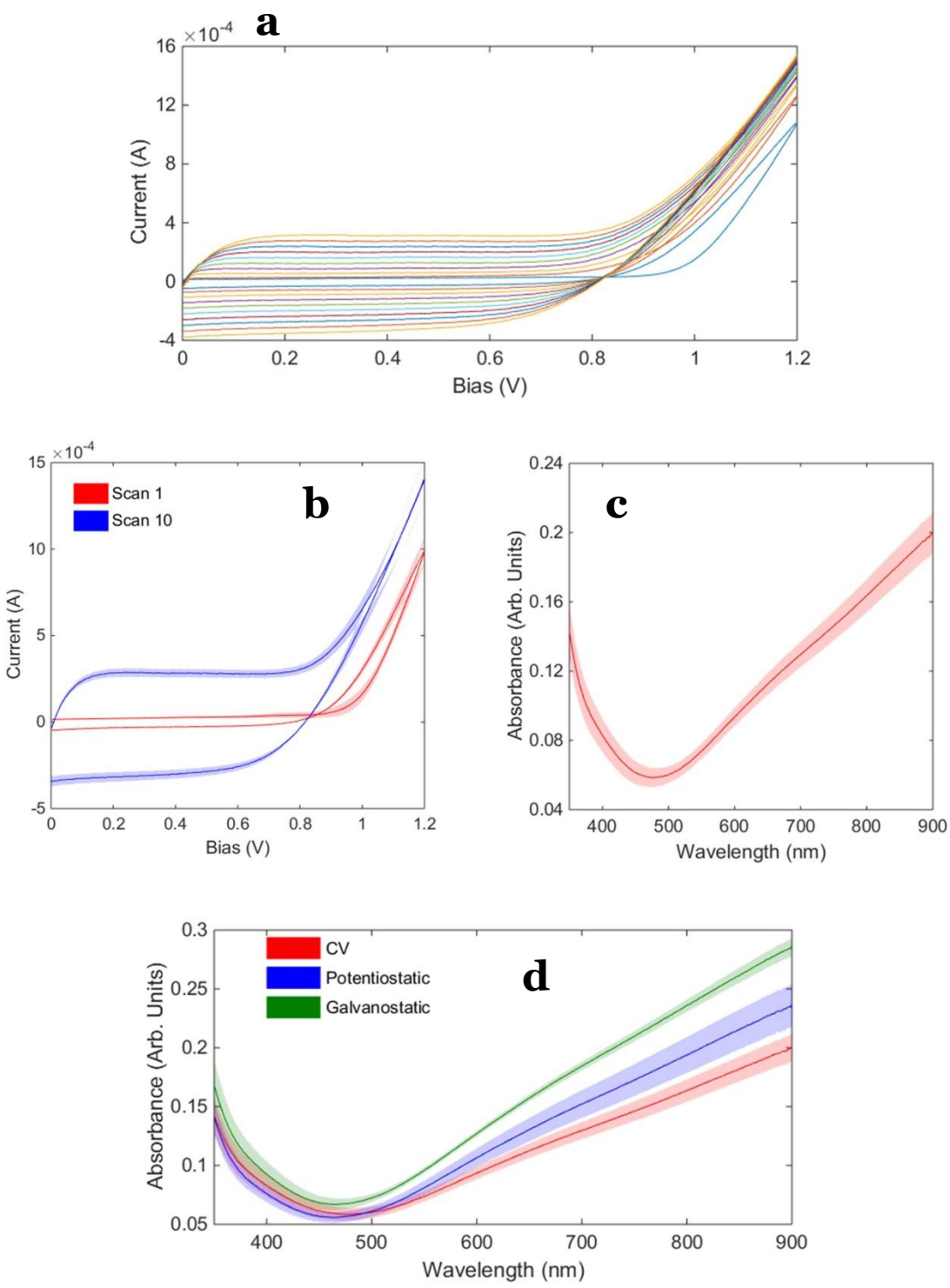


**Figure 2.8.** Potentiodynamic polymerization of PEDOT

*(a)* IV curves of a potentiodyamic EPoly PEDOT film, 60 mV/s for 10 cycles. *(b)* Sample to sample variation of the first and tenth cycle. *(c)* Average UV-Vis spectrum for the potentiodynamically polymerized films. *(d)* UV-Vis spectra for potentiodynamic (CV) potentiostatic, and galvanostatic films. Error bands are 95% confidence intervals.

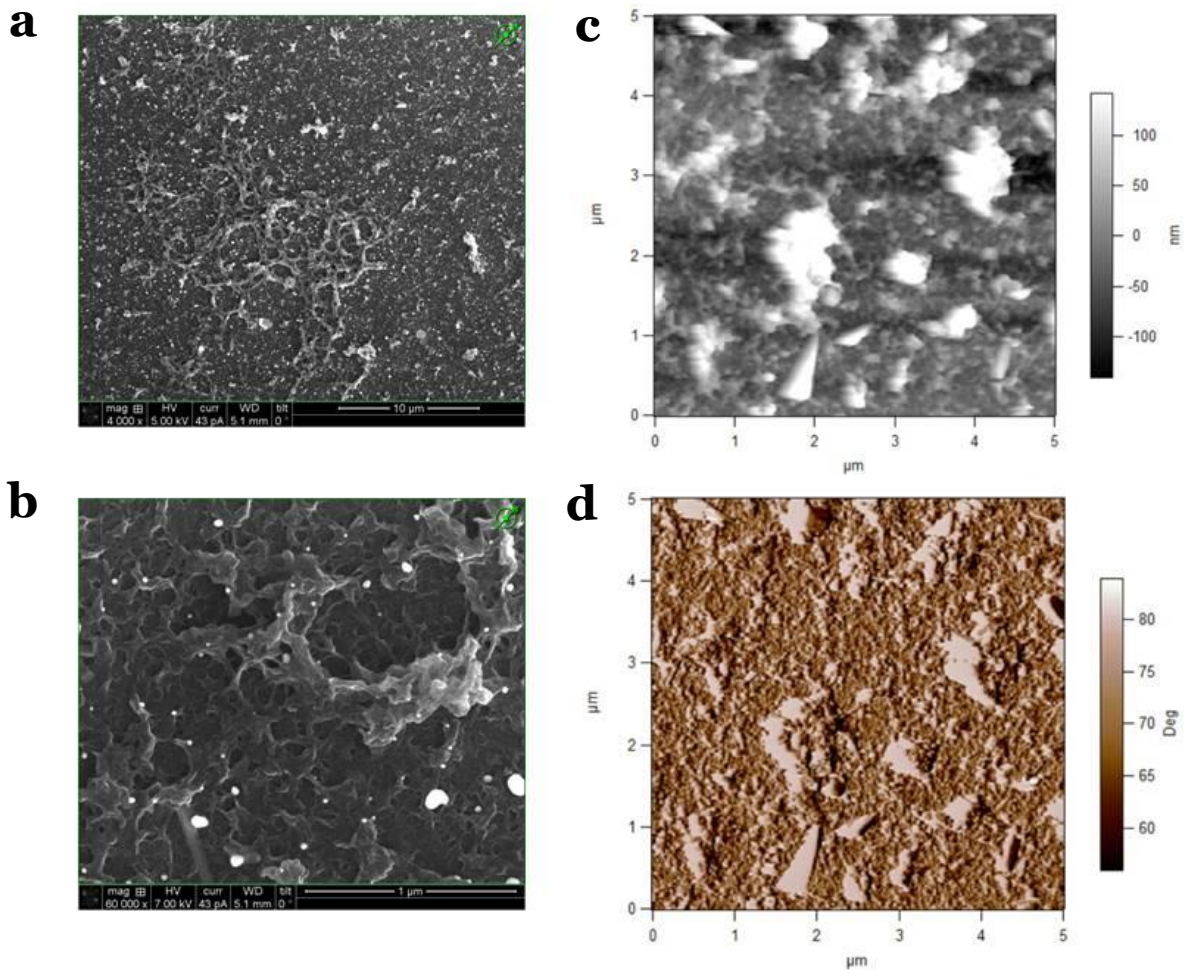


**Figure 2.9.** Film morphology of potentiodynamic electropolymerized PEDOT

SEM images at low *(a)* and high *(b)* magnification. *(c)* AFM height image. *(d)* AFM phase image.

and galvanostatic films, and the spectra of all three films are overlaid in **Figure 2.8d**. There are some differences in the magnitude of the absorbances between the different EPoly conditions due to thickness variations, despite effort to minimize these. Regardless, the spectra in all three cases are quite similar, and are consistent with heavily oxidized PEDOT films.

Morphologically, the potentiodynamic PEDOT films are markedly different than the potentiostatic and galvanostatic films. In the SEM images (**Figure 2.9a & b**) there are now large webs of PEDOT at the surface, rather than simple clusters. These neural-like networks do not exist evenly over the film, but are found locally over regions several hundred $\mu m^2$ in area. The likely cause of these surface networks is that when voltage is swept to sufficiently high values, the polymerization rate increases and creates an inhomogeneous morphology in the film. Excepting these networks, the film is structurally similar to the previous two cases, as the high magnification SEM and AFM images (**Figure 2.9c & d**) show.

Overall three different EPoly methods have been used to grow PEDOT films from a conducting surface. The thermoelectric properties of these films are to be evaluated, but first the charge carrier density must be controlled, the oxidation levels must be understood, and devices must be fabricated.

### *2.2.6 Electrochemical Dedoping of EPoly PEDOT Films*

When PEDOT films are grown via electropolymerization, they are heavily oxidized, and therefore highly doped and electrically conductive. To control the charge carrier density and optimize the thermoelectric properties in the films, a dedoping process must be designed and carried out. As discussed in the introduction, doping or

dedoping of polymers can occur either chemically or electrochemically. Several groups have dedoped PEDOT via chemical reduction,[49–51] but in this study electrochemical reduction was chosen due to its simplicity and consistency with the electropolymerized films.

To electroreduce the PEDOT the films are placed into an acetonitrile bath with a tetrabutylammonium hexafluorophosphate ($TBAPF_6$) supporting electrolyte. A linear voltage sweep is applied starting from zero bias until the desired value is reached, and the voltage is swept at a rate of 10 mV/s. A typical PEDOT dedoping IV curve is displayed in **Figure 2.10a**. From 0 mV to -100 mV, there is a large current increase attributed to the reduction of the bipolarons in the oxidized polymer to polarons. As the voltage is swept to more negative bias, a second peak appears at roughly -600 mV, presumed to be the reduction of the polarons to neutral PEDOT chains.

The UV-Vis spectra of PEDOT films that have been dedoped to various biases support these explanations (**Figure 2.10b, c, & d**). At any dedoping bias, a broad absorbance band appears at 900 nm, and this is consistent with the polaron absorption band in the literature. Unfortunately it is necessary to normalize these spectra to 900 nm to account for sample-to-sample variations in thickness, so it is difficult to comment on the behavior of this peak as the films are dedoped to higher biases. Several methods were attempted at normalization, including dividing the absorbance by the sample thickness, but none produced clearer spectra than normalization at 900 nm. It is evident that even at the highest dedoping biases, significant polaron absorption is still present in the spectra, thus every film contains at least some free charge carriers. The other absorption peak is located at approximately 600 nm, and it is attributed to neutral

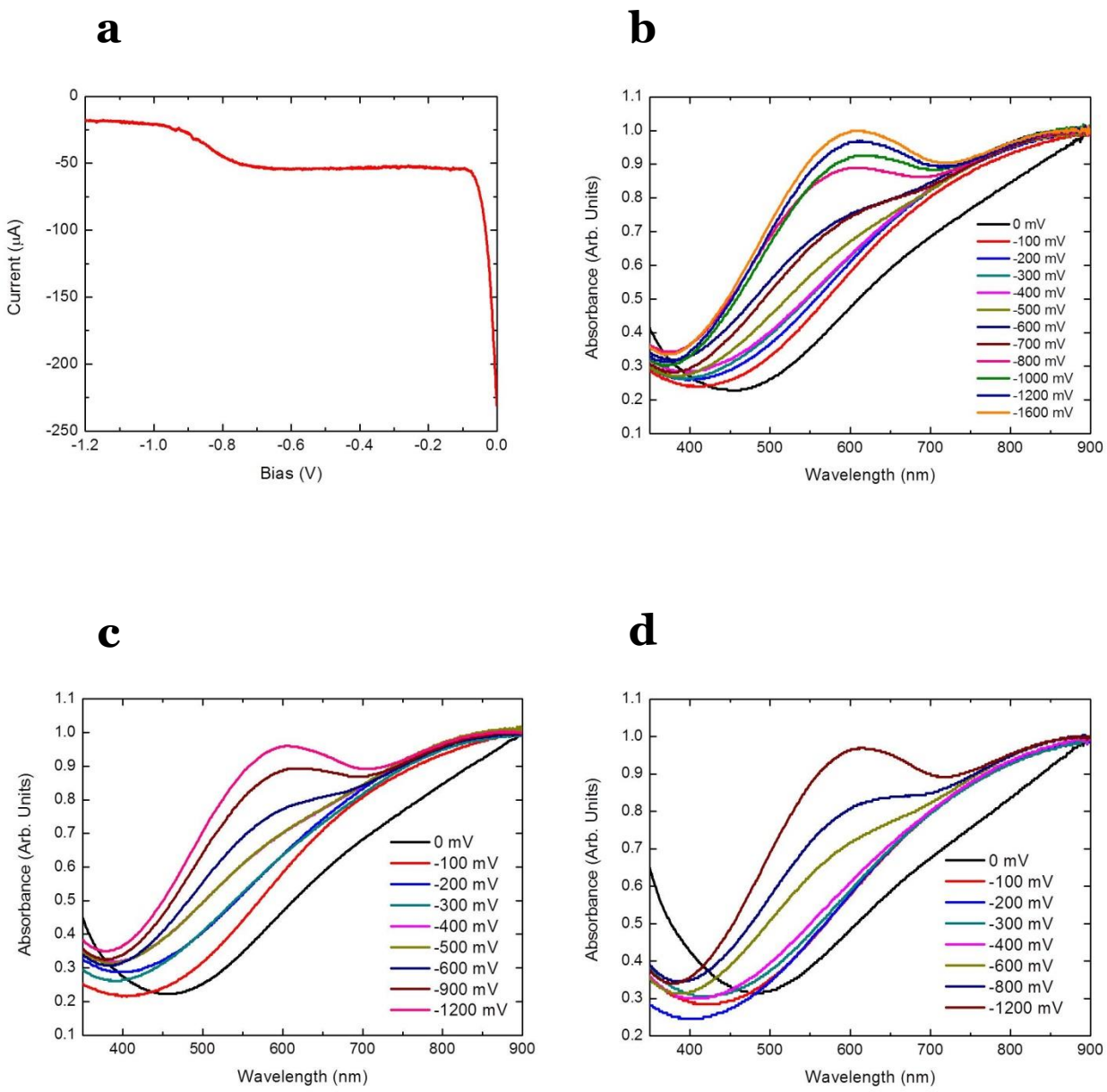


**Figure 2.10.** Electrochemical dedoping of EPoly PEDOT Films

*(a)* Linear sweep dedoping IV curve of an EPoly PEDOT film. *(b)* Potentiostatic *(c)* galvanostatic and *(d)* potentiodynamic UV-Vis spectra at different dedoping biases.

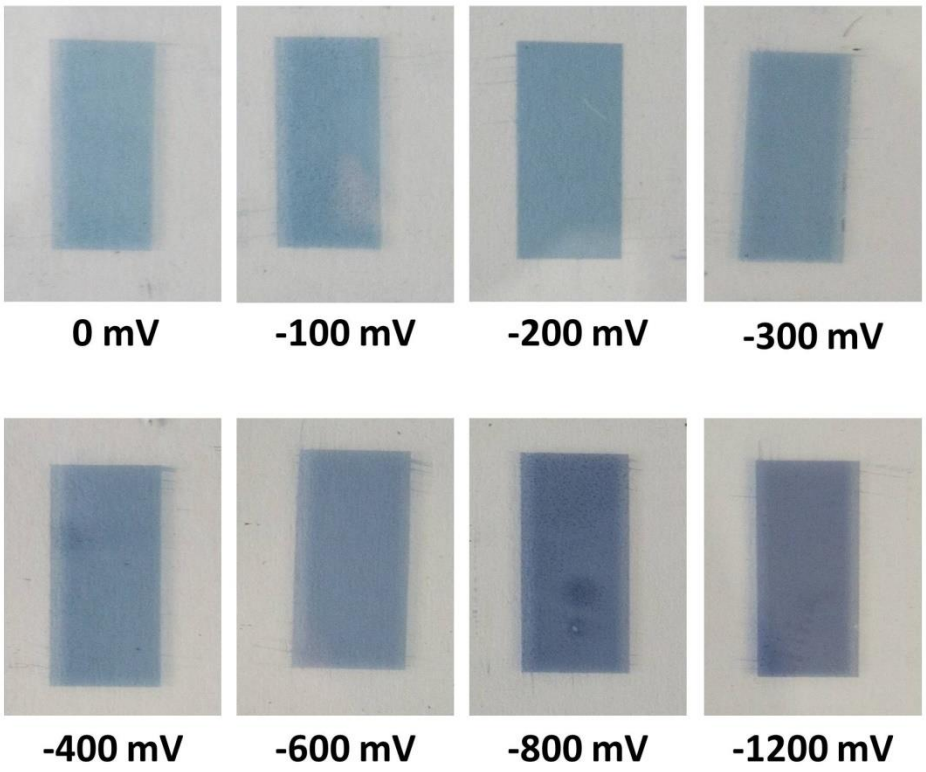


**Figure 2.11.** Photographs of dedoped potentiodynamic PEDOT films

PEDOT absorption. This peak is not present at low dedoping biases, but appears at higher dedoping biases and is largest at the highest biases. This fits with the dedoping IV curve. Photographs of PEDOT films that have been dedoped to various biases are given in **Figure 2.11**. At no or low dedoping biases the films are a pale blue in color, while at dedoping biases above -600 mV, they transition to an indigo color.

### *2.2.7 Oxidation Levels of EPoly PEDOT Films*

Though UV-Vis spectroscopy gives some information about the oxidation levels of the electropolymerized and electrochemically-dedoped PEDOT films, it is certainly not a quantitative way to measure these levels. X-ray photoelectron spectroscopy (XPS) is a technique that has been used previously to determine oxidation levels in PEDOT films.[55,108] In XPS, radiation in the x-ray regime is fired at the surface of a sample (0-10 nm penetration depth). These x-rays cause electrons from atoms at the surface to be ejected, and the instrument subsequently detects their numbers and energies. The kinetic energies of the detected electrons can be related to the binding energy at which they originally existed in the atoms. This binding energy is unique for different electronic environments, making XPS a useful tool to measure surface elemental composition, changes in surface oxidation state, changes in surface binding, etc.

The EPoly PEDOT films contain polarons and bipolarons that must be counterbalanced by anions. Because the films are polymerized oxidatively, the counterions are integrated into the PEDOT during its polymerization from the electrochemical solution. $PF_6^-$ is the likely counter ion because of its presence as the electrolyte during solution, and so by measuring the XPS intensity of the phosphorus, fluorine, and sulfur, the oxidation levels can be measured from their ratios.

EPoly PEDOT films were prepared and dedoped at biases of 0 mV (fully doped), -400 mV, -800 mV, and -1200 mV. XPS was performed on all four samples and the atomic concentrations were calculated from the peak intensities (**Table 2.1**).

**Table 2.1.** XPS-determined atomic concentration in dedoped PEDOT films

| *Dedoping Bias (mV)* | *Peak Identity* | *Atomic Concentration %* |
|---|---|---|
| 0 | C 1s | 54.9 |
| | F 1s | 18.0 |
| | S 2p | 7.65 |
| | P 2p | 2.62 |
| -400 | C 1s | 75.6 |
| | F 1s | 12.7 |
| | S 2p | 9.58 |
| | P 2p | 1.90 |
| -800 | C 1s | 78.7 |
| | F 1s | 9.33 |
| | S 2p | 10.5 |
| | P 2p | 1.49 |
| -1200 | C 1s | 80.0 |
| | F 1s | 8.25 |
| | S 2p | 10.6 |
| | P 2p | 1.24 |

From the sulfur:phosphorus concentration ratio, the oxidation level is determined (**Table 2.2**).

**Table 2.2.** Oxidation levels of dedoped EPoly PEDOT films

| *Dedoping Bias (mV)* | *S:P Concentration Ratio* | *Oxidation Level (%)* |
|---|---|---|
| 0 | 3.03:1 | 33.0 |
| -400 | 5.04:1 | 19.8 |
| -800 | 7.05:1 | 14.2 |
| -1200 | 8.55:1 | 11.7 |

An oxidation level of 100% would indicate that every EDOT unit was charged and counterbalanced with a $PF_6^-$ anion, and therefore based on these oxidation levels positive charges exist on anywhere from 1 out of 3 to 1 out of 9 EDOT units. These oxidation levels are in line with those seen in other PEDOT-type devices.[55,57]

*2.2.8 Electrical Conductivity of EPoly PEDOT Films*

The electrical conductivity of the PEDOT films cannot be measured while the films are in contact with the gold layer, because the gold is several orders of magnitude more conductive than the PEDOT. Several methods were attempted to remove the PEDOT from the gold, including transfer printing, removing the PEDOT with tape, and scraping the PEDOT from the gold. However, none of these proved successful, resulting in incomplete transfer and cracked films. Instead, the gold was removed from underneath the PEDOT through a chemical etching process. Aqua Regia (3:1 hydrochloric:nitric acid) was used as the etchant and the EPoly PEDOT films were submerged in the acid until the gold was dissolved. If the gold layer was sufficiently thin (< 30 nm), the PEDOT remained adhered to the glass slide. A concern with the acid etching process was re-oxidation of the PEDOT films after they were dedoped. To mitigate this, the acid etch was performed immediately after polymerization when the PEDOT was doped maximally, and the conductive PEDOT layer was used as the working electrode for dedoping.

Once the gold was removed from the PEDOT layer, the electrical conductivity could be measured in a 4-point probe setup using the van der Pauw method. If four contacts of insignificant area are placed at the edge of the sample and numbered 1 - 4, the resistance of the sample can be measured by sourcing a current between contacts 1 &

2 and measuring the resultant voltage generated between contacts 3 & 4. This resistance value is designated as $R_{1234}$. The current and voltage loops are then switched to the opposite pairs of contacts, and $R_{3412}$ is measured as well. $R_{1423}$ and $R_{2314}$ are determined similarly, and these two pairs of resistances are averaged.

$$R_v = \frac{R_{1234} + R_{3412}}{2} \tag{6}$$

$$R_h = \frac{R_{1423} + R_{3412}}{2} \tag{7}$$

Where $R_v$ and $R_h$ are the sample resistance values in the vertical and horizontal directions, respectively. The sheet resistance $R_s$ can be calculated by solving (8).

$$e^{-\frac{\pi R_v}{R_s}} + e^{-\frac{\pi R_h}{R_s}} = 1 \tag{8}$$

Finally, the conductivity σ can be related to $R_s$ and the measured film thickness t.

$$\sigma = \frac{1}{R_s t} \tag{9}$$

The electrical conductivities of all polymerized films were determined in this manner, and their values are presented with the thermoelectric data in section 2.2.9.

*2.2.9 Thermoelectric Data of EPoly PEDOT Films*

The parameters of interest for these films are the electrical conductivity, the Seebeck coefficient, and the power factor ($\sigma S^2$). The Seebeck coefficient measurement requires device fabrication to place macroscopic electrical leads onto the PEDOT films. This is accomplished by sputtering two gold contacts and attaching the leads via silver

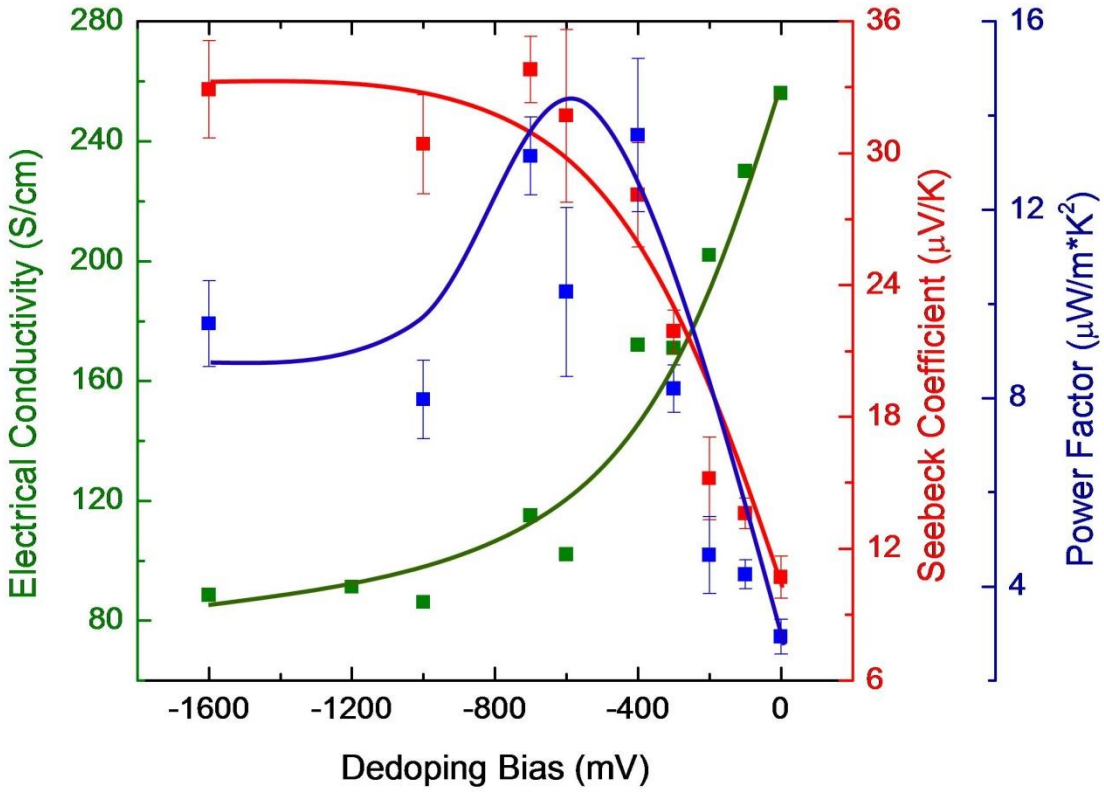


**Figure 2.12.** Thermoelectric properties of potentiostatic EPoly PEDOT Films

epoxy to the contacts. To measure the Seebeck coefficient, a temperature gradient was applied along the device, and the voltage was measured at the two electrical contacts. The temperature was recorded near the contacts with two thermocouples, and the Seebeck coefficient was determined from these values.

The expected behavior with a greater amount of dedoping is that the electrical conductivity will decrease, the Seebeck coefficient will increase, and there will be a dedoping level where the power factor is maximized. This expected behavior is consistent with what is observed for potentiostatic PEDOT films (**Figure 2.12**). The electrical conductivity is 256 S/cm in the fully oxidized film, and decreases exponentially to a value of 89 S/cm at -1600 mV dedoping bias. The opposite trend is observed for the Seebeck coefficient, where there is a minimum value of 10.7 μV/K with no dedoping, and an increase to 32.9 μV/K at maximum dedoping. Therefore the power factor is maximized at a dedoping bias of -400 mV, and this maximum value is 13.6 μW $m^{-1}$ $K^{-2}$. These results indicate that these EPoly PEDOT films are viable thermoelectric materials.

The thermoelectric properties of the galvanostatic and potentiodynamic EPoly PEDOT films are displayed in **Figure 2.13**. In the galvanostatic case, the electrical conductivities are quite similar to the potentiostatic values. This is to be expected based on the similarities in morphology and the UV-Vis spectra. However, the Seebeck coefficients at low dedoping biases (0 to -1000 mV) are smaller than those in the potentiostatic case, so the maximized power factor is smaller as well (10.3 μW $m^{-1}$ $K^{-2}$). It is not completely understood why this decrease occurs, although it is possibly due to a less efficient dedoping process, meaning that the oxidation levels in the galvanostatic

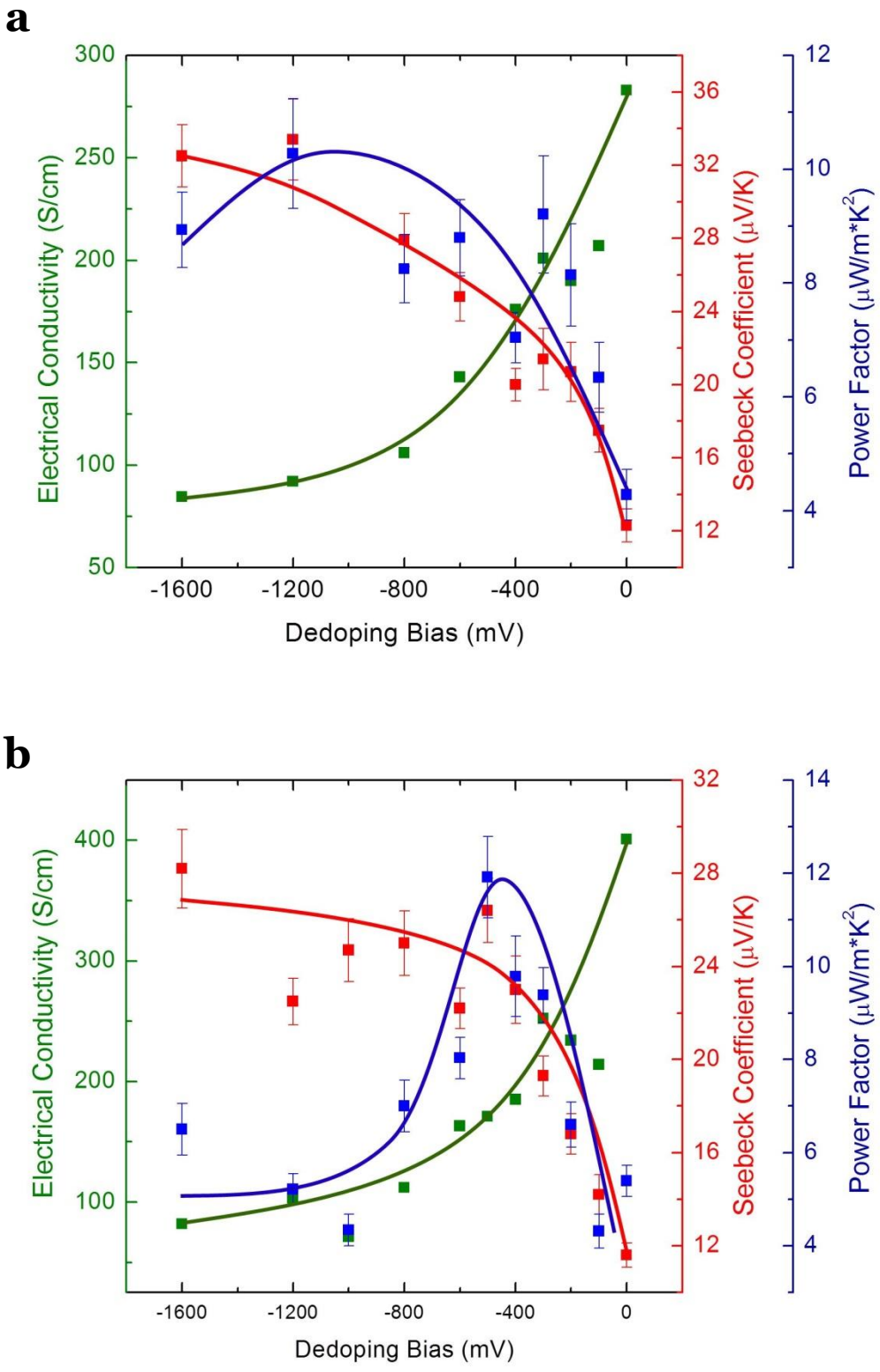


**Figure 2.13.** TE properties of galvanostatic and potentiodynamic EPoly PEDOT Films

*(a)* Thermoelectric properties of galvanostatic PEDOT films. *(b)* Thermoelectric properties of potentiodynamic PEDOT films. All lines are added manually as guides for the eye.

films are different from those in the potentiostatic films at the same dedoping bias. Current work is being done using XPS to elucidate these effects.

In the potentiodynamic films, the electrical conductivity with no dedoping is 401 S/cm, an increase of 57% over the fully doped potentiostatic films and a 42% increase over the fully-doped galvanostatic films. This increase is attributed to the morphology change that occurs in the potentiodynamic films, namely the formation of dense networks of PEDOT. These networks likely lead to increased charge transport which results in increased conductivity. The Seebeck coefficients in the potentiodynamic PEDOT are lower than those in the potentiostatic films, likely due to the increased electrical conductivity. Because the power factor depends on the square of the Seebeck coefficient, the maximum PF in the potentiodynamic films (11.9 $\mu W/m*K^2$) is lower than the respective value in the potentiostatic PEDOT.

All three polymerization techniques produce films that are thermoelectrically useful. However, the power factors are lower than some others have reported for PEDOT-type materials. This is largely due to the relatively low electrical conductivities in these films. Because PEDOT polymerized electrically is morphologically fixed, it is difficult to create the intra-chain and π-π interactions that are needed for highly conductive materials. A way forward may be to develop annealing procedures for these EPoly films, changing the morphology either with a thermal or chemical treatment to improve conductivity.

## 2.3 Conclusions

PEDOT-based thermoelectric materials were developed via an electropolymerization technique. It was determined that both polymerization rate and

final thickness affected the homogeneity of the film, with thinner films and those polymerized at slower rates being of higher quality. PEDOT thin films were grown using potentiostatic, galvanostatic, and potentiodynamic techniques, and their morphology was characterized via SEM and AFM. Potentiostatic and galvanostatic films shared very similar morphologies, but potentiodynamic films were quite different owing to the dense surface networks that did not exist in the other two cases. The films were dedoped electrochemically to control oxidation levels, and these levels were measured via XPS. The electrical conductivity, Seebeck coefficient, and power factor were determined for all three techniques. Potentiostatic PEDOT films showed the largest power factor (13.6 $\mu W/m*K^2$) due to their large Seebeck coefficients, and potentiodynamic films were the most conductive (401 S/cm). All three electropolymerzation techniques produced films that were thermoelectrically active, and future work will focus on improving the conductivity of these thin-films in order to increase performance.

## 2.4 Experimental

### *2.4.1 General Methods*

All chemicals were used without further purification unless otherwise noted. All polymerizations were carried out in a three-electrode potentiostat (Epsilon Electrochemistry, *Bioanalytical Systems Inc.*). Metal evaporations were conducted in an integrated glovebox system under an inert environment (MB-Evap, *MBraun*). Sputter coating was performed in a Kurt Lesker system (PVD 75, *Kurt Lesker*). AFM measurements were made using an Asylum AFM (MFP-3D, *Asylum Research*), and data processing was done in IGOR (*Wavemetrics*). Electrical measurements were taken on a micro-manipulated probe station (1160 Series, *Signatone*) integrated with a Keithley

2636B Sourcemeter. SEM images were taken on an FEI instrument (Helios 600 Nanolab Dualbeam, *FEI*). UV-Vis spectra were taken on a Shimadzu instrument (UV-2600, *Shimadzu Corporation*). XPS spectra were collected via a Kratos Spectrometer (Axis Ultra DLD, *Kratos Analytical*). Sample thickness was determined via profilometry (D100, *KLA Tencor*).

### *2.4.2 Preparation of Gold Working Electrodes*

Glass slides were cut to 25 × 40 mm, and submerged in a solution of deionized water, ammonium hydroxide (14.8 M, *Fisher Scientific*), and hydrogen peroxide (30%, *Fisher Scientific*) in a 2:1:1 ratio for 20 minutes. The slides were removed from the solution, copiously rinsed with deionized water and ethanol (100%, *Decon Laboratories Inc.*), and dried under a jet of nitrogen. The glass slides undergo further cleaning in a UV ozone cleaner (Model 42A, *Jelight Company Inc.*) for 20 minutes. They were then attached to a holder, placed inside the evaporation system, and the system was evacuated to a pressure of $3 \times 10^{-6}$ mbar. Gold was evaporated at 1 Å/s for 3 nm, and then the rate was increased to 10 Å/s until a final thickness of 20 nm was achieved.

### *2.4.3 Electropolymerization of EDOT*

To a screw cap bottle filled with acetonitrile (Optima grade, *Fisher Scientific*), EDOT (97%, *Sigma-Aldrich*) and Bmim $PF_6$ (98%, *Alfa Aesar*) were each added to a final concentration of 0.01 M, and this solution was allowed to stir for 30 minutes. 30 mL of the solution was poured into a glass staining dish. The gold working electrode, a platinum wire counter electrode, and a $Ag/AgNO_3$ reference electrode were submerged into the solution. For potentiostatic polymerizations, 1025 mV was applied to the working electrode for 120 s. For galvanostatic polymerizations, 0.75 mA was applied to

the working electrode. For potentiodynamic polymerizations, the voltage was swept from 0 mV to 1200 mV and returned to 0 mV, at a rate of 60 mV/s, and this was repeated 10 times. In each case after the polymerization was finished, the PEDOT-coated working electrode was removed from the solution, rinsed 3x with acetonitrile, and blown dry with $N_2$. The reference electrode, counter electrode, and staining dish were similarly cleaned and the process was repeated for any remaining working electrodes.

### *2.4.4 Electrochemical Dedoping of PEDOT films*

To remove the gold metal layer, a 3:1 solution of hydrochloric acid (12.1 M, *Fisher Scientific*) to nitric acid (15.9 M, *Fisher Scientific*) was prepared in a glass beaker. The sample was submerged in the solution for 40 s and subsequently removed. It was rinsed with deionized water and blown dry via $N_2$. For the dedoping process, a 0.1 M solution of tetrabutylammonium hexaflurophosphate (Electrochemical Grade, *Fluka*) was prepared in acetonitrile, and 20 mL of this solution was added to a staining dish. The PEDOT coated working electrode, platinum wire counter electrode, and $Ag/AgNO_3$ reference electrode were placed in the solution. Bias was applied to the working electrode in a linear sweep from 0 mV to the desired end value, anywhere from -100 mV to -1600 mV. The dedoped PEDOT was then removed from the bath and rinsed with acetonitrile, then blown dry with $N_2$.

### *2.4.5 Electrical Measurements and Device Fabrication*

Electrical conductivity was measured using the van der Pauw technique as described in section 2.4.5. The dedoped PEDOT films were trimmed to 12.7 x 6.4 mm with a razor blade in order to eliminate any edge defects before they were measured.

Once the electrical conductivity had been determined, two gold top contacts were sputter deposited through a shadow mask. The contacts were 12.7 mm x 2.0 mm and were spaced by 6.4 mm. The final fabrication step was the attachment of the voltage measurement leads to the devices. 32 AWG insulated copper wire was stripped and attached to the gold contacts via silver epoxy (*MG Chemicals*). The epoxy was allowed to cure overnight.

### *2.4.6 Determination of Seebeck Coefficient*

The Seebeck coefficients of EPoly PEDOT films were determined using a home-built setup. A copper block approximately 1 cm × 5 cm × 8 cm was placed onto a hot plate, and an additional block was placed onto a lab jack next to the hot plate. The spacing between the blocks was 12.7 mm. Insulating thermal paste (Type 120 Silcone, *Wakefield Solutions*) was coated onto the underside of a PEDOT device, and the device was affixed onto the blocks and secured with tape. The two wire leads were attached to a voltage measurement system (Model 100, *Instrunet*), and two k-type thermocouples were placed onto the device near the voltage leads. It was important that the thermocouples were electrically insulated from the voltage leads so that their thermovoltages did not interfere with the measurement. Once the setup was ready the hot plate was turned on and allowed to heat the sample to approximately 45 °C, and the temperature and voltage differences along the sample were recorded once the temperature difference reaches > 5 °C. In this way > 1000 measurements could be collected in a short amount of time.

# *Chapter 3*
# CHEMICAL DOPING AND CONDUCTIVITY STUDIES OF TWO STRUCTURALLY-ANALOGOUS POLYMERS

## 3.1 Introduction to TE Polymer Structure-Property Relationships

### *3.1.1 Background*

Chapter 2 demonstrated progress towards high-performance organic thermoelectric materials, and in fact the thermoelectric performance of conducting polymers, especially PEDOT, has increased significantly in recent years. Though organic thermoelectric materials are currently not on par with their inorganic counterparts, it is extremely important to continue device engineering and optimization studies to improve the overall efficiencies of organic TE devices. Equally important however, are more fundamental studies that attempt to correlate polymer structure to device performance. Understanding these structure-property relationships as they relate to electrical conductivity, Seebeck coefficient, and thermal conductivity will allow for the rational design of future thermoelectric polymers.

Towards these goals, several groups have studied controlled series of polymers, including poly(*p*-phenylene vinylenes)[109], polycarbazoles[39,40], and polythiophenes[41,42,110]. It was discovered that though electrical conductivity is elevated through an increase in chain packing density, the Seebeck coefficient is unaffected, thus power factor is maximized in densely-packed films.[41] Additionally, the substitution of nitrogen or fluorine into the polymer backbone leads to a larger power factor by increasing the polymer mobility.[40,109] Despite these examples, more work needs to be

done to further elucidate structure-property relationships in thermoelectric polymers. Fortunately, the OPV, OFET, and OLED communities, including our group, have made great strides in determining the detailed structure and morphology of several conjugated polymers. By leveraging this knowledge, polymers can be electrically and thermoelectrically characterized and conclusions can be drawn from the prior body of work.

### *3.1.2 Introduction to PHTAZ and PFTAZ*

PBnDT-HTAZ (HTAZ) and PBnDT-FTAZ (FTAZ) are two polymers that have been recently synthesized and characterized by our group.[111–114] They are composed of a benzodithiophene donor moiety with a benzotriazole acceptor moiety, and are structurally-identical except for two fluorine substitutions on the benzotriazole in the case of FTAZ (**Figure 3.1**). The optical and electrical properties of the two polymers are listed in **Table 3.1.**

**Table 3.1.** Optical and electrical properties of HTAZ and FTAZ

| *Polymer* | *Film $E_g$ (eV)* | *HOMO (eV)* | *LUMO (eV)* | *Mobility ($cm^2/Vs$)* |
|---|---|---|---|---|
| HTAZ | 1.98 | -5.29 | -2.87 | $3.34 \times 10^{-6}$ |
| FTAZ | 2.00 | -5.36 | -3.05 | $6.76 \times 10^{-5}$ |

Based on the similarities in polymer structure, it is not surprising that the energy levels between the two are only minimally different. However, the SCLC mobility is nearly an order of magnitude higher in FTAZ than in HTAZ. This arises from the fluorine impacting the polymer packing, where the face-on stacking is increased in the fluorinated polymer, leading to greater π-π interactions. An increase in mobility allows for an increase in electrical conductivity without a subsequent rise in the density of

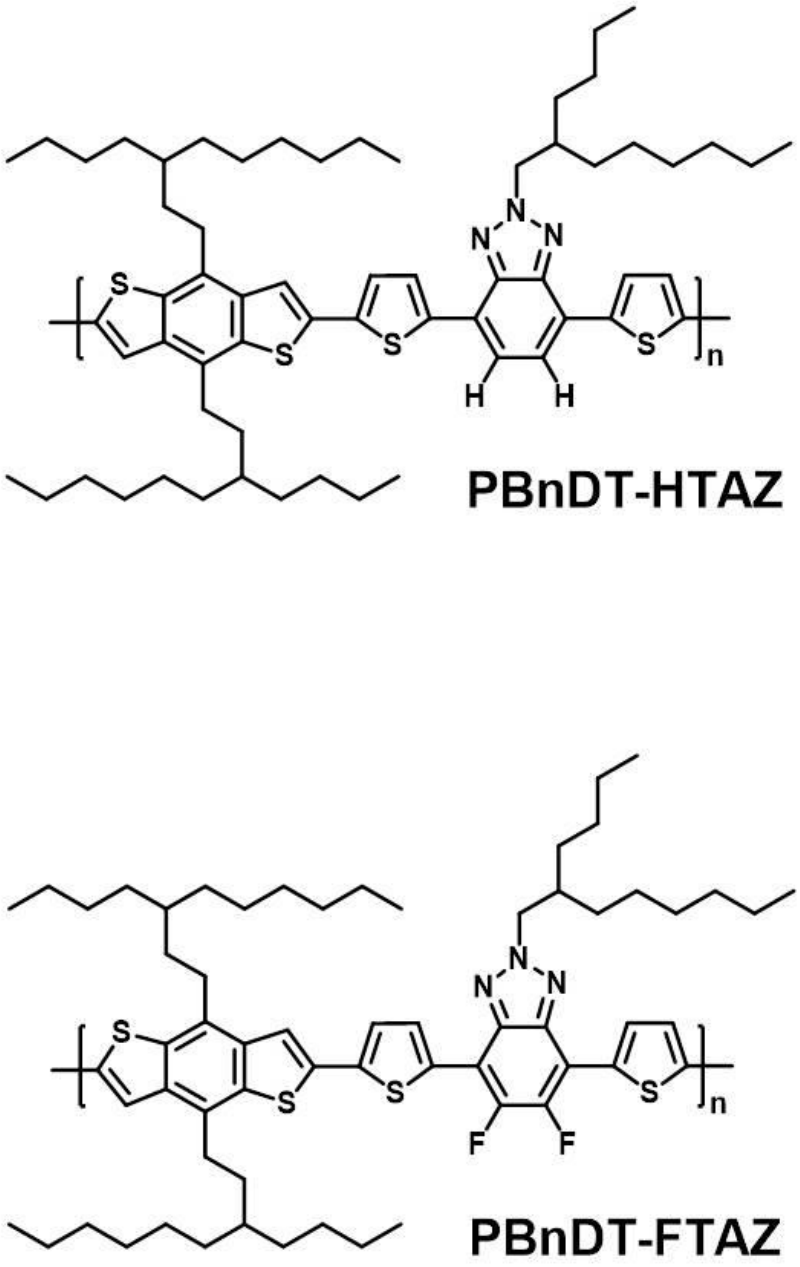


**Figure 3.1.** Polymer structures of PnDT-HTAZ and PnDT-FTAZ

charge carriers in the film. These carriers lower the Seebeck coefficient in a material, and so higher mobility materials are expected to perform better thermoelectrically. Because the structures of HTAZ and BnDT FTAZ are so alike, and yet the mobilities are so different, they present an interesting case study on the direct impact of mobility on thermoelectric performance in organic materials.

In this chapter, HTAZ and FTAZ polymers will be studied. They will be doped to control charge carrier density and their electrical conductivity will be measured. Furthermore, the doping stabilities will be examined and compared between the two polymers.

## 3.2 Results and Discussion

### *3.2.1 Doping of HTAZ and FTAZ*

Both HTAZ and FTAZ are polymerized as neutral polymers, meaning they have no free charge carriers and an intrinsically low electrical conductivity. To increase this conductivity, either chemical or electrochemical doping should be performed. In our case, FTAZ was electrochemically doped by applying a positive bias to an ITO working electrode onto which the polymer film was spun-cast. However, after doping, the polymer needs to be removed from the working electrode for further characterization, or the working electrode must be etched away. Attempts at removing the polymer from the working electrode were unsuccessful due to the fragility of the thin film, so an ITO etch was considered. ITO can be etched in concentrated hydrochloric acid with zinc powder, but unfortunately it is known in the literature that strong acids will chemically dope conjugated polymer materials.[115] This secondary acid doping process does not allow for a controllable doping level in the polymer. Furthermore, other metal working electrodes

are similarly etched in acidic solutions, making them incompatible with any controlled doping process.

The difficulties with electrochemical doping of FTAZ meant that a chemical doping process would need to be developed. Here, an oxidant is added either into a polymer solution before the film is cast, or as a post-treatment in a previously formed film. One of the best known doping oxidants is ferric chloride ($FeCl_3$), which has been used for many years on a variety of polymer systems.[33,116,117] In $FeCl_3$ doping the iron(III) center acts as an oxidizing agent, removing an electron from a polymer chain to form $FeCl_2$. The free $Cl^-$ can then complex with another $FeCl_3$ molecule to form $FeCl_4^-$, which acts as a counterion with the newly-formed polymer polarons and bipolarons. Initial attempts were made by mixing $FeCl_3$ and FTAZ in various solvents and spin-casting films from these solutions, but solvents that could dissolve the polymer and the dopant equally well were not found. A more viable strategy was established by casting FTAZ into a film, and post-treating it in a solution of the iron-based dopant. The degree of doping can then be controlled by varying either the amount of doping time, or the concentration of the $FeCl_3$ in solution. Generally, controlling the amount of dopant is more predictable if the dopant concentration is varied instead of the doping time.

The doping level in HTAZ and FTAZ can be monitored via UV-Vis. The normalized absorption spectra of the neutral polymers are extremely similar (**Figure 3.2a**). Both HTAZ and FTAZ have an onset absorption near 650 nm, consistent with their reported bandgaps. Additionally, there are no absorbances at longer wavelengths, indicating the polymer films are entirely neutral. Once the films are

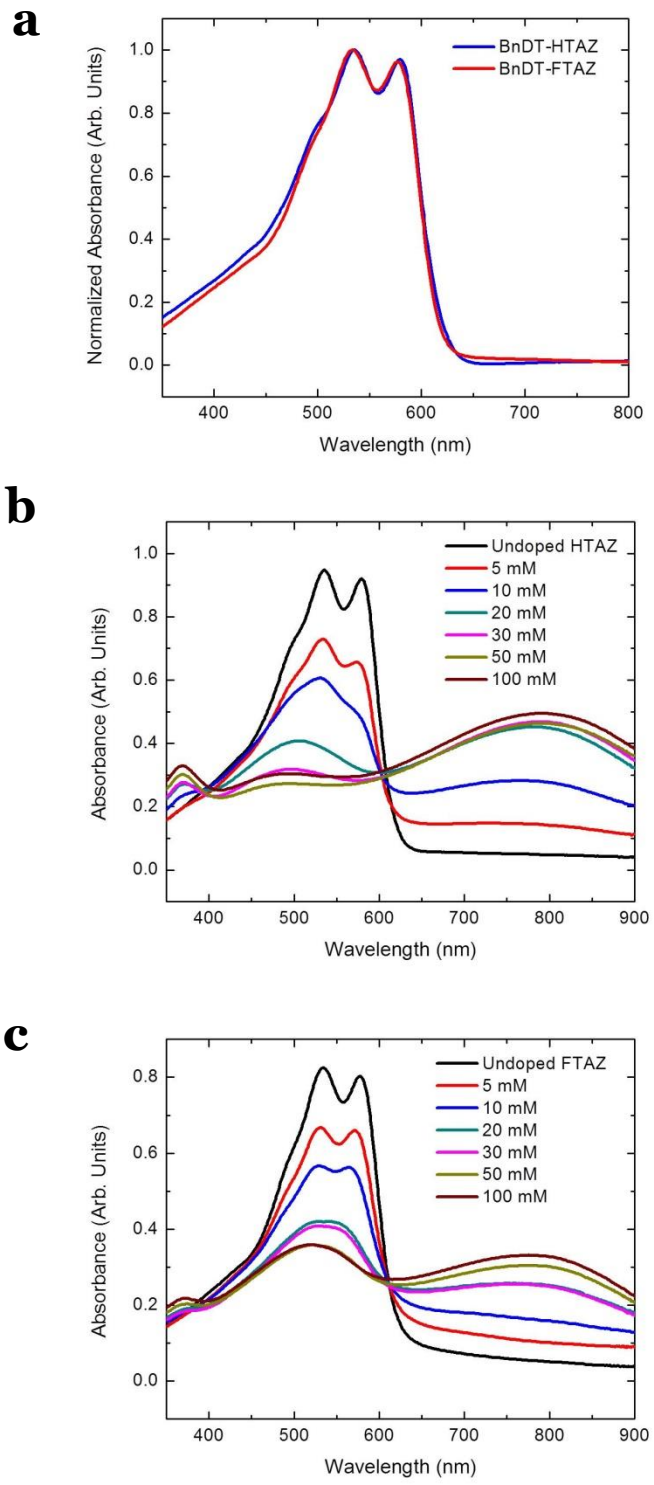


**Figure 3.2.** UV-Vis spectra of HTAZ and FTAZ.

*(a)* Normalized absorbance spectra for HTAZ and FTAZ polymer films. *(b)* HTAZ UV-Vis spectra at different $FeCl_3$ doping concentrations. Doping time is 20 s. *(c)* FTAZ UV-Vis spectra at different $FeCl_3$ doping concentrations. Doping time is 20 s.

treated with $FeCl_3$, a new absorption peak arises at approximately 790 nm in both cases (**Figure 3.2b & c**). This peak is attributed to free charge carriers (most likely polarons) that are generated during the doping step. There is also likely a bipolaron absorption peak in the NIR, outside the range of these spectra. As the dopant concentration increases the neutral absorption peak decreases in intensity, and at the highest $FeCl_3$ concentrations the charged absorption peak either equals or surpasses the intensity of the neutral peak. The FTAZ analogue appears to be less doped at similar concentrations when compared with HTAZ, though the reason behind this is not currently understood. What can be concluded is that both the HTAZ and FTAZ can be successfully doped with $FeCl_3$, and the degree of doping can be tailored by controlling the concentration of the dopant solution.

### *3.2.2 Stability of the Doped HTAZ and BnDT FTAZ Films*

Though the doping of HTAZ and FTAZ films readily proceeds in the presence of $FeCl_3$, the stability of these doped polymers is unknown. Previous reports have indicated that dedoping of poly(alkylthiophene)-based polymers will occur via numerous mechanisms, including thermal,[118] light-induced,[119] and humidity-based processes.[120] To study the stability of the doped HTAZ and FTAZ, films were spun-cast and doped with 50 mM $FeCl_3$ for 20 s, and the UV-Vis spectra were monitored over time (**Figure 3.3a & b**). The films were kept in air and in the dark for the duration of the experiments.

The dedoping behaviors of the two polymers are nearly identical and so they will be discussed together. The free-charge-carrier peak at 790 nm increases in intensity from 0 min – 120 min, but at times > 120 min peak integration decreases. Conversely,

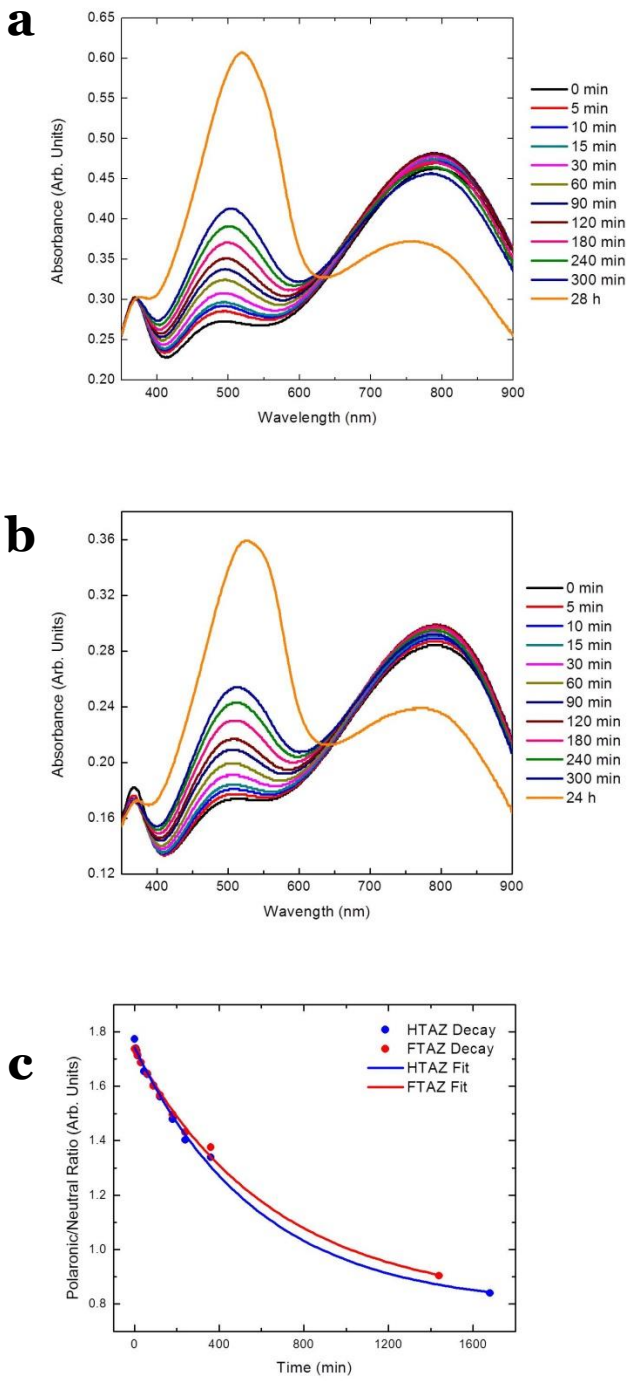


**Figure 3.3.** UV-Vis stability of doped HTAZ and FTAZ

*(a)* UV-Vis spectra of HTAZ taken at various times after $FeCl_3$ doping. *(b)* UV-Vis spectra of FTAZ taken at various times after $FeCl_3$ doping. *(c)* Integration ratios of the polaronic and neutral polymer absorption bands vs. time, fits are exponential decay. All samples are kept in air and in the dark between measurements.

the neutral polymer peak at 500 nm increases at every time interval. This behavior is likely explained by competing reductions. Because the doped polymers contain both polarons and bipolarons, reduction can occur either from bipolarons to polarons, or polarons to neutral polymer units. At times soon after doping, the bipolaron to polaron reduction outcompetes the polaron to neutral reduction, leading to an increase in the polaronic absorption peak at 790 nm. However, after a sufficient number of bipolarons have been reduced in the material, the polaron to neutral reduction occurs more quickly, leading to a decrease in the polaron peak integration. **Figure 3.3c** examines the HTAZ and FTAZ polaron:neutral peak ratios as a function of time after doping. Though the peak ratio decreases in a non-linear fashion, after 90 minutes the ratio is at approximately 90% of the original value. Thus, even though the films are unstable in air, accurate values of conductivity can be achieved through expediting the measurement process.

Curiously, when the stability of the doped polymers is measured in air and under nitrogen, they no longer behave alike. For HTAZ, a clear dependence on environment is observed, with exposure to air drastically increasing the dedoping rate. This is contrasted by FTAZ, where there is no difference in dedoping rate when comparing polymer exposed to air with polymer left under nitrogen. The most common reported mechanism for environmental degradation of doped polymer films involves water acting as a reducing agent.[119,120] The water will oxidize to $H3O^+$, while reducing bipolarons and polarons in the film. The hydronium ions then react with the iron-based counterions to produce several iron(II) species. It is possible that the lower-lying HOMO level in FTAZ vs. HTAZ can expedite this reduction pathway. Current studies are focused on

elucidating the dedoping mechanism in both polymers, in order to understand the energy differences between the two polymers and to improve the doped polymer stability.

### *3.2.3 Electrical Conductivity of HTAZ and FTAZ*

Once both polymers can be doped and the doping level can be reliably controlled, the electrical conductivity can be measured. In Chapter 2, the electrical conductivity of electropolymerized PEDOT films was measured using the van der Pauw technique. This technique was also used to measure the conductivity of the HTAZ and FTAZ films. Unfortunately reliable values were not obtained. These issues most likely arise from the lower conductivities of the TAZ-based polymers when compared with PEDOT. At low conductivities the bias generated between the voltage-sensing probes is very small, leading to erratic resistance values. To mitigate this difficulty, patterned gold contacts were fabricated onto glass slides, and the polymer films were cast onto these patterned substrates. The contacts are 4000 μm wide, and the spacing between them is 20 μm, 40 μm, 60 μm, 80 μm, and 100 μm. Four-point probe IV measurements were performed at each spacing distance, resistance is plotted as a function of this spacing, and the conductivity is extracted from the slope (**Figure 3.4a**). This method is advantageous for high-resistance samples because the spacing between contacts is microscopic, lowering the resistances.

In brief, electrical conductivity measurements are generally performed as follows: a polymer film is doped in an $FeCl_3$ solution of the desired concentration, and immediately following rinsing, the conductivity is measured with a probe station. A UV-Vis spectrum is taken directly after determining the conductivity, and the process is

**a**

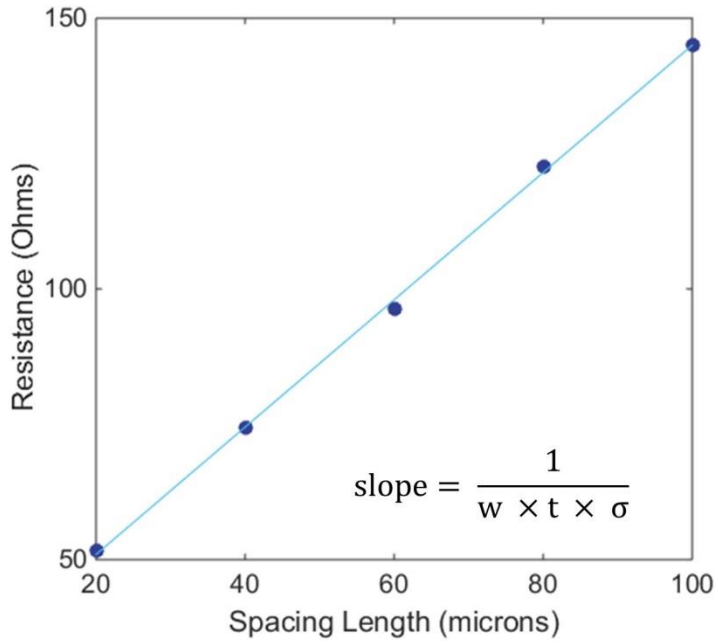


**b**

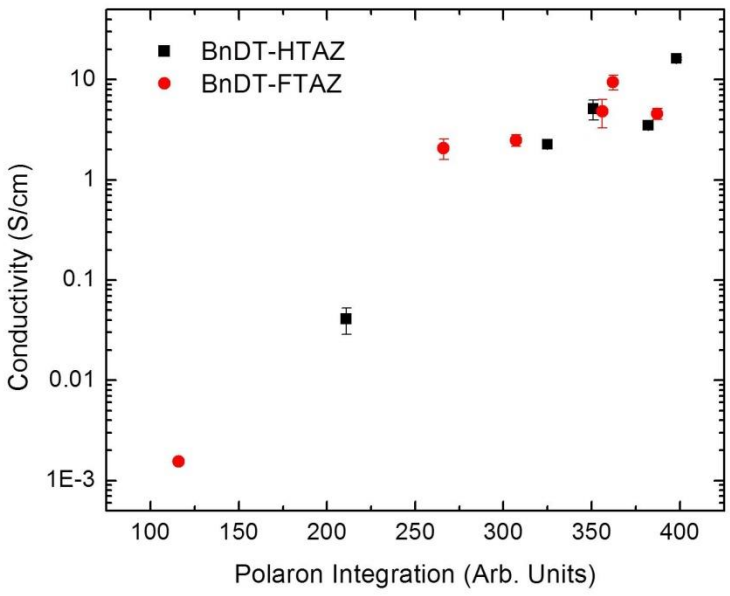


**Figure 3.4.** Electrical conductivity of HTAZ and FTAZ

*(a)* Representative electrical conductivity calculation of a HTAZ film, where w is contact width and t is thickness. *(b)* Electrical conductivities of HTAZ and FTAZ at varying charge carrier concentrations.

repeated for successive films. The samples are exposed to air for < 15 minutes from doping to UV-Vis measurements, meaning that any dedoping processes are generally negligible. To directly correlate charge carriers with conductivity, the measured conductivity values are plotted versus the normalized integrated free-carrier (polaronic) absorption peak (**Figure 3.4b**).

The electrical conductivities of HTAZ and FTAZ are very similar at comparable polaronic carrier densities. This is unexpected because as mentioned earlier the SCLC mobility of FTAZ is an order of magnitude larger than that of HTAZ, and the conductivity is directly dependent on the mobility per equation (5). The SCLC mobility calculations were performed in a vertical device configuration, where contact spacing was defined by film thickness. This is opposed to the conductivities measured here, which involve lateral transport through the films. Polymer mobilities are known to be anisotropic, and it is possible that though the mobilities in the two polymers are different in the vertical orientation, they are nearly equal when measured laterally. Fabricating OFET devices would allow for the direct determination of lateral mobility, and this work is ongoing.

Another potential reason for the observed conductivity behavior is the addition of the $FeCl_3$ dopant. It is clear that the dopant increases carrier concentration, but it is possible that it also changes the mobility of the films. Because FTAZ mobility is enhanced due to increased face-on stacking, and the doping process allows for the integration of $FeCl_4^-$ counterions into the polymer films, it is likely that these ions disturb this stacking in some way. Again, measuring OFET mobilities at varying dopant concentrations would help to clarify theses mechanisms.

## 3.3 Conclusions

A chemical doping method using ferric chloride was developed for two analogous polymers, HTAZ and FTAZ. The doping levels in both polymers were monitored via UV-Vis spectroscopy, and the degree of doping was controlled by varying the concentration of the dopant in solution. The stability of the doped films was measured and found to be very similar in air for both polymers. However, HTAZ was significantly more stable when stored under nitrogen, while the stability of FTAZ did not improve in the inert environment. The electrical conductivities were measured as a function of free carrier concentration, and a highest measured value of 16.1 S/cm was achieved for doped HTAZ. Unexpectedly, the conductivity was not enhanced in the FTAZ films, despite its higher SCLC mobility. Two possible reasons for the lack of conductivity enhancement are an anisotropic mobility in the lateral direction when compared with the vertical direction in these polymers, or a disruption of inter-chain packing and morphology by the dopant molecules. Current work is focused on increasing doped polymer stability, and on the direct measurement of mobility in doped polymer OFET devices. Determining the Seebeck effects of the HTAZ and FTAZ are also of future interest.

## 3.4 Experimental

### *3.4.1 General Methods*

All chemicals are used without further purification unless otherwise noted. Metal evaporations are conducted in an integrated glovebox system under an inert environment (MB-Evap, *MBraun*). AFM measurements are made using an Asylum AFM (MFP-3D, *Asylum Research*), and data processing is done in IGOR (*Wavemetrics*). Electrical measurements are taken on a micro-manipulated probe station (1160 Series,

*Signatone*) integrated with a Keithley 2636B Sourcemeter. UV-Vis spectra are taken on a Shimadzu instrument (UV-2600, *Shimadzu Corporation*). Sample thickness is determined via profilometry (D100, *KLA Tencor*).

### *3.4.2 HTAZ and FTAZ Film Formation*

HTAZ and FTAZ were synthesized as previously reported.[114] Solutions of either polymer were prepared at a 10 mg/mL concentration in trichlorobenzene (>99% anhydrous, *Sigma-Aldrich*), and the polymer solutions were allowed to stir at 130 °C for 6 hr inside a glovebox. Glass substrates were cleaned via 20 minute sonication steps in deionized water, acetone (*Fisher Scientific)*, and isopropyl alcohol (*Fisher Scientific*). The polymer solutions were spun-cast onto the glass substrates at 500 RPM for 60 s through a 1.0 μm PTFE filter (*Whatman PLC*). They were then vacuum annealed for 30 minutes at 1 mbar.

### *3.4.3 Preparation of HTAZ and FTAZ Patterned Substrates*

Glass slides were submerged in a solution of deionized water, ammonium hydroxide (14.8 M, *Fisher Scientific*), and hydrogen peroxide (30%, *Fisher Scientific*) in a 2:1:1 ratio for 20 minutes. The wafers were removed from the solution, copiously rinsed with deionized water and ethanol (100%, *Decon Laboratories Inc.*), and dried under a jet of nitrogen. The wafers underwent further cleaning in a UV ozone cleaner (Model 42A, *Jelight Company Inc.*) for 20 minutes. After cleaning, neat hexamethyldisilazane (Electronic Grade, *Alfa Aesar*) was applied to the surface of the $SiO_2$ substrates and dried under a jet of nitrogen. In a yellow-light cleanroom, photoresist (*JSR NFR 016 D2*) was spun-cast onto the cleaned $SiO_2$ substrates at 500 RPM for 5s, then 4000 RPM for 40 s. The coated substrates were pre-baked on a hot

plate at 95 ˚C for 90 s. A photomask (*Photoplot Store*) with the desired pattern was aligned over the substrate in a mask aligner (MA6/BA6, *Karl Suss*), and exposed under 365 nm i-line radiation for 10 s. The substrate underwent a post-exposure bake at 95 °C for 90 s, and was then submerged in a developing solution (MF-319, *Microposit*) for 60 s until features were fully formed, followed by thorough rinsing in deionized water, and drying with nitrogen. The patterned substrates were mounted and placed into an evaporation system, an adhesion layer of 5 nm of titanium was evaporated at 1 Å/s, and 40 nm of gold was evaporated at 1 Å/s for the first 3 nm, followed by a rate increase to 10 Å/s for the remaining thickness. The photoresist was lifted off with sonication in acetone. Films were spun-cast onto these patterned substrates as described in 3.4.2.

### *3.4.4 Iron(III) Chloride Doping Process*

To six separate scintillation vials, 0.041 g (0.25 mmol), 0.081 g (0.50 mmol), 0.162 g (1.00 mmol), 0.243 g (1.50 mmol), 0.405 g (2.50 mmol), and 0.810 g (5.00 mmol) of anhydrous $FeCl_3$ (97% Reagent Grade, *Sigma-Aldrich*) was added. Each $FeCl_3$ vial was added to 50 mL of acetonitrile (Optima grade, *Fisher Scientific*) to obtain final solution concentrations of 5 mM, 10 mM, 20 mM, 30 mM, 50 mM, and 100 mM. These solutions were added into a staining dish, and a HTAZ or FTAZ film was submerged for 20 s. The film was removed from solution, rinsed with neat acetonitrile, and dried under a stream of nitrogen. Solutions were not reused and the staining dish was rinsed with several washes of acetonitrile between doping steps. Further analysis was performed immediately after doping occurs.

# *Chapter 4*
# DESIGN AND FABRICATION OF POLYMER BRUSH METAL-MOLECULE-METAL JUNCTIONS VIA A TRANSFER PRINTING APPROACH

## 4.1 Introduction to MMM Junction Fabrication and Transfer Printing

### *4.1.1 Background*

***Chapter 2*** and ***Chapter 3*** have together demonstrated efforts towards polymer thin-film thermoelectric materials. In both of these studies, many polymer chains are involved in the transport of electrons through the material. However, as mentioned in the introduction, there is a decrease in polymer mobility as the number of inter-chain hops increases, thus making it desirable to transport mainly through intra-chain mechanisms.[121,122] One way to realize this type of device would be to directly connect single polymer chains between two electrodes.[123,124] Our group has previously demonstrated the ability to grow thiophene-based conjugated polymer brushes from the conducting oxide ITO.[125] Though these are well packed and oriented, issues with fabricating electrical top contacts on top of molecular layers have been previously discussed, and remain a problem in these polymer brush systems. The goal here is to develop a method to fabricate permanent top contacts onto these polymer brush systems, thus allowing them to be electrically and thermoelectrically characterized. This will be accomplished using transfer printing, as detailed below.

*4.1.2 Introduction to Transfer Printing*

Transfer printing is a soft-lithographic technique that works by "inking" an elastomeric stamp with a material, then placing the inked stamp onto a receiving substrate. When the stamp is removed, the ink adheres to the receiving substrate, providing that the receiving substrate has a higher affinity for the ink than the stamp. Transfer printing has previously been used to fabricate MMM junctions by inking a patterned stamp composed of PDMS or another elastomer with a metal, and placing the metal onto a SAM (**Figure 4.1**).[126,127] This is known as nanotransfer printing (nTP). Here, if the SAM end group and the metal are compatible (such as an S-Au linkage), the metal will transfer and form a MMM junction. By patterning the stamp itself, the dimensions of the pattern are limited by the physical properties of the stamp, and in fact, PDMS will collapse onto itself if it is patterned into high-aspect ratios or particularly small features.[128,129] Our group has developed a form of nTP where a PFPE stamp is used rather than PDMS.[83,84] The higher modulus of PFPE allows for sub-micron patterns to be transferred, and we have been able to electrically characterize aliphatic and aromatic SAMs using this method. However, nTP was unsuccessful at forming junctions onto polymer brushes.

Another method to form transfer printed MMM junctions is to pattern the top metal contact via lithography, and to use this metal pattern to ink an un-patterned stamp. The inked stamp is brought into contact with the SAM and removed, forming the junction. The adhesion between the metal ink, elastomeric stamp, and receiving SAM is controlled by changing the rate at which the stamp is removed from a given surface. This kinetically-controlled transfer printing (KTP) was developed by Prof. John

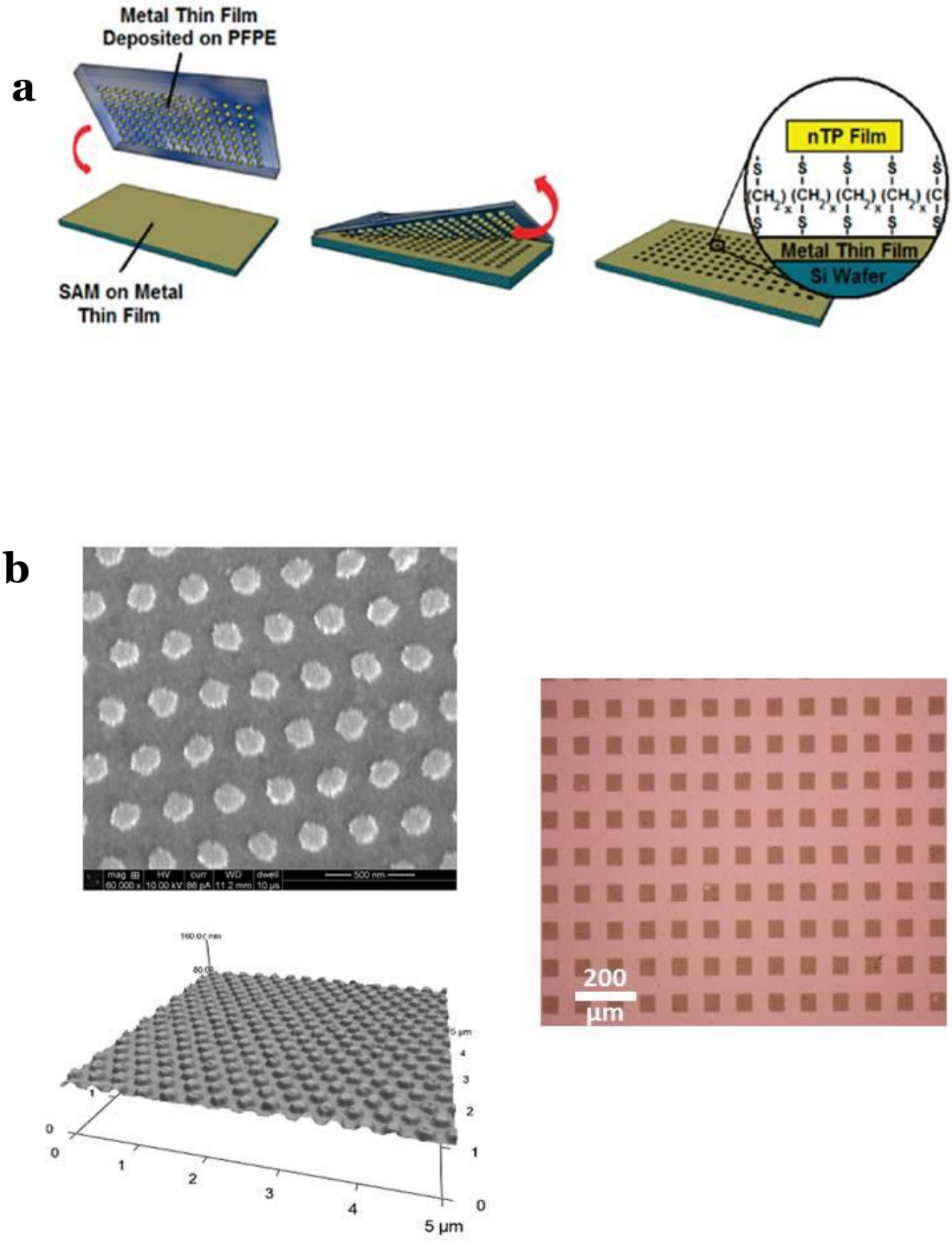


**Figure 4.1.** Forming MMM junctions via nTP.

*(a)* Diagrammatic depiction of nTP onto a SAM. *(b)* SEM, AFM, and optical micrographs of metal features patterned via nTP on top of decanedithiol SAMs.

Rodgers,[130–132] and it is advantageous versus other types of transfer printing because the pattern is no longer limited by the stamp and can be transferred onto relatively arbitrary substrates through control of the peel velocity of the stamp.

In this chapter metal-molecule-metal junctions based on polymer brushes will be fabricated via KTP, and these KTP top contacts will be compared with those formed via nTP. These junctions will be characterized, and their possible usefulness as thermoelectric materials will be discussed.

## 4.2 Results and Discussion

### *4.2.1 Theory of KTP*

Kinetically-controlled transfer printing relies on the viscoelastic properties of the PDMS stamp to aid in transferring the ink onto the receiving substrate. There are three interfaces of concern here: ink/substrate1, PDMS/ink, and ink/substrate2. The pickup and printing processes can be modeled as competing fracture paths between these three interfaces.

In fracture mechanics, there exists a critical energy release rate, $G_c$, such that when the energy release rate for crack propagation, G, reaches $G_c$, a crack is able to move steadily though the material. The critical energies for the ink/substrate1 and ink/substrate2 interfaces are represented as $G_c^{\text{ink/substrate1}}$ and $G_c^{\text{ink/substrate2}}$. Because the ink and both substrates are elastic materials, their interfacial $G_c$ values are independent of peel rate. However, the critical energy release rate of the PDMS/ink interface, $G_c^{\text{PDMS/ink}}$, varies with peel rate due to the viscoelastic nature of the stamp.

$$G_c^{PDMS/ink} = G_c^{PDMS/ink}(v) \tag{10}$$

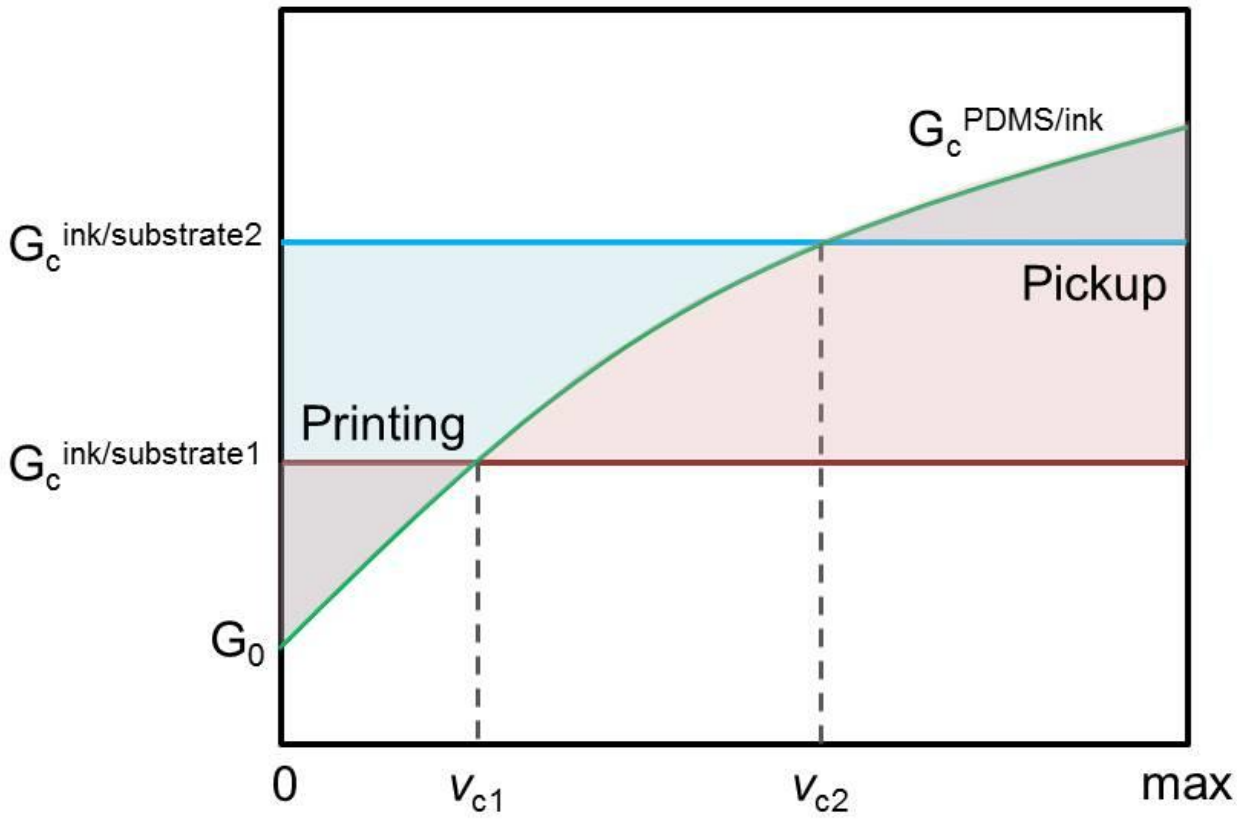


**Figure 4.2.** Interactions between interfaces in KTP.

In fact, $G_c^{PDMS/ink}$ increases with an increasing peel rate as given in (7), where $G_o$ is the

$$G_c^{PDMS/ink}(v) = G_0\left[1 + \left(\frac{v}{v_0}\right)^n\right] \tag{11}$$

critical energy release rate as $v$ approaches zero, $v_o$ is a reference peeling velocity that relates to $G_o$, and n is a scaling parameter that can be found experimentally. Equation (7) holds because the energy dissipation due to chain relaxation in the stamp increases as velocity increases. The necessary energies for pickup and printing are:

$$G_c^{ink/substrate1} < G_c^{PDMS/ink}(v) \quad \text{pickup} \tag{12}$$

$$G_c^{ink/substrate2} > G_c^{PDMS/ink}(v) \quad \text{printing} \tag{13}$$

In compatible materials, there is a critical peel velocity, $v_{c1,}$ at which $G_c^{PDMS/ink}(v_{c1}) = G_c^{ink/substrate1}$. Likewise, there is a $v_{c2}$ at which $G_c^{PDMS/ink}(v_{c2}) = G_c^{ink/substrate2}$. Above these $v_c$ values, the ink is picked up from the substrates by the PDMS, and below these $v_c$ values, the ink is left behind on the substrates. These interactions are depicted in **Figure 4.2**.

*4.2.2 General Procedure for the Formation of MMM Junctions via KTP*

The KTP process can be subdivided into 3 parts: fabricating the donor substrate (**Figure 4.3**), inking the stamp from donor substrate, and transferring the features to the receiving substrate (**Figure 4.4**). Donor substrates are prepared using standard photolithography procedures. Briefly, a silicon oxide substrate is coated with a photoresist and cured through a photomask under UV light. The photoresist is developed leaving a pattern on the silicon oxide, and a metal is sputter deposited through the pattern. The resist can be washed away, leaving a patterned metal layer on

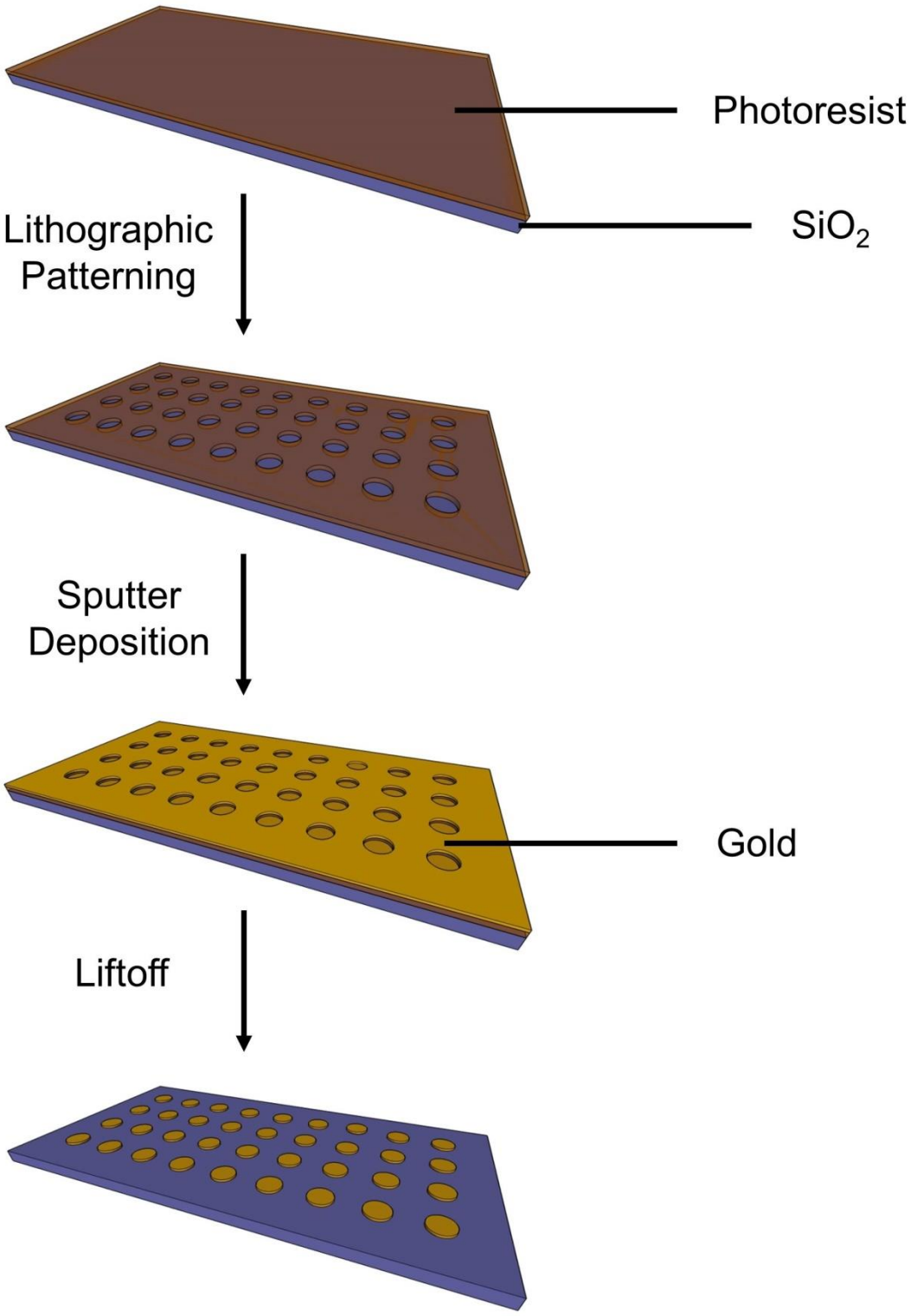


**Figure 4.3.** KTP Donor Fabrication.

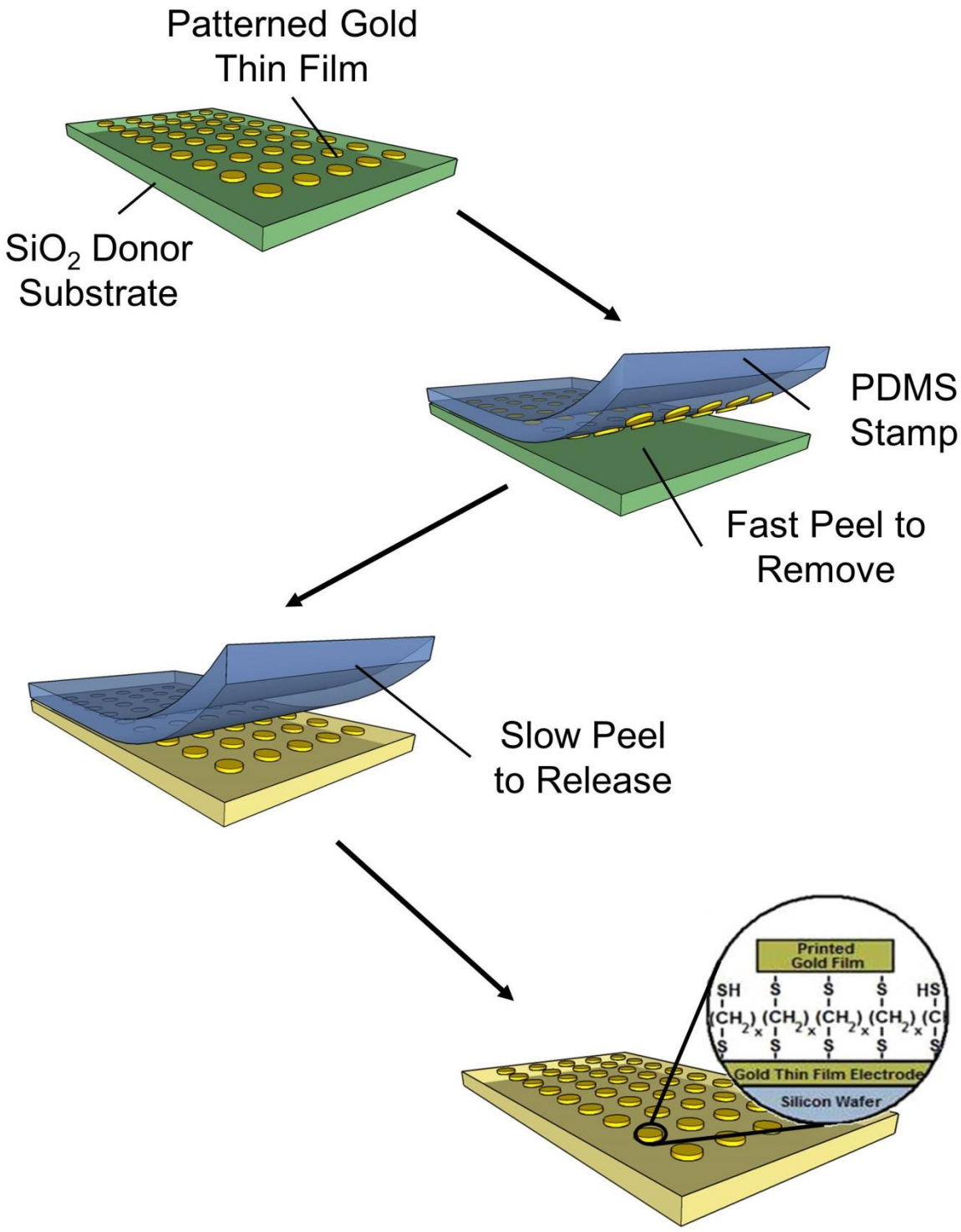


**Figure 4.4.** MMM Junctions fabricated via KTP.

top of the silicon oxide. To ink, a PDMS stamp is brought into contact with the patterned donor, and removed quickly (> 10 cm/s) from the surface. Once the stamp is inked, it is brought into contact with the receiving substrate and removed slowly (< 0.1 cm/s), leaving the metal pattern on top of the receiver.

*4.2.3 Fabrication of Donor Substrates*

Donor substrate fabrication is a standard lithography and liftoff process with a few exceptions. Due to the necessary weak binding between the donor substrate and the deposited ink that is needed for KTP, most photoresist liftoff conditions were incompatible, removing the patterned metal layer as well as the resist. This included sonication for any longer than several seconds. To solve this, a negative photoresist was used and developed for 150% of the recommended time. This resulted in an undercut of the resist which allowed liftoff via a 15 minute pre-soak in solvent followed by < 5 seconds of sonication. SEM images of gold donors after lithography and liftoff are displayed in **Figure 4.5a & b.**

Once the donor lithography and liftoff process was optimized several attempts were made to pick up the gold pattern from the substrate, but all attempts failed to yield reliable pickup. It was hypothesized that the binding interaction between the gold and the silicon oxide was too strong, so that even at maximum peel velocity the $v_c$ for pickup was not reached. To weaken this interaction, an etching step was added following liftoff. The donors were placed in a dilute hydrofluoric acid (HF) solution, which selectively etches $SiO_2$ (14).

$$SiO_2 + 6\,HF \rightarrow H_2SiF_6 + 2\,H_2O \qquad (14)$$

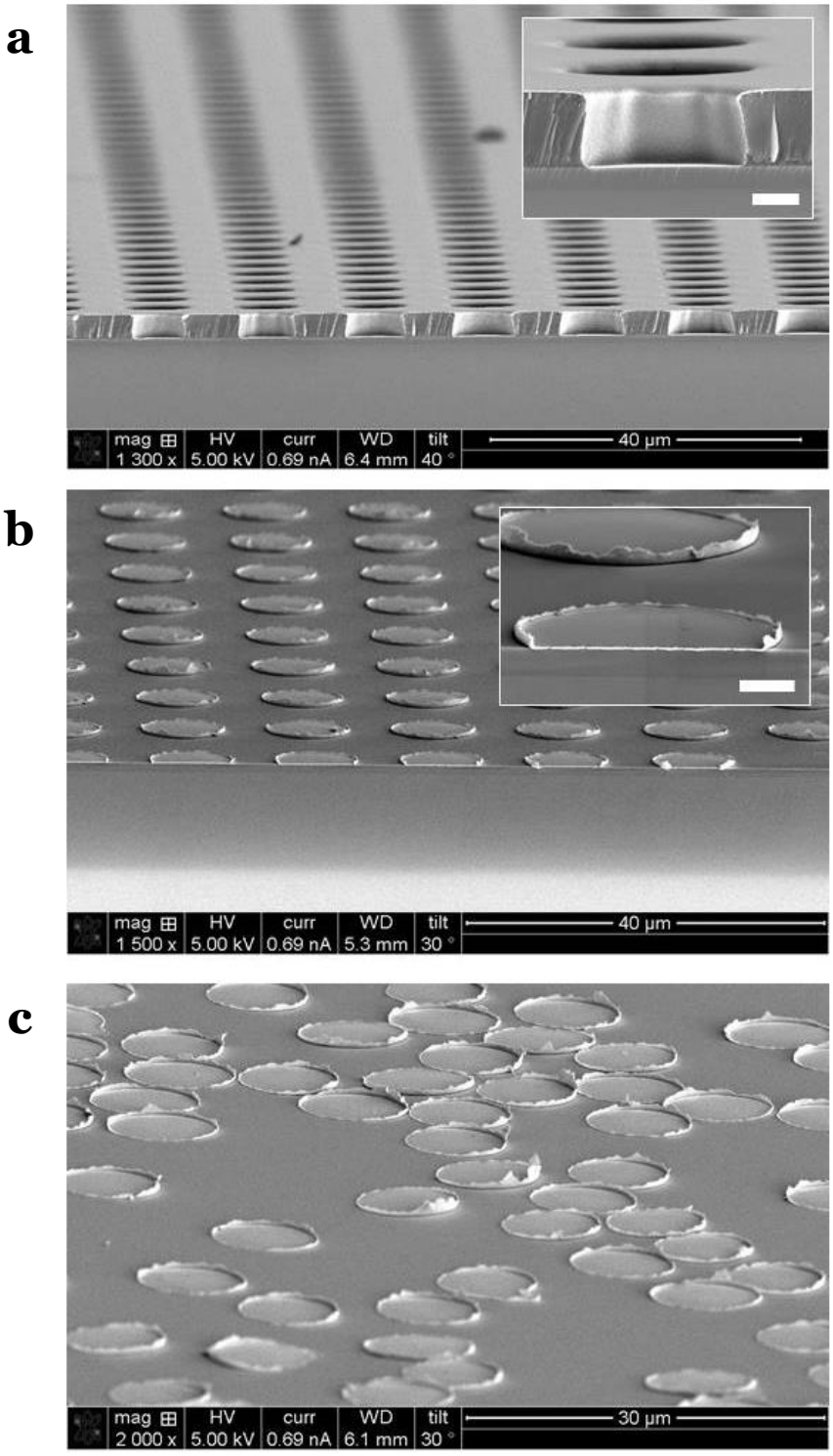


**Figure 4.5.** SEM micrographs of KTP donors.

*(a)* 7 µm diameter gold features deposited on top of patterned photoresist and $SiO_2$. *(b)* 7 µm diameter features on $SiO_2$ after liftoff of the photoresist. *(c)* 7 µm features after over-etching with HF. Inset scale bars are 2 µm.

The etching time needed depends on the concentration of HF, the size and shape of the metal features, and the thickness of the $SiO_2$ layer. If features are excessively etched, they will delaminate from the $SiO_2$ surface (**Figure 4.5c**). Once appropriate etching conditions are found, the gold features can then be removed effectively from the substrate with PDMS.

*4.2.4 Pickup and Placement of Patterns*

As mentioned in the previous section, once donor substrates are fabricated and the $SiO_2$ layer is etched with HF, pickup of features onto PDMS proceeds quite well. The PDMS stamps used are approximately 1 cm thick so that they can remain rigid during pickup and printing. To pick up the metal ink, PDMS is brought into contact with the donor and rapidly peeled away at a velocity > 10 cm/s, which transfers the pattern from the donor to the stamp. In general, small features (< 100 μm) transfer easier onto the PDMS, while features that are macroscopic in one or both directions are more difficult to pick up. This is presumably because the van der Waals' interactions' are stronger between the metal and the substrate when the area is larger, thus making pickup more difficult. Also, it is problematic to HF etch on larger features because of the amount of $SiO_2$ that must be dissolved.

Once the pattern has been transferred to the PDMS, it is printed by bringing the stamp into contact with the receiving substrate. The stamp is left for several minutes to allow intimate contact between the metal ink and the substrate, and then slowly peeled at < 0.1 cm/s. During this removal the metal ink is transferred to the receiving substrate. We have been able to obtain near-quantitative transfer of gold metal films onto substrates with a strong binding affinity for gold such as thiol-based SAMs (Error!

Reference source not found.**a**), as well as those with a weaker binding affinity such as $SiO_2$ (Error! Reference source not found.**b**). The transfer is applicable to many shapes and sizes of microscale features, including the 7 μm diameter circles in (Error! Reference source not found.**c**). However, when feature size is increased above the microscale, the printing process becomes quite difficult. Because the features are transferred gradually rather than all at once, these larger patterns will flex and ultimately fracture as they are printed onto a receiving substrate (Error! Reference source not found.**d**). In the polymer brush system of interest, features transfer readily onto polymer films that are < 15 nm in length, but those > 15 nm prove more difficult. This is believed to be because of the lower surface energy of longer brushes, most likely due to surface roughness. Sporadic transfer will occur with careful peel back of the PDMS stamp, and in fact brushes as thick as 25 nm have been characterized.

### *4.2.5 Comparison of KTP Top Contacts with Those Formed Via nTP*

When forming MMM junctions via transfer printing, KTP presents advantages over nTP in terms of feature continuity and surface roughness. When a metal thin film is directly deposited onto either PDMS or PFPE, as it is during an nTP process, the film will crack during formation (**Figure 4.6a**).[133] This happens because the stamp materials have low surface energies, and therefore interact weakly with the deposited gold. Also, because films above 20 nm thick do not lead to high quality transfer via nTP, depositing thicker films is not a viable strategy to eliminate cracks. An attempt to minimize this cracking of nTP features was made by pre-treating the stamp with oxygen plasma, thus functionalizing the surface to increase gold interactions.[134] This helped to lower the number and width of individual surface cracks, but did not remove them

completely **(Figure 4.6b**). Because it is impossible to perform an nTP process without this deposition step, it is not possible at this point to have a top contact formed via nTP that is crack-free. On the other hand, KTP features can be deposited onto any surface and then picked up via a PDMS stamp. Thin films of many metals are routinely deposited onto silicon oxide without cracking, making this method ideal for the production of crack-free top contacts as long as cracks are not introduced during transfer. Additionally, excellent transfer can occur even with films several hundred nm thick, and these thicker films are less prone to the development of cracks. Though some large cracks could be observed upon transfer for macroscopic-sized features, no evidence of cracking was perceived on feature sizes below 100 μm when characterized via SEM (**Figure 4.6c**).

Another major issue with metal contacts transferred via nTP is the roughness of the metal/receiving substrate interface in the final junction. In nTP, the metal is transferred directly to the substrate after being deposited, which means that the roughness at the top contact will depend on the final roughness of this deposited film. Traditionally these films are ~ 1 nm root-mean-square (RMS) roughness, although we have decreased their roughness to < 600 pm RMS by increasing the rate of deposition. The final junctions made via this transfer-printing method contain molecules that are as short as 1 nm, meaning that any further decrease would be extremely beneficial towards consistent electrical properties in finished devices. In the KTP case, the metal film to be transferred is picked up by the stamp and subsequently printed onto the substrate. Thus, the roughness at the top contact interface will depend on the roughness at the donor/metal interface when the donor is fabricated. Seemingly, the metal pattern

replicates the roughness of the donor substrate onto which it is originally deposited. In

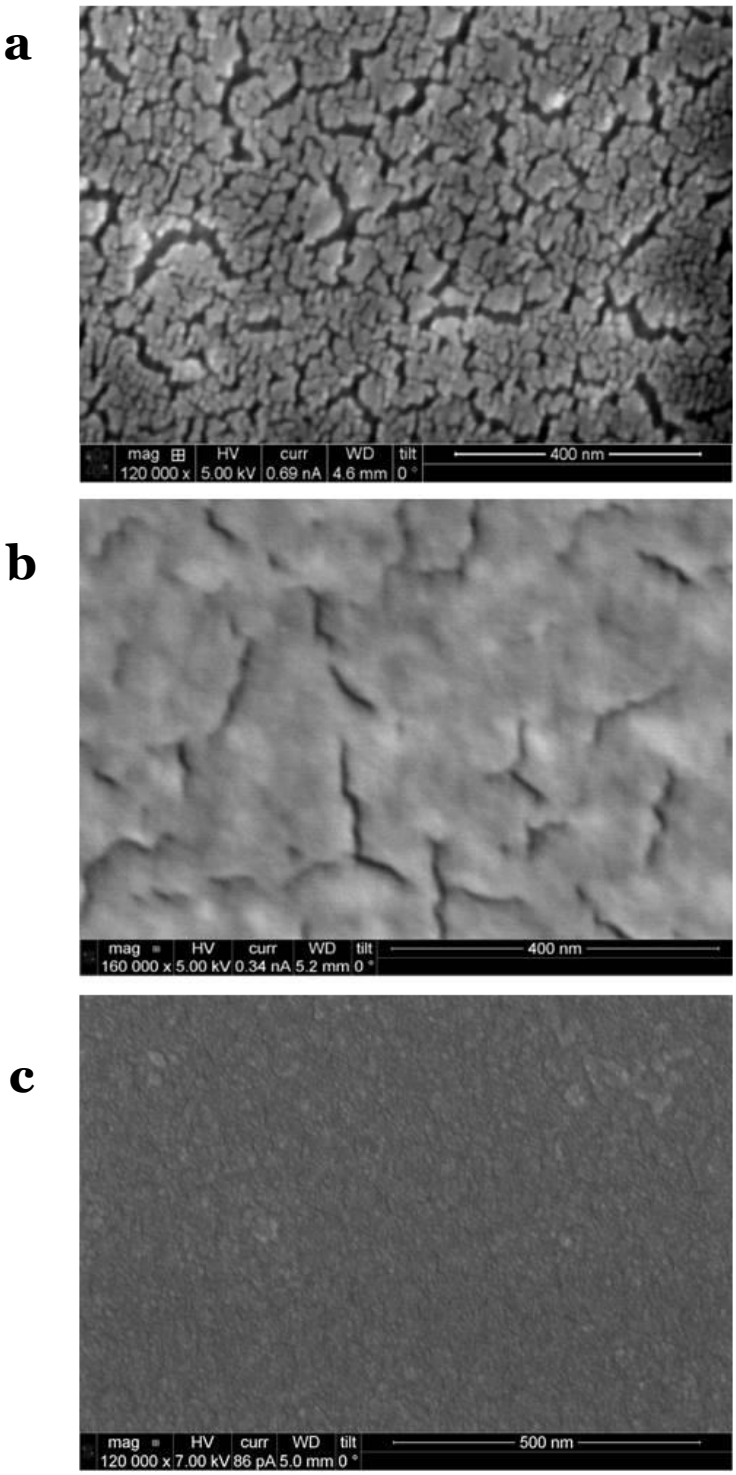


**Figure 4.6.** Cracking in nTP and KTP features

*(a)* Cracking in a 50 μm feature transferred via nTP with a PDMS stamp. *(b)* Cracking in a 50 μm feature transferred via nTP with a PDMS stamp that had been treated with oxygen plasma. *(c)* 50 μm feature transferred with via KTP with a PDMS stamp showing no evidence of cracking.

our case, the silicon oxide that is used as the donor substrate has an RMS roughness of < 300 pm, twice as smooth as in the nTP case. Conceivably, with an atomically smooth substrate, such as mica, even lower roughness could be achieved.

### *4.2.6 Fabrication of Polymer-Brush Based MMM Junctions via KTP*

Our group has been able to grow and characterize poly(3-methylthiophene) (P3MT) brushes from a conductive ITO surface via surface initiated Kumada-catalyst transfer polycondensation (SI-KCTP) (**Figure 4.7**).[125] ITO slides are cleaned and a monolayer is formed in solution onto the surface of the ITO. The monolayer is thermally annealed to increase ordering, and a Pd catalyst is inserted. This monomer-catalyst species remains surface-bound to the ITO, and serves as a polymerization initiator. The functionalized ITO is placed into a solution of active monomer to propagate the polymer chain, and chain length can be controlled via reaction time. The results of these reactions are vertically-oriented conjugated polymer chains that are surface-bound to ITO.

To electrically characterize these P3MT brushes top contacts are transferred onto the films via KTP. Measurements are taken using a cAFM technique, placing a gold-coated AFM tip in contact with the KTP junctions, electrically connecting the ITO and the tip, and applying a bias to the tip to force a current through the polymer brush. MMM junctions with 50 × 50 μm square top contacts, and 7 μm diameter circle top contacts have both been measured using this method. In the 50 μm square case, measuring individual junctions is a slow and tedious process because of the limitations of the AFM. Specifically, the maximum scanning range can fit only a few junctions, so in order to characterize many junctions, multiple scans must be performed. This is also

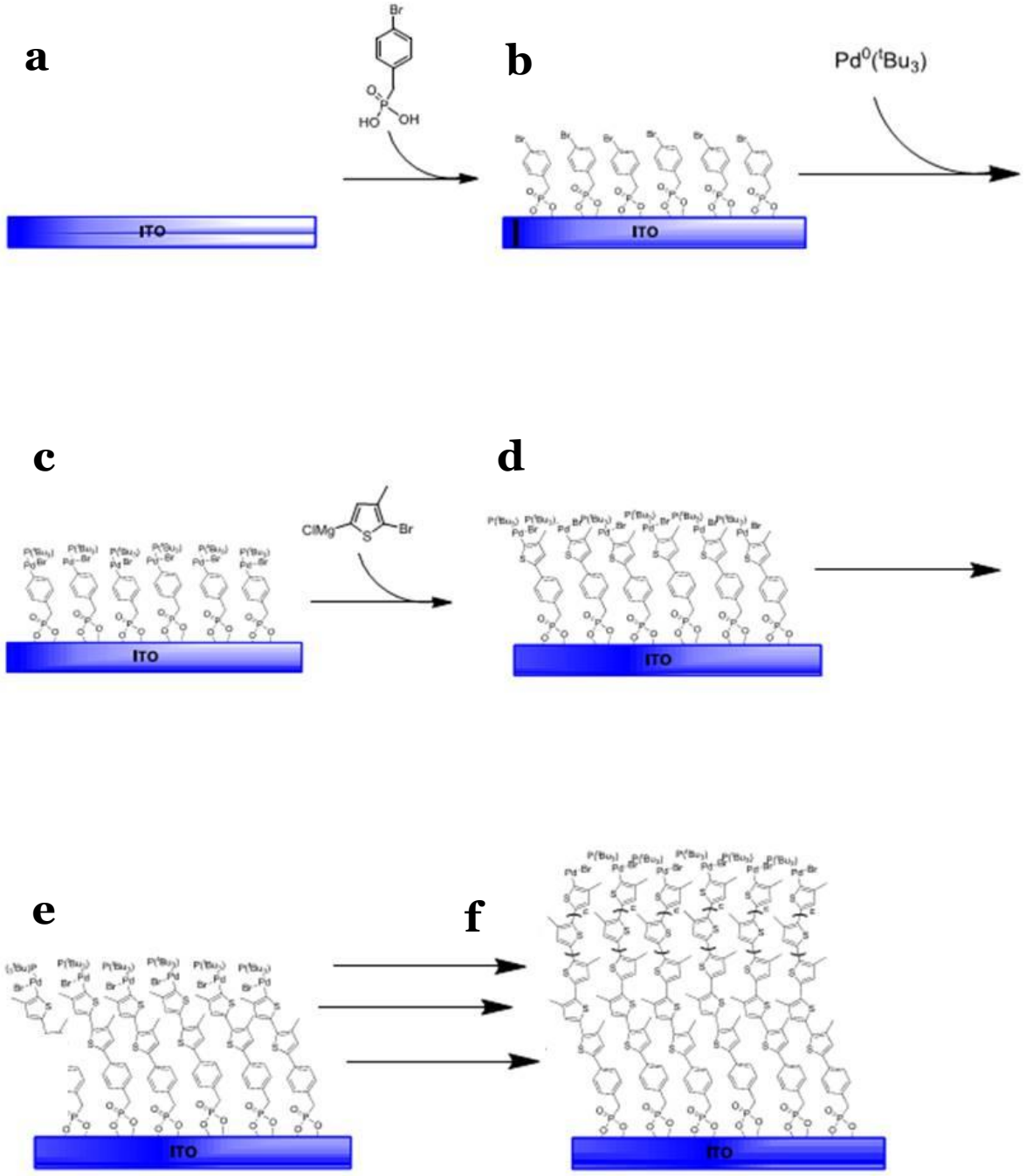


**Figure 4.7.** SI-KCTP formation of P3MT brushes

*(a)* Cleaned ITO surface. *(b)* Monolayer formation onto the ITO surface. *(c)* Catalyst insertion to form the initiating species. *(d)* Attachment of the first monomer onto the surface. *(e), (f)* continued chain extension onto the surface to form the final P3MT film.

disadvantageous because the gold-coated tip will wear down with increased scanning, lowering the reliability of these measurements. Despite these shortcomings, approximately 94% of 50 μm devices gave measureable IV curves, and thus were considered working. The other 6% were shorted. Shorting most likely occurred due to wrinkling or other deformations in the metal top contacts that created pinholes in the polymer film, allowing a direct gold-ITO current pathway.

The 7 μm circle features improve upon the 50 μm squares because the area footprint of a 7 μm circle is ~2% of the larger square features. This eliminates many of the problems related to the speed at which data can be collected, and also helps to measure many more junctions with an individual cAFM tip. The decreased junction size also leads to a decrease in shorted junctions to 2%. Of the remaining junctions, 90% are working and 8% are open. Open devices are not seen in the 50 μm squares, and the reason is presumed to be poor contact between the P3MT and the top gold electrode. Because the 7 μm features are smaller and more rigid, they will sometimes not conform to the polymer morphology which leads to an open circuit. Even with these open junctions, it was decided that the smaller circle features were superior to the larger square features, and the remaining electrical characterization was done on these 7 μm diameter circles.

### *4.2.7 Electrical Characterization of As-Grown P3MT MMM Junctions*

Once top contacts could be fabricated via KTP, electrical characterizations were performed in order to elucidate the electrical properties of the KTP P3MT junctions. Typically an IV curve was acquired on an individual P3MT KTP junction by sweeping a bias between -3 V and +3 V. This was performed on several different KTP top contacts,

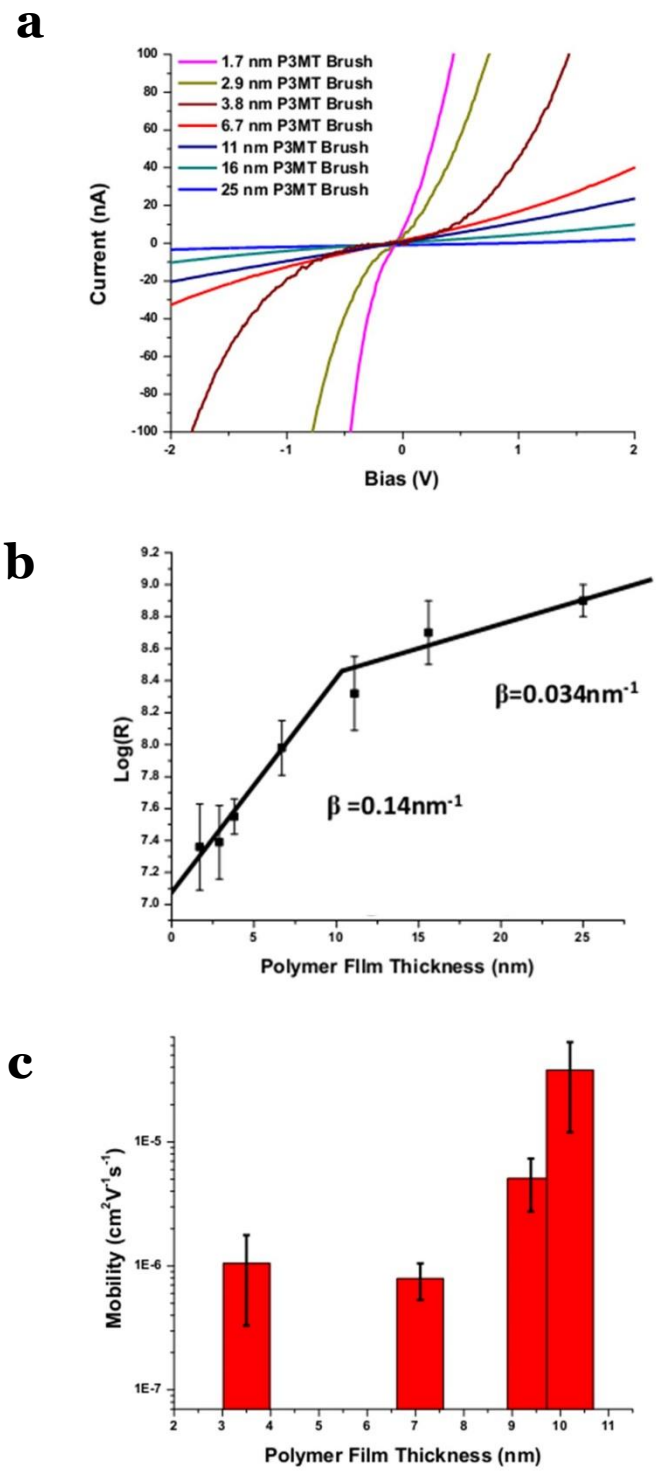


**Figure 4.8.** Charge transport in as-grown KTP P3MT junctions

*(a)* Representative IV curves of several lengths of P3MT KTP junctions. *(b)* Length dependence of resistance in P3MT KTP junctions. *(c)* Mobility of P3MT KTP junctions.

and the results were averaged to obtain the final data. The quantities of interest here are the resistance and the mobility of the KTP P3MT devices.

Representative IV curves of KTP P3MT devices containing several different chain lengths are given in **Figure 4.8a**. These curves are non-ohmic, meaning that the current does not depend linearly on the applied voltage as given by Ohm's law. This is expected for a molecular electronic junction, since transport occurs either via tunneling or nearest-neighbor hopping mechanisms. If the IV curve is modeled using a cubic fit, the linear term of the fit is equal to the inverse of the resistance. It can be clearly seen in **Figure 4.8a**that as the length of the P3MT chains increase, resistance also increases. This dependence of resistance on length in molecular junctions can be described by the beta parameter, β. Equation (15) gives a modified version of the Simmons model,[135] which describes electron tunneling through a thin insulating film.

$$R = R_0 e^{\beta l} \tag{15}$$

Here $R_0$ is the resistance when molecule length = 0, and l is length. A lower value of β means less dependence of the resistance on molecule length, and thus more efficient charge transport. β can be near 10 $nm^{-1}$ for alkane-type molecules, and below 0.1 $nm^{-1}$ for heavily conjugated molecules.[68,69,136,137]

By plotting the log(Resistance) of the KTP P3MT junctions vs. the thickness of the polymer films, β can be extracted from the slope (**Figure 4.8b**). In these polymer systems there are two clear regimes with different β values, 0 – 10 nm and > 10 nm. The β values in both cases are among the lowest reported for molecular systems, indicating that this system is highly conjugated, and that charge transports very efficiently through

these KTP brushes. The transition to a lower β value is either due to a transition from tunneling to charge-hopping, or a change in the number of hops needed to cross the junction. This type of efficient transport will hopefully mean that high conductivities can be obtained via doping these P3MT films.

Mobility (μ) is also of great interest as explained in Chapter 1. In polymer thin-films, the mobility can be determined via the Mott-Gurney Law (16).

$$J = \frac{9\varepsilon\mu V_a^2}{8L^3} \tag{16}$$

Here J is current density, ε is the dielectric constant of the film, $V_a$ is the applied bias, and L is the film thickness. The Mott-Gurney law is true only when charge transport exists in the space-charge limited current (SCLC) regime, and this regime occurs when the slope of the log-log IV plot is equal to two.[138,139] Thus, by taking the portion of an IV curve where its log-log slope equals two, and plotting the current density vs. the square root of the applied bias, mobility can be extracted from the slope. The mobilities of KTP P3MT junctions with varying polymer length are shown in **Figure 4.8c**, and these values are similar to other P3MT thin-films.

### *4.2.8 Electrical Characterization of Annealed P3MT Junctions*

It was discovered by our group that the P3MT brushes could be thermally annealed to improve their morphology. This annealing process increases the length of the polymer films (**Table 4.1**), and also their surface orientation. This chain extension is less dramatic in films that are thicker pre-annealed. KTP P3MT junctions were fabricated onto these annealed films, and a similar set of experiments was conducted in order to determine their electrical properties.

**Table 4.1.** Comparison between pre-annealed and post-annealed P3MT films

| *P3MT Pre-annealed Thickness (nm)* | *P3MT Post-annealed Thickness (nm)* | *ΔThickness (nm)* | *Post-annealed : pre-annealed change* |
|---|---|---|---|
| 3.5 ± 0.9 | 13.7 ± 0.7 | 10.2 ± 1.1 | 3.9 ± 1.0 |
| 7.1 ± 0.5 | 22.1 ± 0.9 | 15.0 ± 1.0 | 3.1 ± 0.3 |
| 9.4 ± 0.05 | 21.3 ± 2.3 | 11.9 ± 2.3 | 2.3 ± 0.2 |
| 10.2 ± 0.5 | 17.5 ± 2.9 | 7.3 ± 2.9 | 1.7 ± 0.3 |

**Figure 4.9a** describes representative IV behavior of a series of annealed KTP P3MT junctions. Here, the resistance dependence on film thickness is equally apparent as in the pre-annealed junctions. A β value of 0.15 $nm^{-1}$ is calculated for these junctions using the same methods as the pre-annealed junctions. Interestingly, in the annealed junctions there is only one regime of charge transport. This is contrary to the pre-annealed junctions which exhibited a transition at > 10 nm to a lower β value. Based on the large ratio change in film thickness for thinner pre-annealed polymer films, it is likely that the lower β regime in the pre-annealed junctions is due to poor quality films. Once the films are annealed, film quality is equal for all polymer lengths.

Mobility measurements for annealed KTP P3MT junctions are conducted identically to pre-annealed films. At each film length measured, mobility increases in annealed films when compared with their corresponding pre-annealed film (**Figure 4.9b**). This increase is as high as two orders of magnitude in the shortest pre-annealed film, and the mobility values that are obtained approach those measured for oriented P3MT chains on a surface. The enhancement in mobility is likely explained by the chain extension during the annealing process. By extending individual chains, intra-chain

**a**

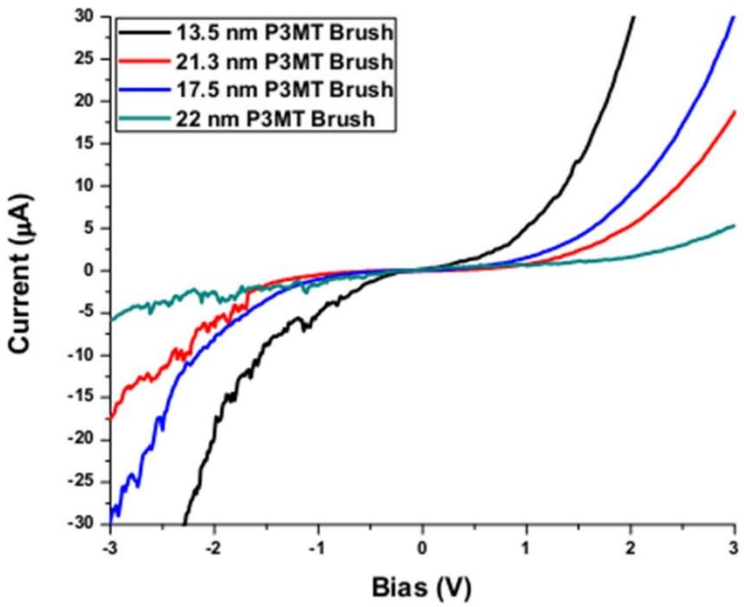


**b**

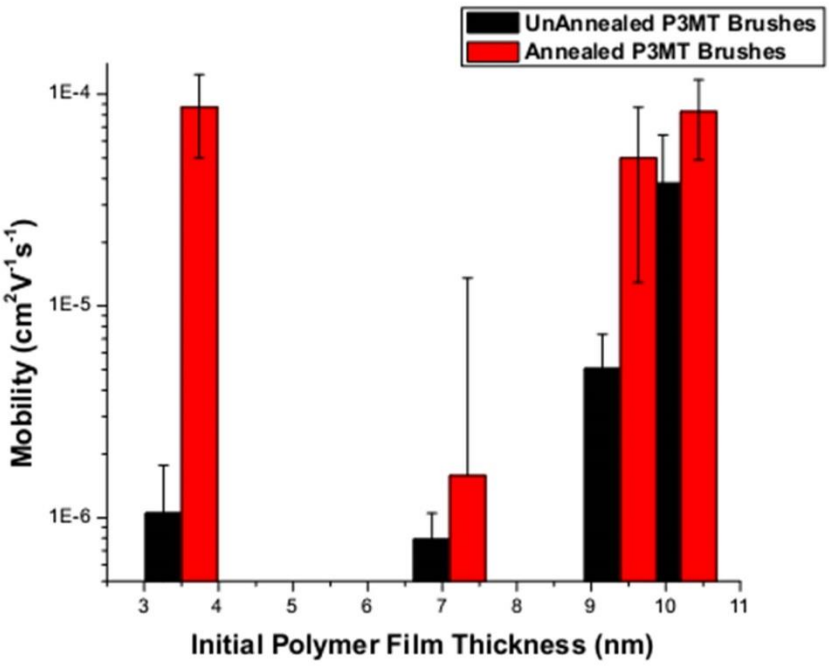


**Figure 4.9.** Charge transport in annealed KTP P3MT junctions.

*(a)* Representative IV curves of annealed KTP P3MT junctions of varying lengths. *(b)* Comparison of mobility in annealed and as grown KTP P3MT junctions.

conjugation lengths as well as inter-chain interactions are increased. These types of interactions allow charge to transport more quickly through the film, increasing the mobility. Though the values reported here are lower than some others, it is clearly demonstrated that the junctions formed via KTP allow for the characterization of IV behavior and mobility in these P3MT systems. By further tuning P3MT morphology through additional annealing steps or modified synthetic procedures, mobility can be further increased.

## 4.3 Conclusions

Metal-molecule-metal junctions were formed on a poly(3-methylthiophene) polymer brush via kinetically-controlled transfer printing. The KTP process depends on changing the surface energy of an elastomeric stamp by controlling the peel rate, and through this process patterns can be transferred from a silicon oxide donor substrate onto the P3MT receiving substrate. Comparisons were made between the KTP process and a previously developed nTP process, and it was shown that the KTP process significantly improves both the surface cracking and surface roughness of transfer-printed features. The KTP P3MT junctions were electrically characterized, and their resistance, β-value, and SCLC mobility were determined. It was discovered that mobility can be greatly enhanced by thermally annealing the P3MT brushes, and this high mobility will hopefully lead to large thermoelectric effects in the future.

## 4.4 Experimental

### *4.4.1 General Methods*

AFM measurements were made using an Asylum AFM (MFP-3D, *Asylum Research*), and data processing was done in IGOR (*Wavemetrics*). SEM images were

taken on an FEI instrument (Helios 600 Nanolab Dualbeam, *FEI*). Sputter coating was performed in a Kurt Lesker system (PVD 75, *Kurt Lesker*).

*4.4.2 KTP Donor Fabrication*

Silicon wafers with 1 μm thermally-grown silicon oxide (*University Wafer*) were submerged in a solution of deionized water, ammonium hydroxide (14.8 M, *Fisher Scientific*), and hydrogen peroxide (30%, *Fisher Scientific*) in a 2:1:1 ratio for 20 minutes. The wafers were removed from the solution, copiously rinsed with deionized water and ethanol (100%, *Decon Laboratories Inc.*), and dried under a jet of nitrogen. The wafers underwent further cleaning in a UV ozone cleaner (Model 42A, *Jelight Company Inc.*) for 20 minutes. After cleaning, neat hexamethyldisilazane (Electronic Grade, *Alfa Aesar*) was applied to the surface of the $SiO_2$ substrates and dried under a jet of nitrogen. In a yellow-light cleanroom, photoresist (*JSR NFR 016 D2*) was spun-cast onto the cleaned $SiO_2$ substrates at 500 RPM for 5s, then 4000 RPM for 40 s. The coated substrates were pre-baked on a hot plate at 95 °C for 90 s. A photomask (*Photoplot Store*) with the desired pattern was aligned over the substrate in a mask aligner (MA6/BA6, *Karl Suss*), and exposed under 365 nm i-line radiation for 10 s. The substrate underwent a post-exposure bake at 95 °C for 90 s, and was then submerged in a developing solution (MF-319, *Microposit*) for 60 s until features are fully formed, followed by thorough rinsing in deionized water, and drying with nitrogen. The patterned substrates were mounted and placed into a sputter-deposition system, and a 200 nm layer of gold was sputtered onto them at a constant rate of 2 Å/s. The substrates were removed and soaked in an acetone bath (*Fisher Scientific*) for 30 minutes, and if necessary agitated briefly in an ultrasonication bath in order to lift off the photoresist.

The substrates were then etched in hydrofluoric acid (5 %, *Fisher Scientific*), and the etching time depended on the size and shape of the feature. For 7 μm diameter circle features, the etching time was 5 s.

### *4.4.3 PDMS Stamp Preparation*

PDMS prepolymer (Sylgard 184 Elastomer Kit, *Dow Corning)* was mixed 3.5:1 (*w/w*) with the corresponding cross-linker and stirred until well combined. The mixture was poured into a plastic petri-dish until it was approximately 10 mm thick. The dish was placed into a 1 mbar vacuum for 1 hr until all bubbles were removed from the mixture. The dish was then placed into a 70 °C oven overnight until the PDMS is thermally-cured. The stamp was cut into pieces approximately 12 mm × 25 mm in size for the KTP process.

### *4.4.4 KTP Process*

A donor substrate was mounted onto a lab bench with double-sided tape, and a PDMS stamp was cleaned via scotch tape to remove any particulate from the surface of the stamp. The stamp was mounted onto a glass slide with double-sided tape, and placed face down onto the surface of the donor. Pressure was applied to the glass slide to bring the stamp into contact with the donor surface, and the stamp was “popped” off of the surface by tapping on one side of the glass slide. The rate of removal of the stamp from the donor substrate was then quite fast (> 10 cm/s), so the features from the donor are transferred onto the stamp. A polymer-brush substrate was mounted to the lab bench via double-sided tape, and the feature-containing stamp was brought into contact with this substrate after removal of the glass-slide backing. The stamp was lightly tapped to bring the gold features into contact with the polymer brush, and left for > 3

minutes to obtain intimate contact. The stamp was then very carefully peeled away from the surface. This was done as slow as possible, but practically occurred at a rate of ~ 0.5 mm/s. After removal of the stamp the polymer brush was examined under a microscope to confirm that adequate transfer had occurred.

### *4.4.5 cAFM Measurements*

Cantilevers (AC240TS, Force Constant ~ 2 N/m *Olympus*) were sputter-coated with alternating layers of chromium and gold at 2 Å/s in the following manner: 2.5 nm Cr, 5.0 nm Au, 2.5 nm Cr, 10.0 nm Au, 2.5 nm Cr, 35.0 nm Au, 2.5 nm Cr, 50.0 nm Au. The coated tips were mounted onto the AFM, and the circuit for conductive measurements was created by connecting a wire between the tip and the substrate. A tapping scan was first performed over the KTP features in order to determine their locations. To acquire an IV curve, the AFM was switched to contact mode, the tip was placed above a single KTP feature, and the set point was gradually increased until contact was made. A bias was applied to the tip and swept over the desired range, and the current was recorded.

# *Chapter 5*
# SUMMARY OF CONCLUSIONS AND RECOMMENDATIONS FOR FUTURE WORK

## 5.1 Summary of Conclusions

Due to a rapid rise in global population and a concurrent expansion in worldwide power usage, the proportion of energy that is derived from renewable sources must increase in the coming decades above its current 3.5%. Heat is a vast and untapped renewable resource, and if it can be captured and exploited, it could become a major part of the future world energy portfolio. Materials that can convert heat to electricity and vice versa are known as thermoelectric materials, and have been intensely researched over the previous two decades. However, despite these efforts current TE applications are scarce. This is because present commercial devices make use of inorganic semiconductors that are both expensive and toxic to the environment. Additionally, these devices are much lower in efficiency when compared with other energy technologies, and lab techniques that increase efficiency are extremely difficult to scale.

A possible way forward to commercial TE devices is to utilize conjugated organic polymers. These materials have been implemented into LEDs, photovoltaics, and electrochromic applications, among others. They are lightweight, flexible, synthetically tunable, and relatively non-toxic to the environment. Also, they are easily processed into devices, which helps overcome their generally lower performance when compared with inorganic materials. The past several years have seen rapid advancement in the organic

TE field, and the existing state of the art can achieve performance near 40% of commercial inorganic systems.[52]

Even with these advancements, much more work still needs to be done to improve organic thermoelectric devices. Alternative approaches must be explored to help discover novel high-performing polymer systems. Fundamental studies to explain polymer structure-property relationships also need be conducted so that future polymers can be designed in a logical way. Additionally, new device architectures and polymer orientations should be evaluated. This dissertation has sought to make contributions in these three areas.

### *5.1.1 Electropolymerized PEDOT Thin Films as an Organic TE Material*

Poly(3,4-ethylenedioxythiophene), especially when complexed with polystyrene sulfonate, is the most prevalent as well as the highest performing organic TE material. Because PEDOT:PSS is stable and commercially available as an aqueous dispersion, it is quite simple to fabricate thermoelectric devices using it, and several examples exist in the literature.[48–50,140] However, the polyanion chains in PEDOT:PSS films are electrically insulating and therefore detrimental to the TE performance. Some recent efforts have focused on either selectively removing the neutral PSS portion, or chemically polymerizing PEDOT with small molecule counterions.[55,57,91] A different approach could be to electropolymerize PEDOT directly onto a surface, eliminating any film-casting steps. The morphology of the film is affected by the polymerization conditions,[105] and the counterion can be controlled directly by altering the electrolyte, which has been shown to affect TE performance.[107]

A detailed study of electropolymerized PEDOT film morphology was conducted, and it was determined that both the polymerization rate and the final film thickness will alter morphology. Thicker films are generally more globular than the net-like morphology of thinner films, and film homogeneity is increased by decreasing the rate of polymerization. Once this dependence was understood, thin PEDOT films (< 150 nm) at rates near 1 nm/s were electropolymerized via several different methods onto gold working electrodes with a $Bmim^+$ $PF_6^-$ supporting electrolyte. Films polymerized under potentiostatic (constant voltage) and galvanostatic (constant current) conditions exhibited very similar morphologies, possessing a homogenous net-like structure with dense clusters existing at the surface. Alternatively, films polymerized under potentiodynamic conditions contained large networks of dense PEDOT, rather than simple clusters. Despite these morphology differences, the UV-Vis spectra of all three polymerization techniques were consistent with heavily-oxidized PEDOT films.

The electropolymerized PEDOT films were etched in aqua regia to remove the gold working electrodes, and subsequently dedoped electrochemically. A negative bias was swept beginning at 0 mV to several desired values, and the UV-Vis spectra of the dedoped films were examined. A large absorption peak attributed to neutral PEDOT chains arose in the UV-Vis spectra at large dedoping biases, and a visible color change from a pale blue to a deep indigo was observed in the films. The oxidation levels of films dedoped to different biases were determined via XPS by examining the ratio between the sulfur and the phosphorus peaks. Based on this analysis, a fully doped electropolymerized PEDOT film contained a positive charge on 1 of 3 EDOT units, while a film dedoped to -1200 mV contained a positive charge on only 1 of 9 EDOT units.

The electrical conductivity of the PEDOT films was measured in a 4-point probe van der Pauw configuration. Fully doped potentiostatic films had a conductivity of 257 S/cm, fully doped galvanostatic films had a conductivity of 282 S/cm, and fully doped potentiodynamic films had a conductivity of 401 S/cm. The significant enhancement in the potentiodynamic conductivity was attributed to its morphology, specifically the dense networks that existed within the film. Electrical conductivity decreased as the films were dedoped in all cases, generally achieving values near 90 S/cm at the largest dedoping biases. The Seebeck coefficients and thermoelectric power factors were also determined for the three electropolymerization methods, and a maximum power factor of 13.6 $\mu W\ m^{-1}\ K^{-2}$ was achieved in potentiostatic polymerized PEDOT, vs. 11.9 $\mu W\ m^{-1}\ K^{-2}$ for potentiodynamic polymerized PEDOT. The larger Seebeck coefficients in the potentiostatic films when compared with the potentiodynamic films led to this performance increase. Current work is focused on improving electrical conductivity to that of spun-cast PEDOT films.

### *5.1.2 Doping and Conductivity Studies of HTAZ and FTAZ*

Though the continual improvement of device efficiency through PEDOT and other high-performing polymers is an important area of organic TE research, fundamental structure-property studies that attempt to correlate changes in polymer composition with thermoelectric behavior are just as important. Two structurally analogous polymers, HTAZ and FTAZ, were chemically doped and characterized.

HTAZ and FTAZ are not intrinsically conductive when polymerized and processed into films because they contain no free charge carriers. To inject free charges into the films a chemical doping method was developed using an $FeCl_3$ dopant. Polymer

films were spun-cast and post-treated in a dopant solution, and the doping level was controlled by changing the concentration of dopant in solution. The UV-Vis spectra of both doped polymers exhibited a clear absorption peak at energies below the polymer bandgap, due to free charge carriers in the films. The doped polymers reverted back to their original state once removed from the dopant solution, mainly due to thermal instability and reduction via atmospheric $H_2O$. Curiously, the stability of FTAZ did not increase under nitrogen, while the stability of HTAZ did. This was potentially because of the lower HOMO level in the fluorine-based polymer, which stabilizes it to water reduction processes.

The electrical conductivities of the polymers were measured in a 4-point probe setup. Though it was hypothesized that FTAZ would be more conductive than HTAZ at similar oxidation levels due to its higher SCLC mobility, this was not the measured result. The polymers were similarly conductive at comparable carrier densities, and in fact the highest measured conductivity was measured in HTAZ (16.1 S/cm). It is possible that the mobility of FTAZ was not enhanced over HTAZ in the lateral film direction, which is the direction in which the conductivity measurements are made. Perhaps more likely though was that the $FeCl_4^-$ counterions, which balance the positively-charged carriers, disrupt polymer packing and morphology. Because the mobility in FTAZ depends on this stacking, any disorder generated by the counterion would negatively affect it. Current work is focusing on measuring the lateral mobility in these materials, and also on looking at $FeCl_3$ effects on mobility and morphology.

*5.1.3 Design and Fabrication of Polymer Brush Metal-Molecule-Metal Junctions*

Though the previous two studies focused on thin polymer films where electrons travel through many chains, another possible way forward for organic thermoelectric materials is to attach single polymer chains between two electrodes. This would allow intramolecular electron transport to be the main mechanism, allowing for an increase in mobility, electrical conductivity, and TE performance. A transfer printing method was adapted and developed for polymer-brush devices to fabricate metal-molecule-metal junctions.

Kinetically-controlled transfer printing (KTP) was used to fabricate top metal contacts onto P3MT polymer-brush substrates. KTP depends on controlling the surface energy of an elastomeric stamp by changing the peel rate. The metal pattern to be transferred was fabricated onto silicon oxide donor substrates, which were briefly etched in hydrofluoric acid to enable the release of the donor pattern. The pattern was picked up by the stamp, placed onto the polymer brush receiving substrate, and the stamp was peeled away slowly in order to release the metal pattern onto the polymer brush. The final device architecture is an array of single P3MT polymer chains, anchored between an ITO bottom electrode and a gold transfer-printed top electrode.

The KTP process demonstrated advantages over other transfer-printing techniques such as nanotransfer printing (nTP). Though nTP films have a roughness that is dependent on the metal deposited layer, the KTP films could be as smooth as the donor substrate. In fact the gold electrodes used here are approximately half as rough as those fabricated with nTP (300 pm vs. 600 pm). Additionally, patterns fabricated with

nTP were prone to crack during metal deposition leading to fractured electrodes, while the KTP process produced pristine features that are crack-free.

Electrical characterization was performed in a cAFM setup. The as-grown polymer brushes possess two charge-transport regimes at different polymer lengths, both having very low beta values. The transport was clearly non-ohmic, and the mobility could be extracted from the SCLC region of the IV curve. It was found that a thermal annealing process increased thickness and improved the electrical properties of the polymer brush films. In the annealed films, transport remained non-ohmic but had the same beta value at all polymer lengths. Furthermore, the mobility of all annealed polymers increased with respect to their as-grown counterparts, and a 100-fold increase was seen in the shortest pre-annealed device. This mobility increase was likely caused by improved morphology in the annealed films due to chain extension, and the values obtained approach those for oriented P3MT films on a surface.

## 5.2 Future Work

### *5.2.1 Stretchable Electropolymerized TE Devices*

Though in principle organic thermoelectric devices can be flexible and stretchable, very few literature reports exist. This is mainly due to the brittle nature of most conjugated organic systems, which is only improved upon sacrificing some electronic properties. In other areas of organic electronics, stretchable materials have been developed using graphene,[141,142] carbon nanotubes,[143,144] and insulating polymer-metal hybrids.[145,146] In these cases, a pattern of active material that can absorb strain without failure is designed, or the substrate is pre-strained before attachment of the electronic material. We have attempted to pre-strain a commercial elastomer (3M VHB

Tape) and subsequently transfer electropolymerized PEDOT films onto it to fabricate stretchable TE devices. However, the PEDOT was irreparably cracked when the pre-strain was released, leading to failed devices.

Recently, Prof. David Martin's group was able to electropolymerize an alkene-functionalized poly(3,4-propylenedioxythiophene) (PProDOT), and post-functionalize it using thiol-ene click chemistry.[147,148] Though they used only mono thiols in the post-functionalization step, adding a dithiol would crosslink the film and allow for increased mechanical strength. This crosslinking, coupled with careful design of the working electrode, could lead to a stretchable TE device. The electropolymerization and post-functionalization steps are described in **Figure 5.1a**, while the device fabrication steps are displayed in **Figure 5.1b**. Briefly, the PProDOT alkene derivative is electropolymerized onto a patterned gold working electrode, and the gold is etched away. The PProDOT film is crosslinked with the dithiol molecule under UV light, and is then transferred onto an adhesive elastomer. Electropolymerization is an ideal method for this type of fabrication because it allows for easy patterning of the PProDOT film through patterning the working electrode. The stretchable devices can be characterized identically to the electropolymerized PEDOT films that were studied in Chapter 2.

### *5.2.2 Mobility Studies in HTAZ and FTAZ*

As mentioned in Chapter 3, a detailed study on the mobility of HTAZ and FTAZ needs to be conducted. Though the relationship between carrier concentration and mobility in organic semiconductors is not completely understood, it is known that both the amount of carriers and the amount of dopant do affect charge transport.[149,150] While the SCLC mobility of FTAZ is greatly enhanced when

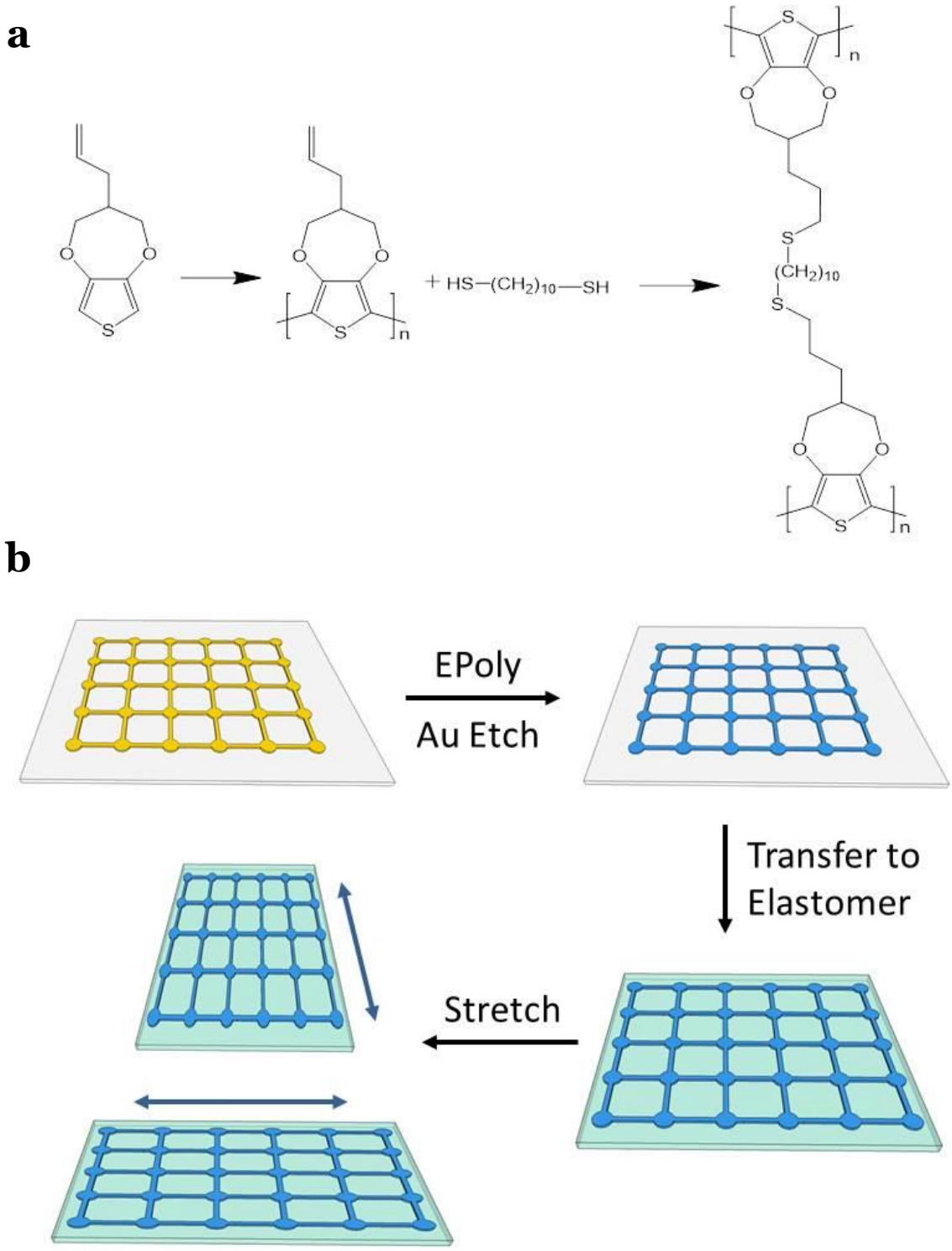


**Figure 5.1.** Stretchable TE device design

*(a)* Synthesis of crosslinkable PProDOT films. *(b)* Fabrication method for stretchable PProDOT TE devices.

compared with HTAZ, it is well known that many organic materials have anisotropic mobilities,[151–153] and it is presently unknown whether this enhancement exists in the in-plane direction. OFET devices based on HTAZ and FTAZ must be fabricated and the OFET mobilities of both polymers should be measured. The OFET mobilities can be compared with the SCLC mobilities that have been measured previously to understand any anisotropic behavior in these systems.

The OFET mobilities of doped HTAZ and FTAZ also need to be measured. It is hypothesized that the $FeCl_4^-$ counterions integrate into the organic films and disrupt inter-chain interaction, lowering the mobility. However, it is unknown if this actually occurs, and if so, which doping level is the critical point of disruption. Measuring the OFET mobility at several different doping levels will help to illuminate any effect the dopant has on charge transport. Also, XPS should be performed to assess the dopant level in the polymers. By calculating the intensity of the iron and sulfur peaks, the amount of oxidation can be accurately measured.

### *5.2.3 Thermoelectricity in HTAZ and FTAZ Films*

Though Chapter 3 studied the electrical conductivity of HTAZ and FTAZ, this is only one half of the thermoelectric power factor. The Seebeck coefficient also needs to be measured for these polymers as a function of oxidation level. This is difficult because of the instability of the doped polymers in air, coupled with the requirements for thermoelectric device fabrication and measurement involving prolonged exposure (~1 hr) to the atmosphere. However, future measurements could potentially be taken in an inert environment.

### *5.2.4 Thermoelectricity of P3MT Metal-Molecule-Metal Junctions*

In Chapter 4, a transfer-printing approach was used to fabricate P3MT-based metal-molecule-metal junctions anchored between gold and ITO. The charge transport through these molecular layers was measured, but future work will focus on determining the Seebeck coefficient of these systems. In almost every literature report of single-molecule thermoelectrics, the magnitude of the Seebeck coefficient increases as the length of the molecule increases. This is true for both aliphatic and conjugated systems,[85,154,155] and in fact some of the highest reported single-molecule Seebeck coefficients to date are seen in relatively long conjugated molecules.[65] However, these "long" molecules are still only < 5 repeat units, and theoretical work supports the idea of even longer molecules having exceptional Seebeck coefficients.[156,157] As mentioned in the introduction, measuring the Seebeck coefficient of molecular junctions is a non-trivial process. We have attempted measurements using a cAFM with an in-line external voltmeter, as described in **Figure 5.2** and originally detailed by Reddy et. al.[87,158,159] However, measurements on polymer-brush films have been unreliable up until this point, mainly due to high voltage noise. Immediate efforts will focus on proper shielding for the system to lower noise, followed by measurements on several lengths of P3MT brushes.

## 5.3 Broad Scientific Impact

The impact of the work presented herein, and that of organic thermoelectric materials in general, will not be known for some time. Though the results presented signify only incremental steps towards improved performance in organic TE devices, it is possible that the knowledge gained will help to greatly improve efficiencies in the

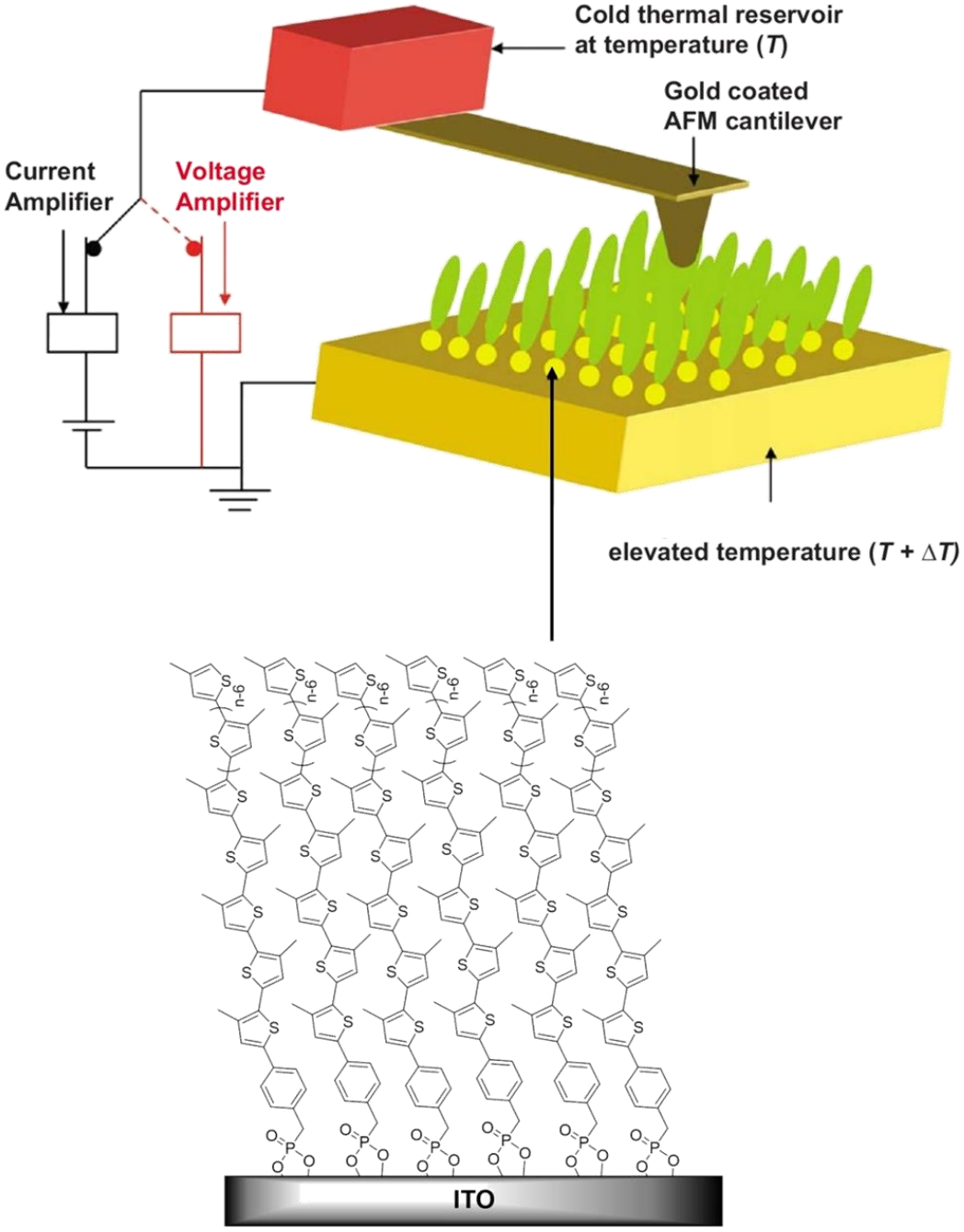


**Figure 5.2.** Schematic of a P3MT brush Seebeck coefficient measurement.

The substrate is heated to an elevated temperature, while the gold-coated cantilever is held at room temperature. Electrical measurements can be performed with the current amplifier, while voltage sensing is done with the voltage amplifier.

future. Electropolymerized PEDOT films could scale very easily into commercial device applications, while the HTAZ and FTAZ studies could aid in rational design of future TE polymers. Likewise, the fabrication of molecular devices based on single polymer layers may lead to unprecedented performance in the future. What is definitively known is that organic thermoelectric materials represent a burgeoning technology, and that continued research may lead to their implementation into the future worldwide energy picture.

## Appendix 1: XPS Spectra of EPoly PEDOT at Different Dedoping Biases

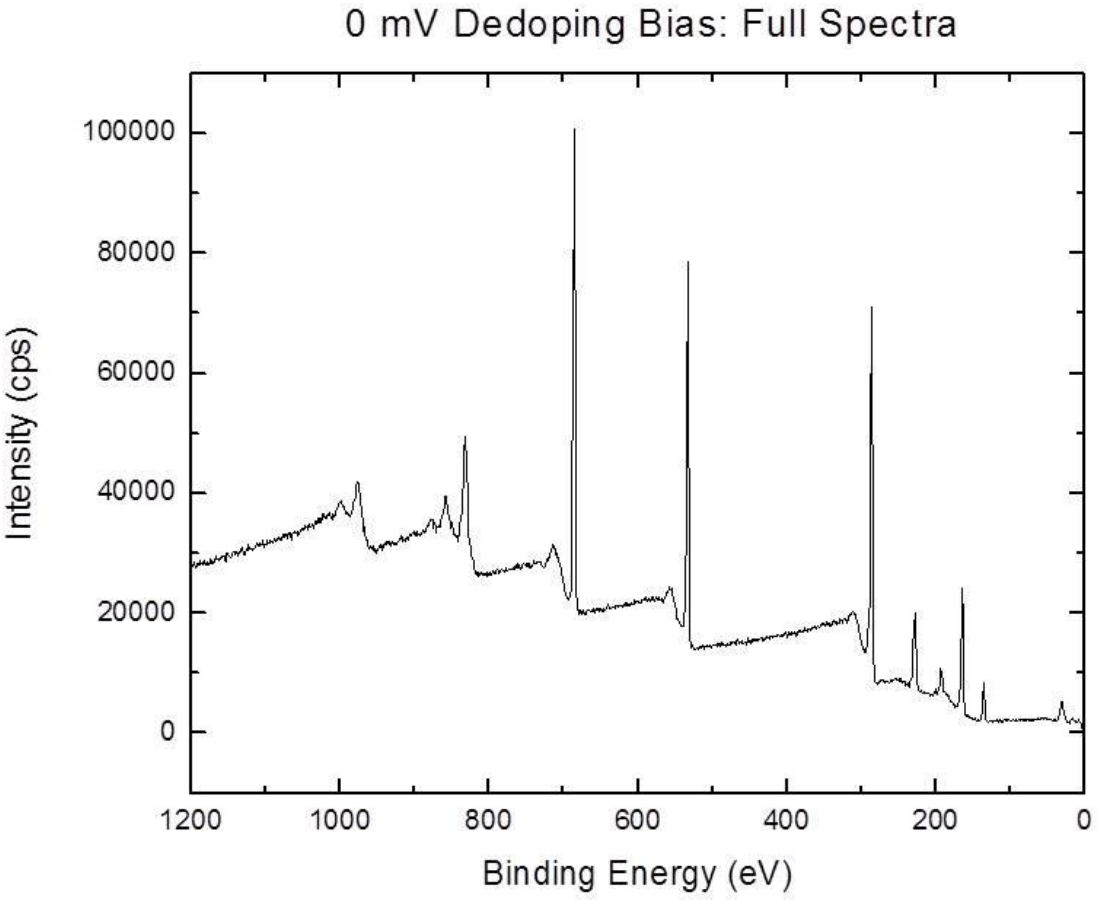

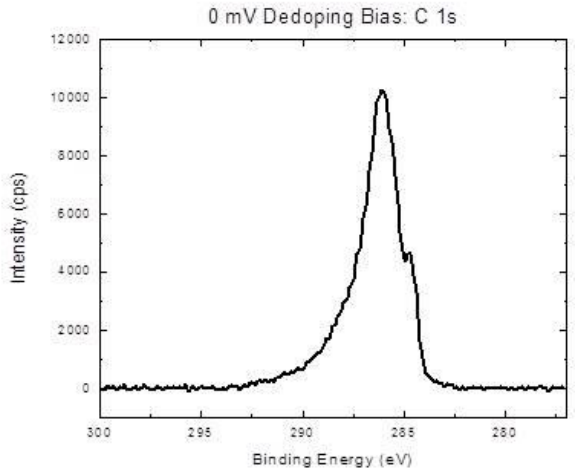
0 mV Dedoping Bias: C 1s
Intensity (cps)
Binding Energy (eV)

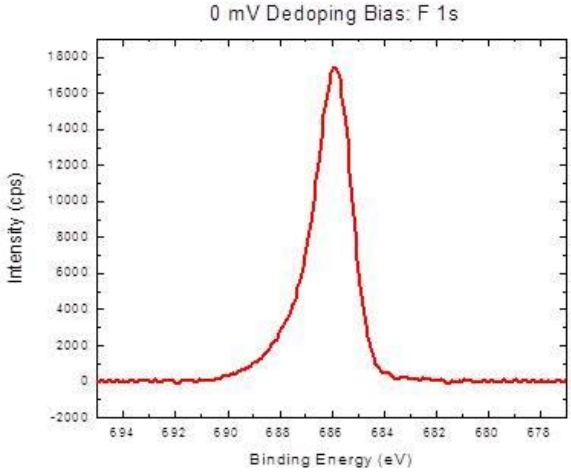
0 mV Dedoping Bias: F 1s
Intensity (cps)
Binding Energy (eV)

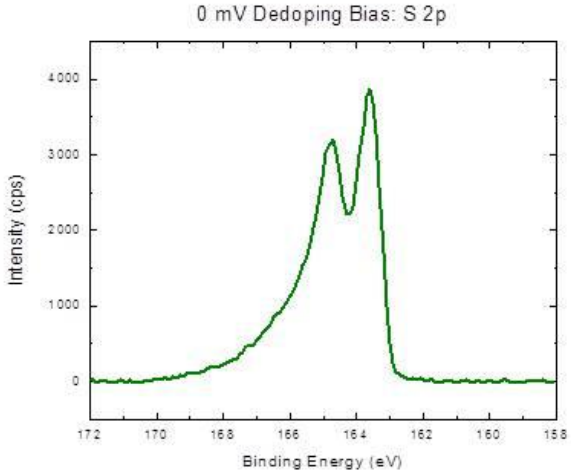
0 mV Dedoping Bias: S 2p
Intensity (cps)
Binding Energy (eV)

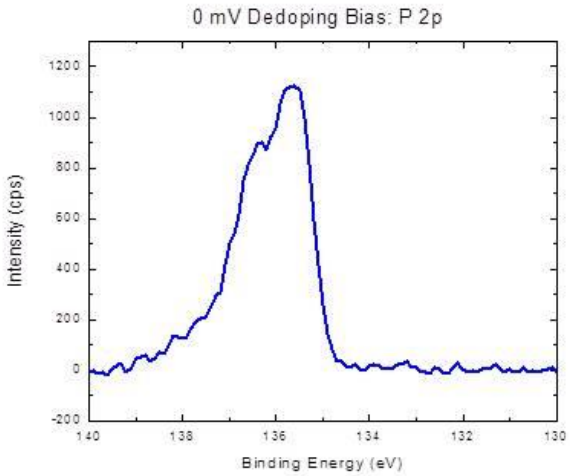
0 mV Dedoping Bias: P 2p
Intensity (cps)
Binding Energy (eV)

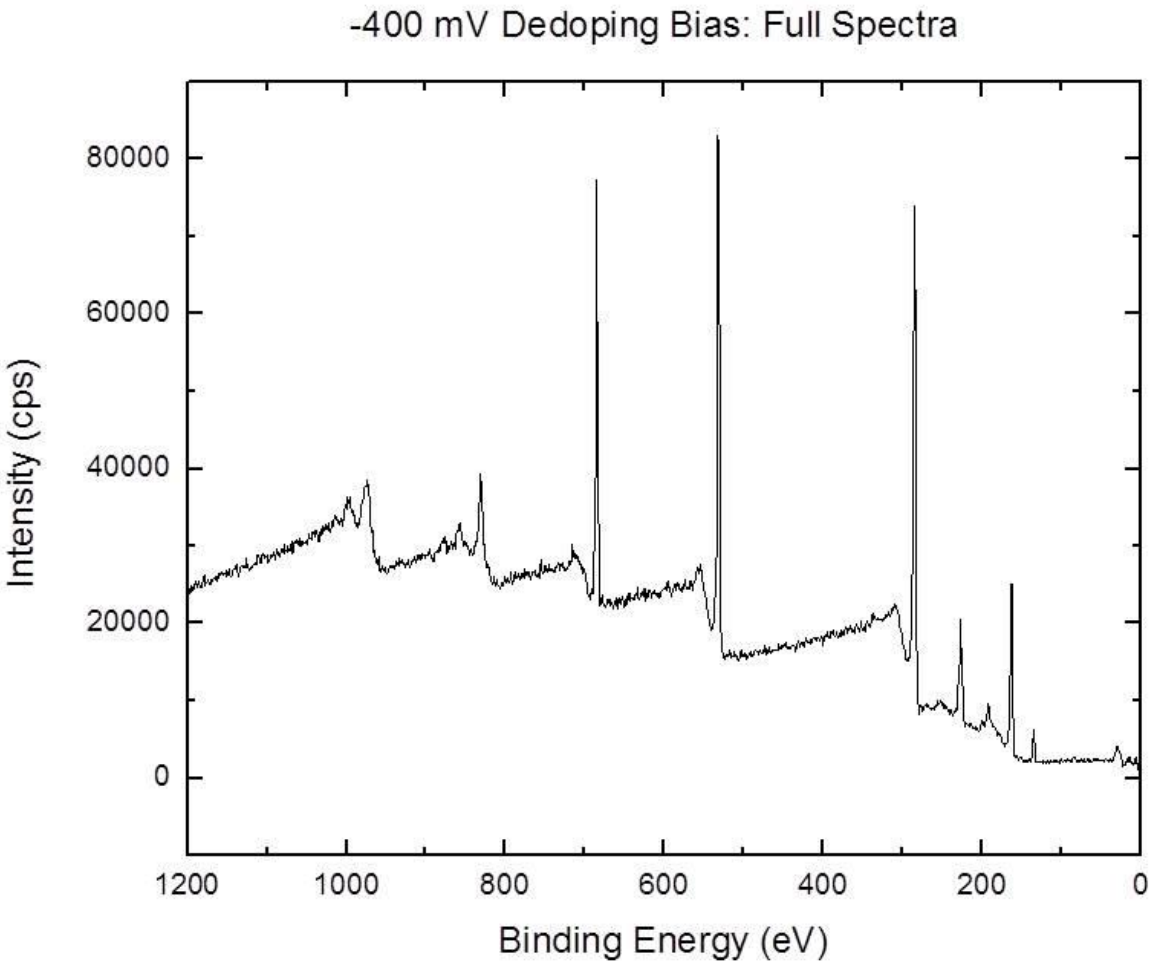
-400 mV Dedoping Bias: Full Spectra
Intensity (cps)
80000
60000
40000
20000
0
1200
1000
800
600
400
200
0
Binding Energy (eV)

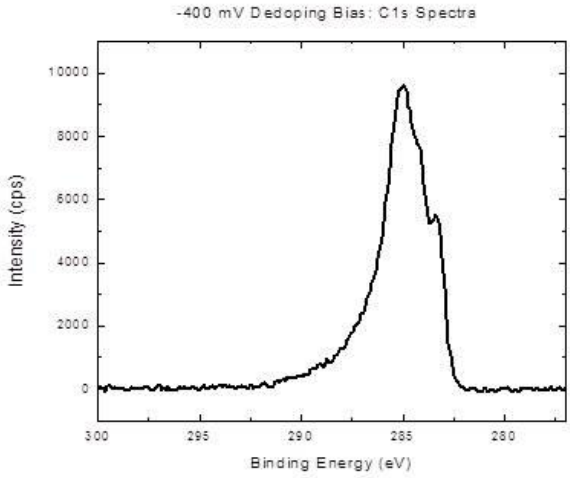
-400 mV Dedoping Bias: C1s Spectra
Intensity (cps)
Binding Energy (eV)

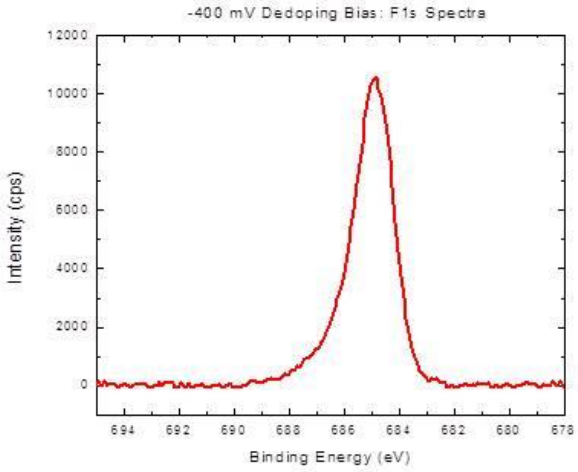
-400 mV Dedoping Bias: F1s Spectra
Intensity (cps)
Binding Energy (eV)

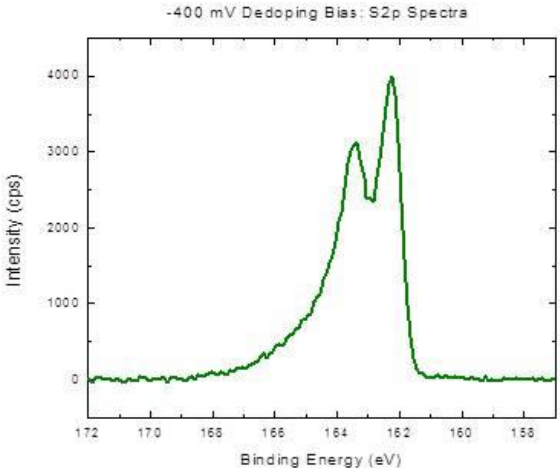
-400 mV Dedoping Bias: S2p Spectra
Intensity (cps)
Binding Energy (eV)

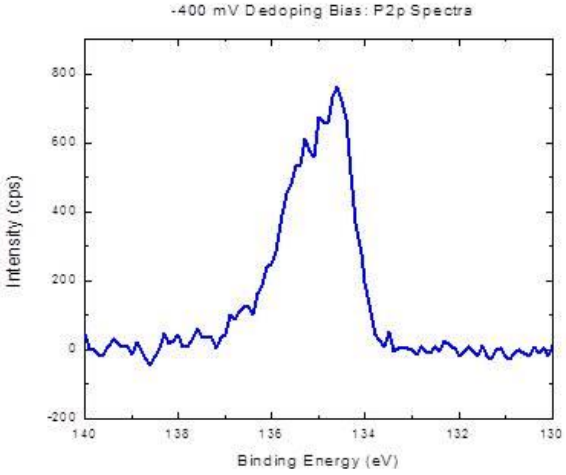
-400 mV Dedoping Bias: P2p Spectra
Intensity (cps)
Binding Energy (eV)

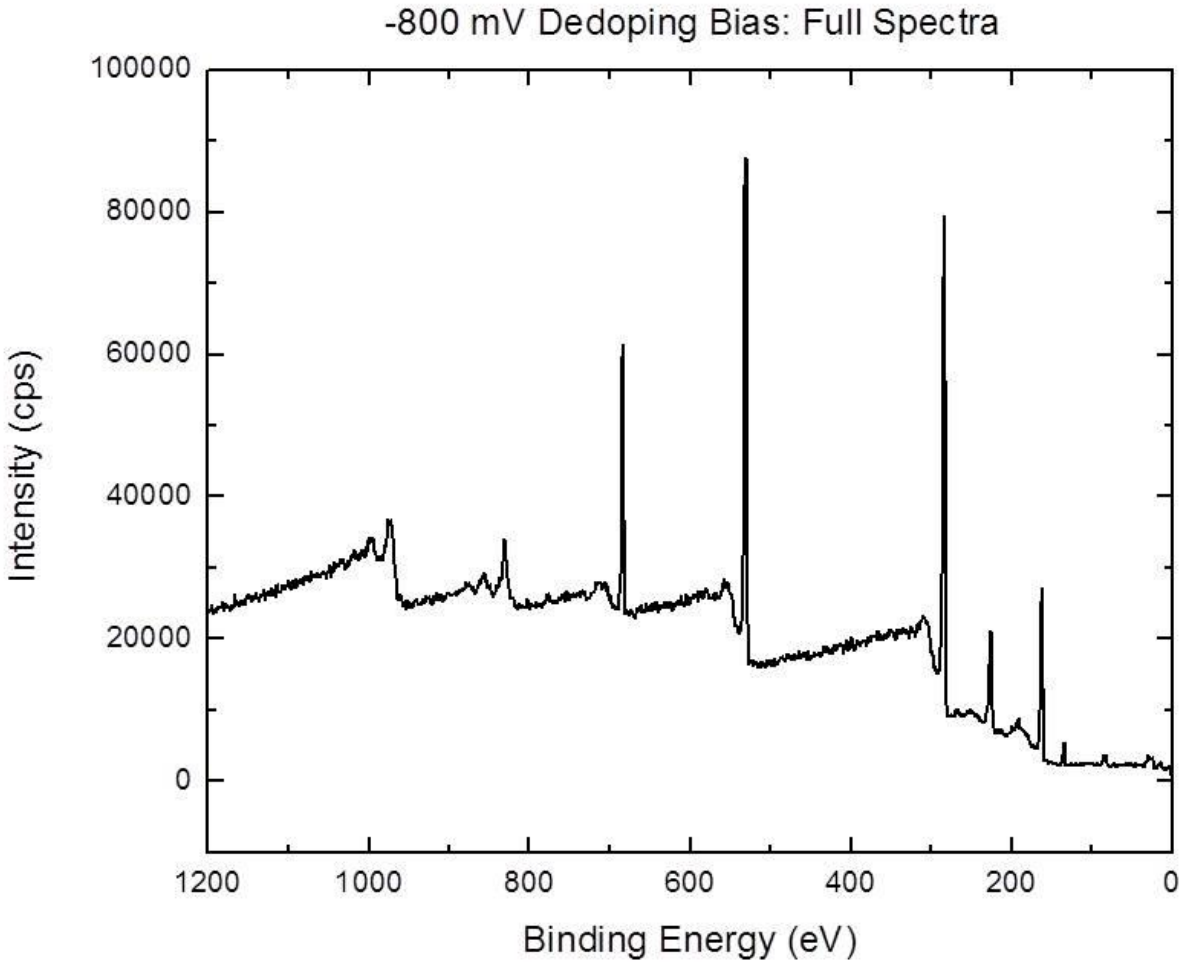
-800 mV Dedoping Bias: Full Spectra
Intensity (cps)
100000
80000
60000
40000
20000
0
1200
1000
800
600
400
200
0
Binding Energy (eV)

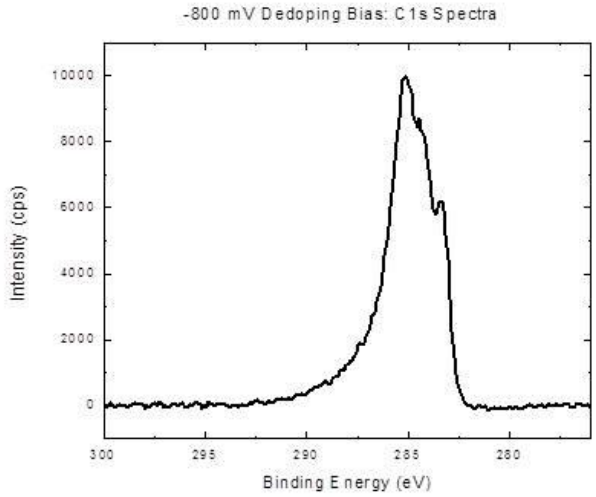
-800 mV Dedoping Bias: C1s Spectra
Intensity (cps)
Binding Energy (eV)

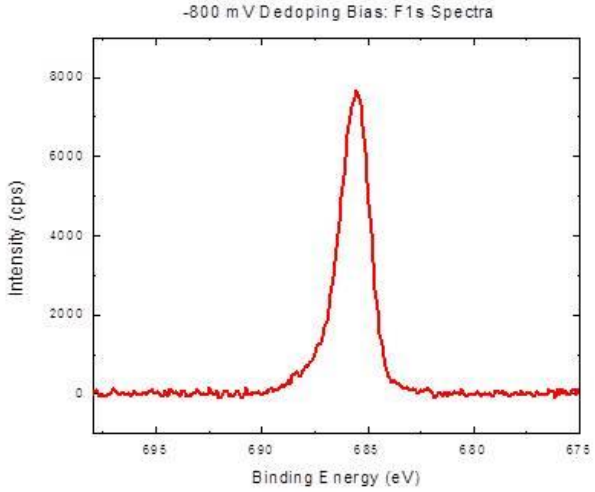
-800 mV Dedoping Bias: F1s Spectra
Intensity (cps)
Binding Energy (eV)

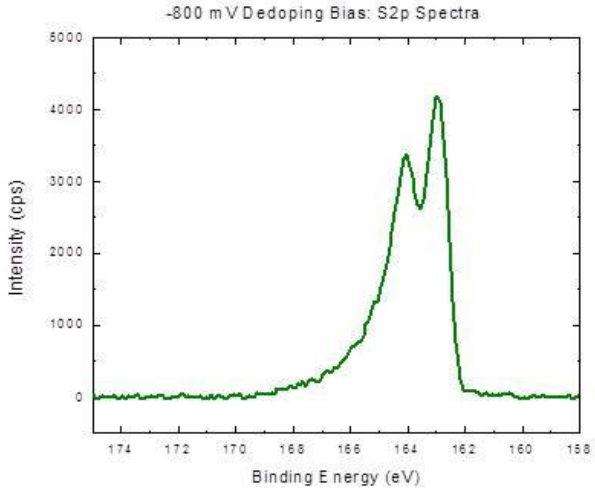
-800 mV Dedoping Bias: S2p Spectra
Intensity (cps)
Binding Energy (eV)

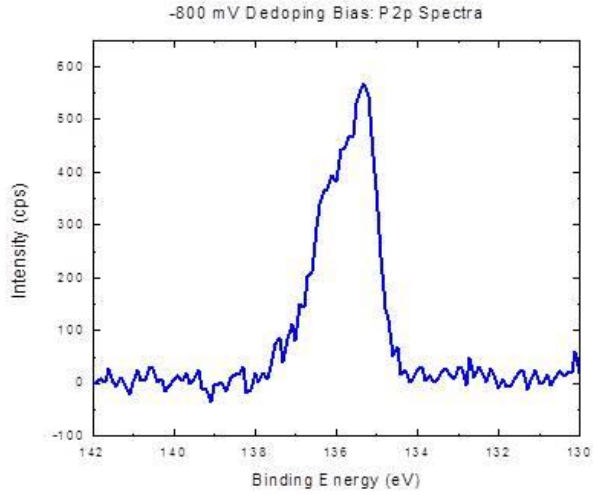
-800 mV Dedoping Bias: P2p Spectra
Intensity (cps)
Binding Energy (eV)

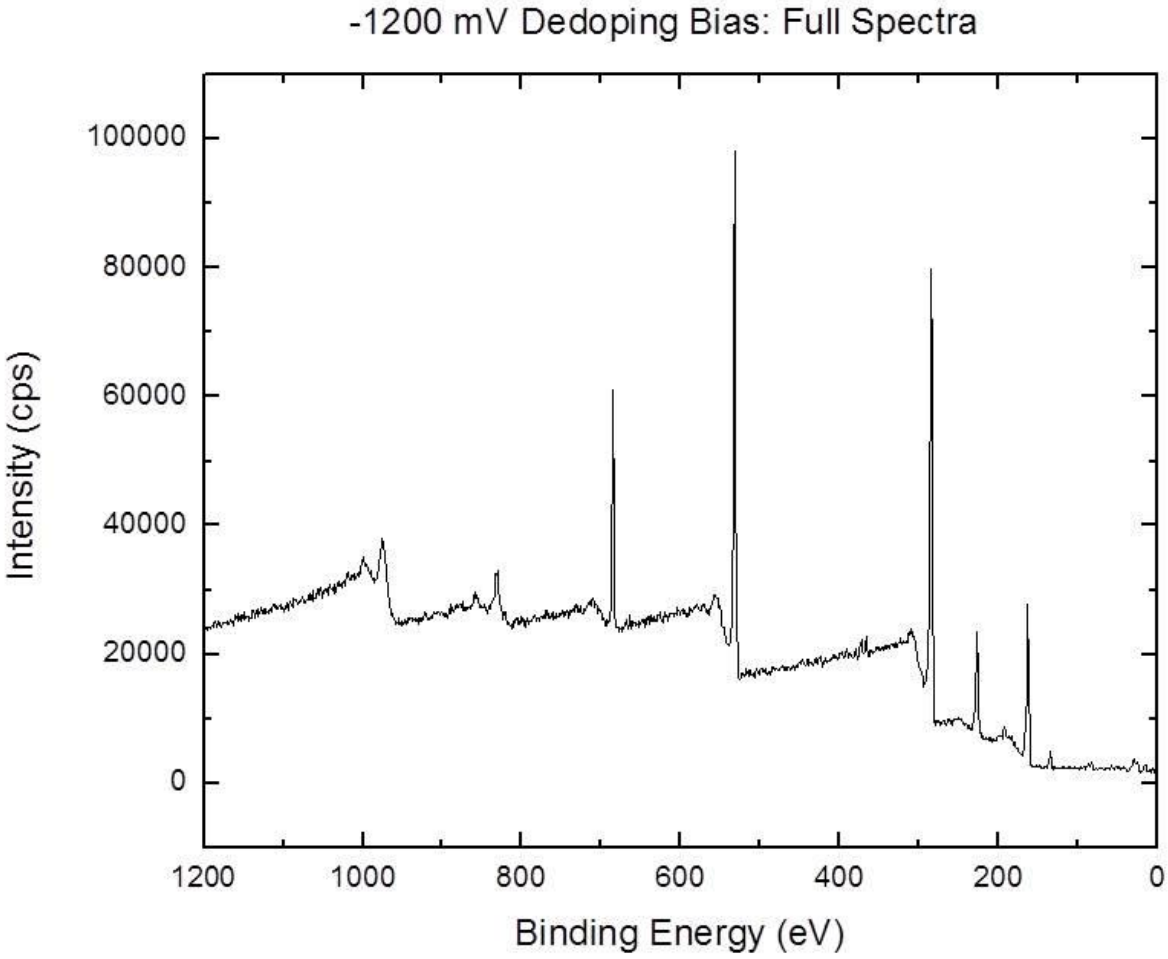
-1200 mV Dedoping Bias: Full Spectra
Intensity (cps)
100000
80000
60000
40000
20000
0
1200
1000
800
600
400
200
0
Binding Energy (eV)

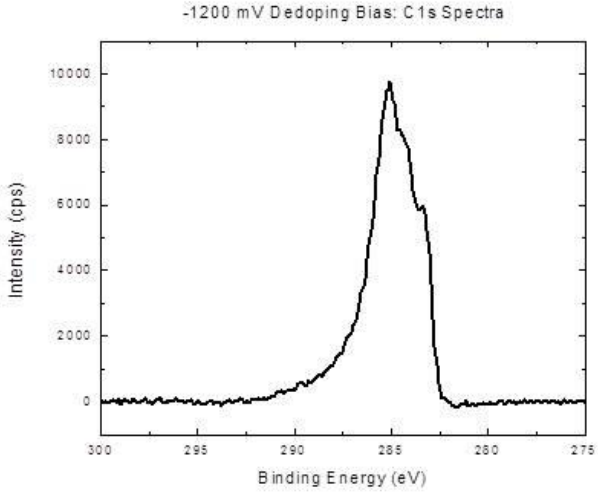
-1200 mV Dedoping Bias: C 1s Spectra
Intensity (cps)
Binding Energy (eV)

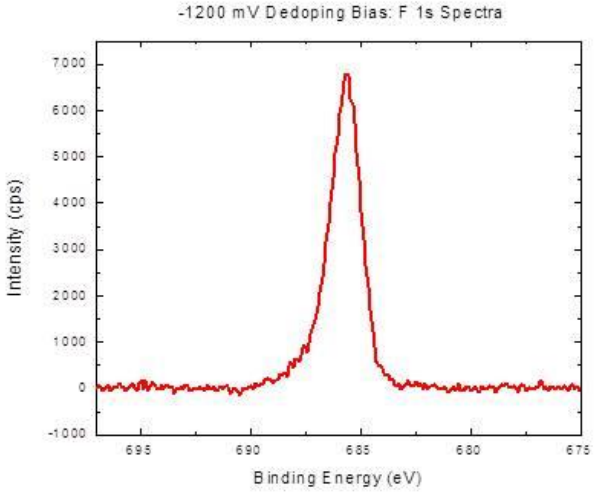
-1200 mV Dedoping Bias: F 1s Spectra
Intensity (cps)
Binding Energy (eV)

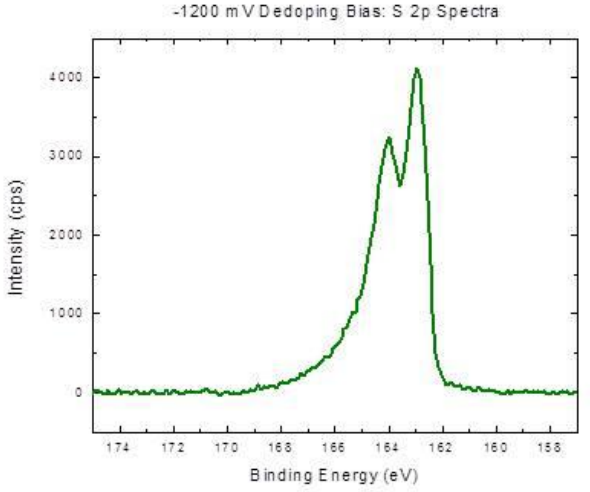
-1200 mV Dedoping Bias: S 2p Spectra
Intensity (cps)
Binding Energy (eV)

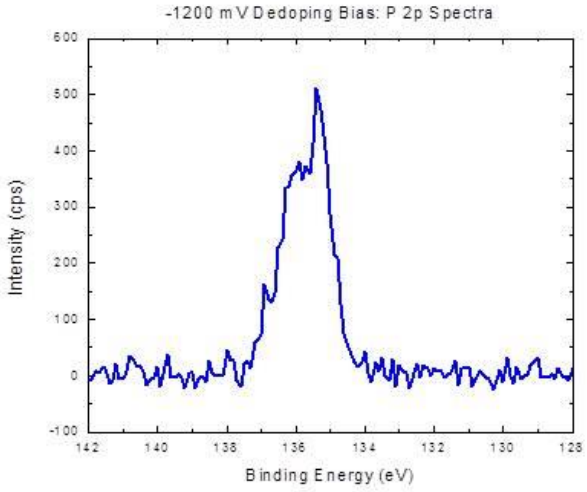
-1200 mV Dedoping Bias: P 2p Spectra
Intensity (cps)
Binding Energy (eV)

## Appendix 2: SEM Images of Dedoping Electropolymerized PEDOT Films

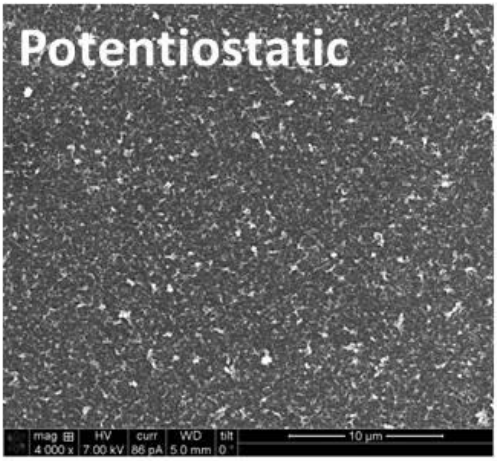


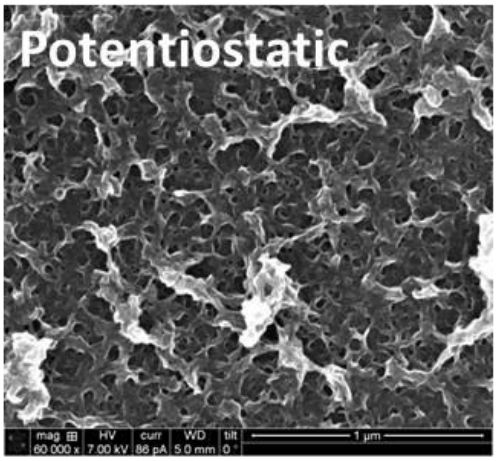


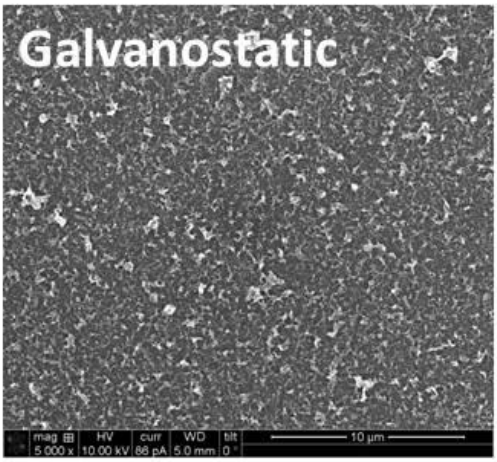


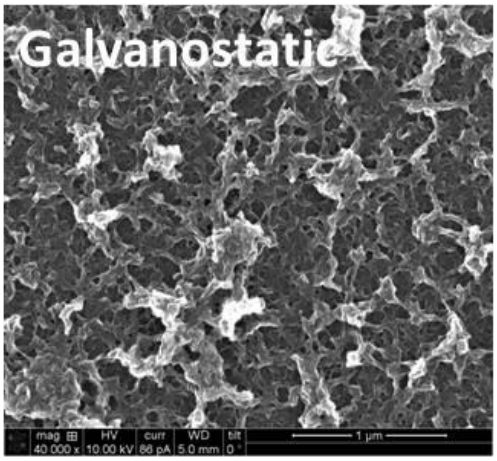


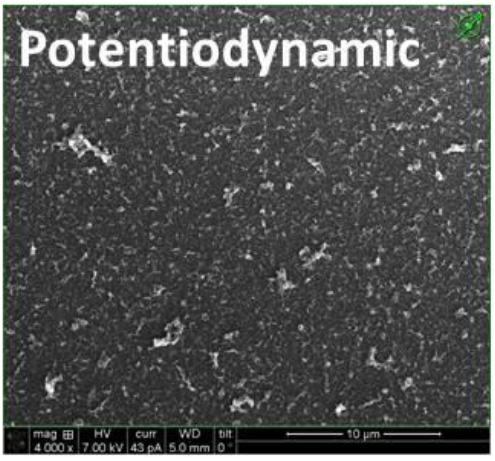


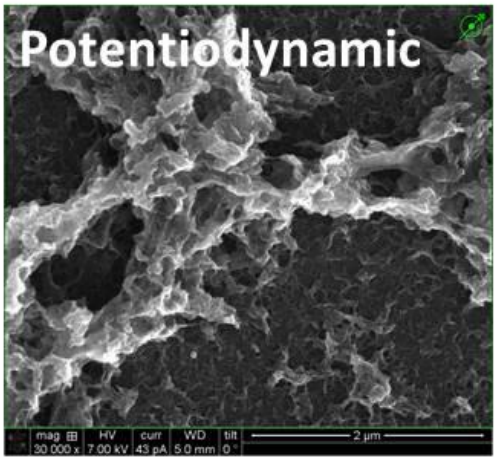

## Appendix 3: AFM Images of HTAZ and FTAZ Films

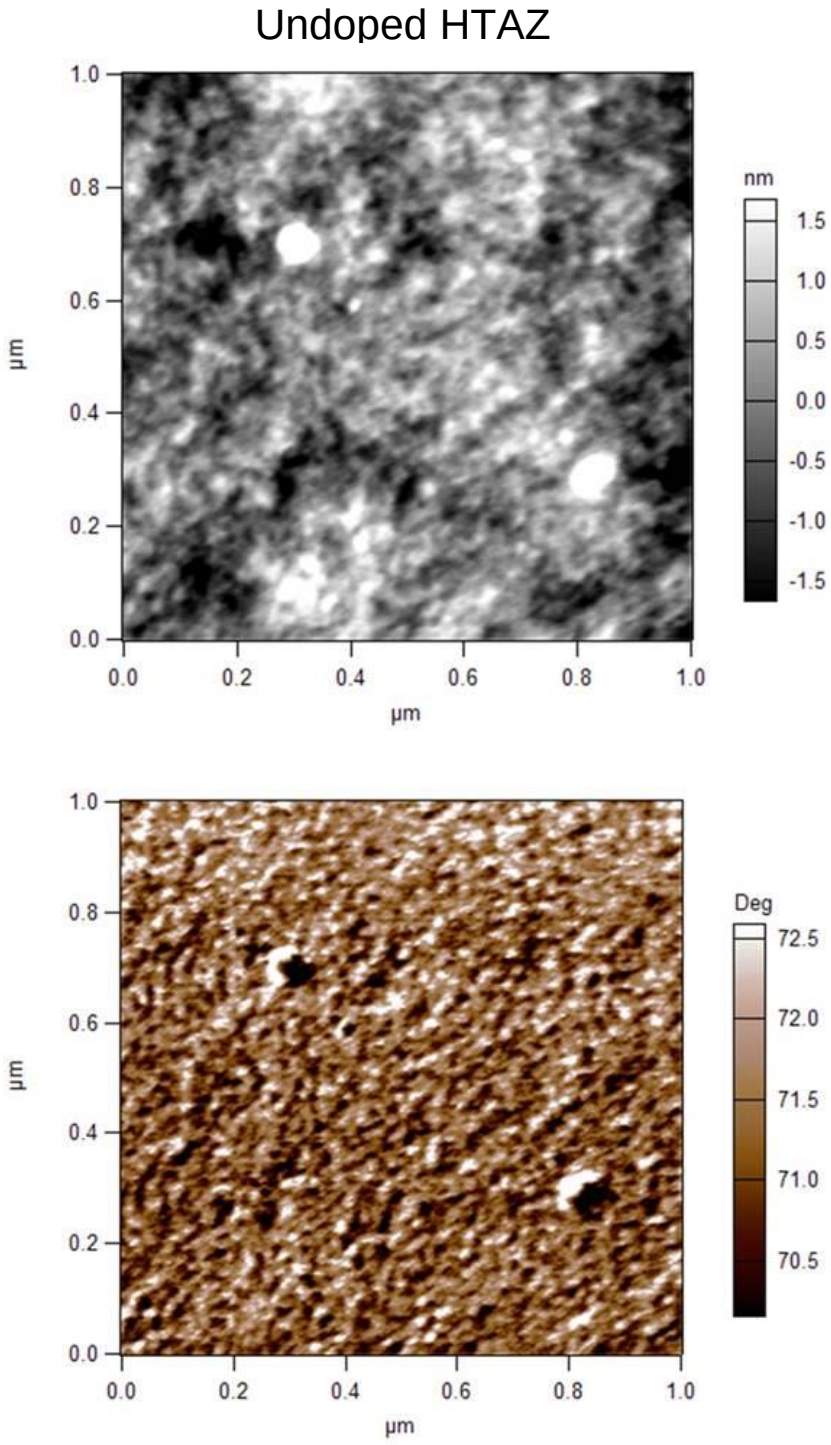

100 mM Doped HTAZ

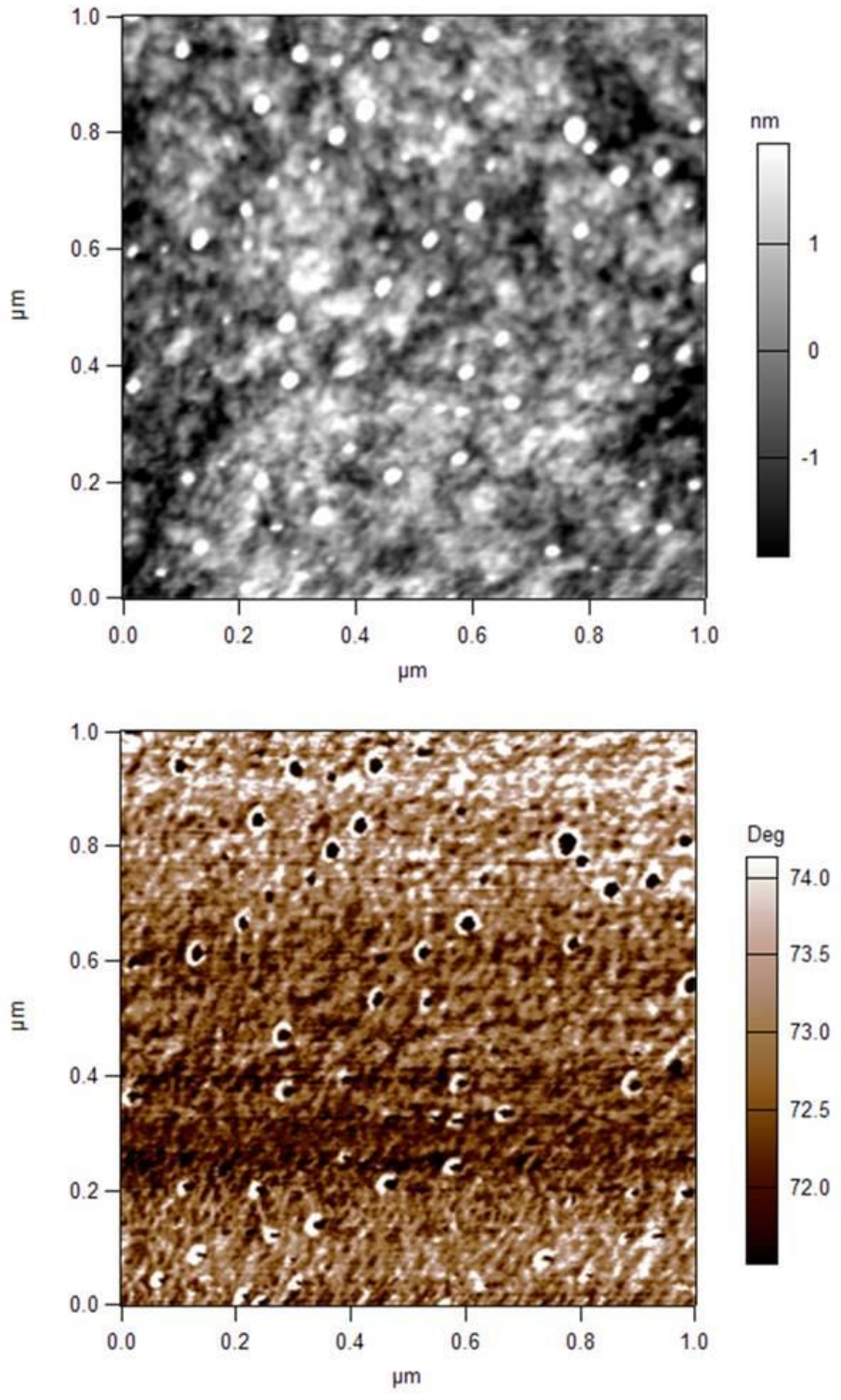

Undoped Doped FTAZ

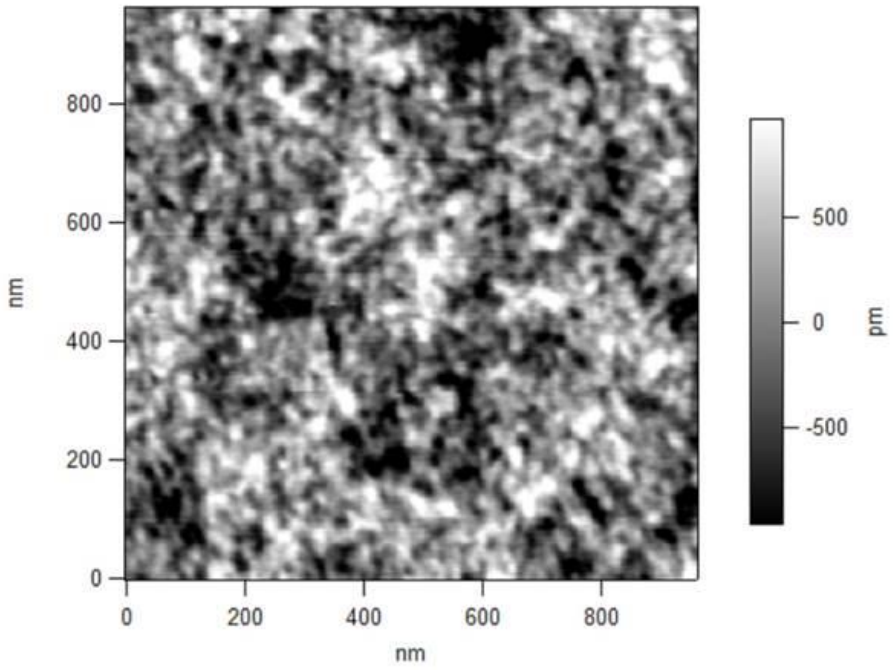


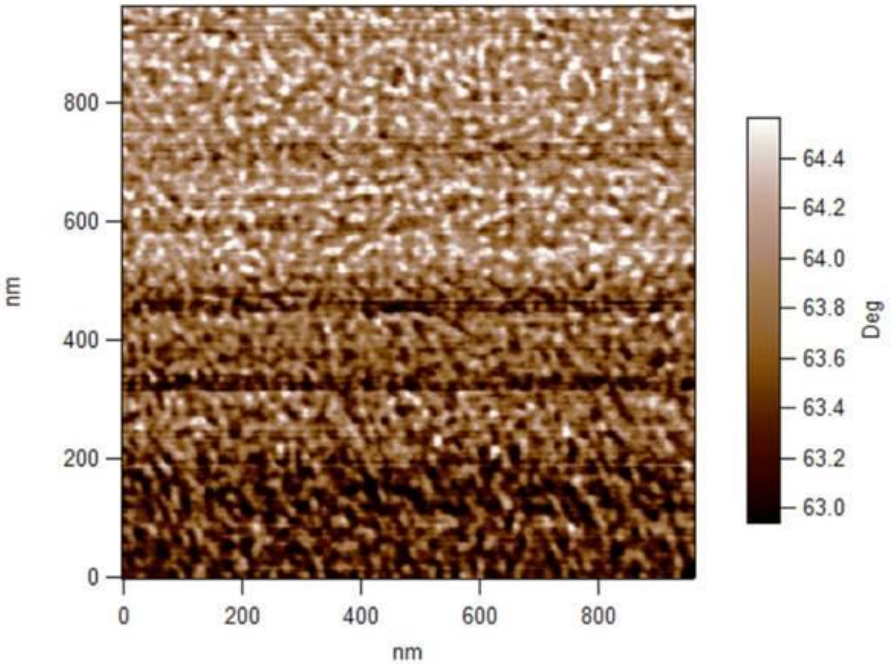

# 100 mM Doped FTAZ

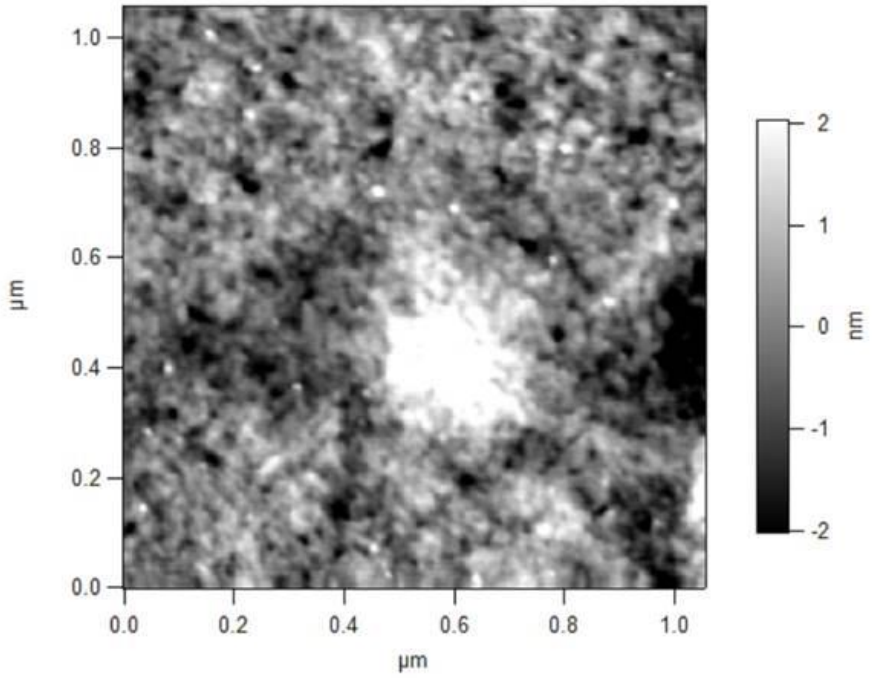


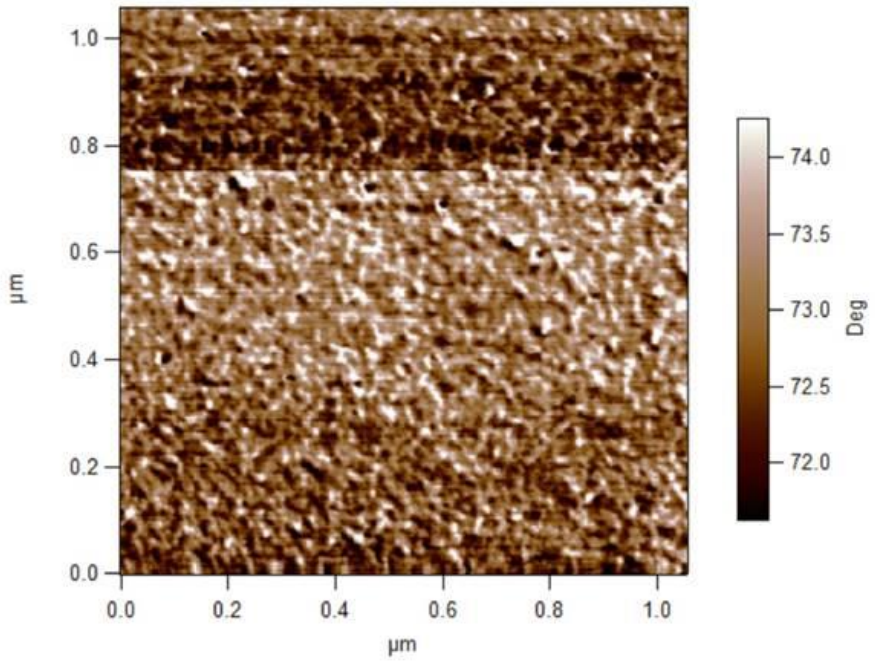

## REFERENCES


(1) Crossette, B.; Kollodge, R.; Puchalik, R.; Chalijub, M. *The State of World Population 2011*; New York, 2011.

(2) *2014 Key World Energy Statistics*; Paris, 2014.

(3) Shakouri, A. *Annu. Rev. Mater. Res.* **2011**, *41* (1), 399–431.

(4) Eva-Dry 1100 Petite Dehumidifier https://www.eva-dry.com/dehumidifiers/eva-dry-1100-petite-dehumidifier/ (accessed Jun 28, 2015).

(5) Curiosity Rover https://www.nasa.gov/mission_pages/msl/index.html (accessed Jun 28, 2015).

(6) Gentherm Climate Seats http://www.gentherm.com/en/page/climate-seats (accessed Jun 28, 2015).

(7) Thermoelectric Wine Coolers http://www.newair.com/wine-beverage-coolers (accessed Jun 28, 2015).

(8) Guo, X.; Baumgarten, M.; Müllen, K. *Prog. Polym. Sci.* **2013**, *38* (12), 1832–1908.

(9) Heliatek: the future is light http://www.heliatek.com/ (accessed Jun 28, 2015).

(10) OLED S9C Series Smart TV http://www.samsung.com/us/video/tvs/KN55S9CAFXZA (accessed Jun 28, 2015).

(11) Velmre, E. *Proc. Est. Acad. Sci. Eng.* **2007**, *13* (4), 276–282.

(12) *A Dictionary of Scientists*; Oxford University Press, 2003.

(13) Bell, L. E. *Science* **2008**, *321* (5895), 1457–1461.

(14) DiSalvo, F. J. *Science* **1999**, *285* (5428), 703–706.

(15) Chasmar, R. P.; Stratton, R. *J. Electron. Control* **1959**, *7* (1), 52–72.

(16) Sofo, J. O.; Mahan, G. D. *Phys. Rev. B* **1994**, *49* (7), 4565–4570.

(17) Mahan, G. D. *J. Appl. Phys.* **1989**, *65* (4), 1578.

(18) Venkatasubramanian, R.; Siivola, E.; Colpitts, T.; O'Quinn, B. *Nature* **2001**, *413* (6856), 597–602.

(19) Harman, T. C.; Taylor, P. J.; Walsh, M. P.; LaForge, B. E. *Science* **2002**, *297* (5590), 2229–2232.

(20) Hsu, K. F.; Loo, S.; Guo, F.; Chen, W.; Dyck, J. S.; Uher, C.; Hogan, T.; Polychroniadis, E. K.; Kanatzidis, M. G. *Science* **2004**, *303* (5659), 818–821.

(21) Heremans, J. P.; Jovovic, V.; Toberer, E. S.; Saramat, A.; Kurosaki, K.; Charoenphakdee, A.; Yamanaka, S.; Snyder, G. J. *Science* **2008**, *321* (5888), 554–557.

(22) Letheby, H. *J. Chem. Soc.* **1862**, *15*, 161.

(23) Kearns, D.; Calvin, M. *J. Chem. Phys.* **1958**, *29* (4), 950.

(24) Kovacic, P.; Kyriakis, A. *J. Am. Chem. Soc.* **1963**, *85* (4), 454–458.

(25) Bolto, B.; McNeill, R.; Weiss, D. *Aust. J. Chem.* **1963**, *16* (6), 1090–1103.

(26) McDonald, R. N.; Campbell, T. W. *J. Am. Chem. Soc.* **1960**, *82* (17), 4669–4671.

(27) Chiang, C.; Fincher, C.; Park, Y.; Heeger, A.; Shirakawa, H.; Louis, E.; Gau, S.; MacDiarmid, A. *Phys. Rev. Lett.* **1977**, *39* (17), 1098–1101.

(28) Tang, C. W.; VanSlyke, S. A. *Appl. Phys. Lett.* **1987**, *51* (12), 913.

(29) Koezuka, H.; Tsumura, A.; Ando, T. *Synth. Met.* **1987**, *18* (1-3), 699–704.

(30) The Nobel Prize in Chemistry 2000 http://www.nobelprize.org/nobel_prizes/chemistry/laureates/2000/ (accessed Jun 30, 2015).

(31) Basescu, N.; Liu, Z.-X.; Moses, D.; Heeger, A. J.; Naarmann, H.; Theophilou, N. *Nature* **1987**, *327*, 403–405.

(32) Reynolds, J. R.; Chien, J. C. W.; Karasz, F. E.; Lillya, C. P.; Curran, D. J. *J. Chem. Soc. Chem. Commun.* **1982**, No. 23, 1358–1359.

(33) Kuivalainen, P.; Stubb, H.; Isotalo, H.; Yli-Lahti, P.; Holmström, C. *Phys. Rev. B* **1985**, *31* (12), 7900–7909.

(34) Poudel, B.; Hao, Q.; Ma, Y.; Lan, Y.; Minnich, A.; Yu, B.; Yan, X.; Wang, D.; Muto, A.; Vashaee, D.; Chen, X.; Liu, J.; Dresselhaus, M. S.; Chen, G.; Ren, Z. *Science* **2008**, *320* (5876), 634–638.

(35) Moses, D.; Denenstein, A. *Phys. Rev. B* **1984**, *30* (4), 2090–2097.

(36) Nogami, Y.; Kaneko, H.; Ishiguro, T.; Takahashi, A.; Tsukamoto, J.; Hosoito, N. *Solid State Commun.* **1990**, *76* (5), 583–586.

(37) Mateeva, N.; Niculescu, H.; Schlenoff, J.; Testardi, L. R. *J. Appl. Phys.* **1998**, *83* (6), 3111–3117.

(38) Hiroshige, Y.; Ookawa, M.; Toshima, N. *Synth. Met.* **2006**, *156* (21-24), 1341–1347.

(39) Lévesque, I.; Bertrand, P.-O.; Blouin, N.; Leclerc, M.; Zecchin, S.; Zotti, G.; Ratcliffe, C. I.; Klug, D. D.; Gao, X.; Gao, F.; Tse, J. S. *Chem. Mater.* **2007**, *19* (8), 2128–2138.

(40) Aïch, R. B.; Blouin, N.; Bouchard, A.; Leclerc, M. *Chem. Mater.* **2009**, *21* (4), 751–757.

(41) Endrődi, B.; Mellár, J.; Gingl, Z.; Visy, C.; Janáky, C. *J. Phys. Chem. C* **2015**, *119* (16), 8472–8479.

(42) Zhang, Q.; Sun, Y.; Xu, W.; Zhu, D. *Macromolecules* **2014**, *47* (2), 609–615.

(43) Lu, G.; Bu, L.; Li, S.; Yang, X. **2014**, 1–6.

(44) Sun, J.; Yeh, M. L.; Jung, B. J.; Zhang, B.; Feser, J.; Majumdar, A.; Katz, H. E. *Macromolecules* **2010**, *43* (6), 2897–2903.

(45) Lu, B.; Chen, S.; Xu, J.; Zhao, G. *Synth. Met.* **2013**, *183*, 8–15.

(46) Clevios™ Conductive, Transparent and Flexible Polymers http://www.heraeus-clevios.com/en/home/clevios-homepage.aspx (accessed Jul 2, 2015).

(47) Döbbelin, M.; Marcilla, R.; Salsamendi, M.; Pozo-Gonzalo, C.; Carrasco, P. M.; Pomposo, J. A.; Mecerreyes, D. *Chem. Mater.* **2007**, *19* (9), 2147–2149.

(48) Luo, J.; Billep, D.; Waechtler, T.; Otto, T.; Toader, M.; Gordan, O.; Sheremet, E.; Martin, J.; Hietschold, M.; Zahn, D. R. T.; Gessner, T. *J. Mater. Chem. A* **2013**, *1* (26), 7576–7583.

(49) Mengistie, D. A.; Chen, C.-H.; Boopathi, K. M.; Pranoto, F. W.; Li, L.-J.; Chu, C.-W. *ACS Appl. Mater. Interfaces* **2015**, *7* (1), 94–100.

(50) Tsai, T.-C.; Chang, H.-C.; Chen, C.-H.; Huang, Y.-C.; Whang, W.-T. *Org. Electron.* **2014**, *15*, 641–645.

(51) Park, H.; Lee, S. H.; Kim, F. S.; Choi, H. H.; Cheong, I. W.; Kim, J. H. *J. Mater. Chem. A* **2014**, *2* (18), 6532–6539.

(52) Kim, G.-H.; Shao, L.; Zhang, K.; Pipe, K. P. *Nat. Mater.* **2013**, *12* (8), 719–723.

(53) Lee, S. H.; Park, H.; Kim, S.; Son, W.; Cheong, I. W.; Kim, J. H. *J. Mater. Chem. A* **2014**, *2* (20), 7288–7294.

(54) Lee, S. H.; Park, H.; Son, W.; Choi, H. H.; Kim, J. H. *J. Mater. Chem. A* **2014**, *2*, 13380–13387.

(55) Bubnova, O.; Khan, Z. U.; Malti, A.; Braun, S.; Fahlman, M.; Berggren, M.; Crispin, X. *Nat. Mater.* **2011**, *10* (6), 429–433.

(56) Park, T.; Park, C.; Kim, B.; Shin, H.; Kim, E. *Energy Environ. Sci.* **2013**, *6*, 788–792.

(57) Bubnova, O.; Khan, Z. U.; Wang, H.; Braun, S.; Evans, D. R.; Fabretto, M.; Hojati-Talemi, P.; Dagnelund, D.; Arlin, J.-B.; Geerts, Y. H.; Desbief, S.; Breiby, D. W.; Andreasen, J. W.; Lazzaroni, R.; Chen, W. M.; Zozoulenko, I.; Fahlman, M.; Murphy, P. J.; Berggren, M.; Crispin, X. *Nat. Mater.* **2013**, *13* (2), 190–194.

(58) Prins, P.; Grozema, F. C.; Schins, J. M.; Patil, S.; Scherf, U.; Siebbeles, L. D. A. *Phys. Rev. Lett.* **2006**, *96* (14), 146601.

(59) Aviram, A.; Ratner, M. A. *Chem. Phys. Lett.* **1974**, *29* (2), 277–283.

(60) Reed, M. A.; Zhou, C.; Muller, C. J.; Burgin, T. P.; Tour, J. M. *Science* **1997**, *278* (5336), 252–254.

(61) Ratner, M. *Nat. Nanotechnol.* **2013**, *8* (6), 378–381.

(62) Joachim, C.; Gimzewski, J. K.; Aviram, A. *Nature* **2000**, *408*, 541–548.

(63) Nitzan, A. *Annu. Rev. Phys. Chem.* **2001**, *52*, 681–750.

(64) Su, T. A.; Li, H.; Steigerwald, M. L.; Venkataraman, L.; Nuckolls, C. *Nat. Chem.* **2015**, *7* (3), 215–220.

(65) Dell, E. J.; Capozzi, B.; Xia, J.; Venkataraman, L.; Campos, L. M. *Nat. Chem.* **2015**, *7* (3), 209–214.

(66) Kaliginedi, V.; Moreno-García, P.; Valkenier, H.; Hong, W.; García-Suárez, V. M.; Buiter, P.; Otten, J. L. H.; Hummelen, J. C.; Lambert, C. J.; Wandlowski, T. *J. Am. Chem. Soc.* **2012**, *134* (11), 5262–5275.

(67) Bruot, C.; Hihath, J.; Tao, N. *Nat. Nanotechnol.* **2012**, *7* (1), 35–40.

(68) Kim, B.; Choi, S. H.; Zhu, X.-Y.; Frisbie, C. D. *J. Am. Chem. Soc.* **2011**, *133* (49), 19864–19877.

(69) Engelkes, V. B.; Beebe, J. M.; Frisbie, C. D. *J. Am. Chem. Soc.* **2004**, *126* (43), 14287–14296.

(70) Beebe, J.; Kim, B.; Gadzuk, J.; Daniel Frisbie, C.; Kushmerick, J. *Phys. Rev. Lett.* **2006**, *97* (2), 1–4.

(71) Thuo, M. M.; Reus, W. F.; Nijhuis, C. A.; Barber, J. R.; Kim, C.; Schulz, M. D.; Whitesides, G. M. *J. Am. Chem. Soc.* **2011**, *133* (9), 2962–2975.

(72) Chiechi, R. C.; Weiss, E. A.; Dickey, M. D.; Whitesides, G. M. *Angew. Chem. Int. Ed. Engl.* **2008**, *47* (1), 142–144.

(73) Nijhuis, C. A.; Reus, W. F.; Barber, J. R.; Whitesides, G. M. *J. Phys. Chem. C* **2012**, *116* (26), 14139–14150.

(74) Wang, G.; Yoo, H.; Na, S.-I.; Kim, T.-W.; Cho, B.; Kim, D.-Y.; Lee, T. *Thin Solid Films* **2009**, *518* (2), 824–828.

(75) Akkerman, H. B.; Blom, P. W. M.; de Leeuw, D. M.; de Boer, B. *Nature* **2006**, *441* (7089), 69–72.

(76) Akkerman, H. B.; Naber, R. C. G.; Jongbloed, B.; van Hal, P. a; Blom, P. W. M.; de Leeuw, D. M.; de Boer, B. *Proc. Natl. Acad. Sci. U. S. A.* **2007**, *104* (27), 11161–11166.

(77) Kronemeijer, a. J.; Huisman, E. H.; Akkerman, H. B.; Goossens, a. M.; Katsouras, I.; van Hal, P. a.; Geuns, T. C. T.; van der Molen, S. J.; Blom, P. W. M.; de Leeuw, D. M. *Appl. Phys. Lett.* **2010**, *97* (17), 173302.

(78) Oxide, G.; Layer, M. B. **2012**, No. 9, 8022–8029.

(79) Wang, G.; Kim, Y.; Choe, M.; Kim, T.; Lee, T. *Adv. Mater.* **2011**, *23*, 755–760.

(80) Seo, S.; Min, M.; Lee, S. M.; Lee, H. *Nat. Commun.* **2013**, *4*, 1920.

(81) Seo, S.; Min, M.; Lee, J.; Lee, T.; Choi, S.-Y.; Lee, H. *Angew. Chem. Int. Ed.* **2012**, *51* (1), 108–112.

(82) Wang, G.; Na, S.-I.; Kim, T.-W.; Kim, Y.; Park, S.; Lee, T. *Org. Electron.* **2012**, *13* (5), 771–777.

(83) Niskala, J. R.; You, W. *J. Am. Chem. Soc.* **2009**, *131* (37), 13202–13203.

(84) Niskala, J. R.; Rice, W. C.; Bruce, R. C.; Merkel, T. J.; Tsui, F.; You, W. *J. Am. Chem. Soc.* **2012**, *134* (29), 12072–12082.

(85) Reddy, P.; Jang, S.-Y.; Segalman, R. A.; Majumdar, A. *Science* **2007**, *315* (5818), 1568–1571.

(86) Tan, A.; Sadat, S.; Reddy, P. *Appl. Phys. Lett.* **2010**, *96* (1), 013110.

(87) Tan, A.; Balachandran, J.; Sadat, S.; Gavini, V.; Dunietz, B. D.; Jang, S.-Y.; Reddy, P. *J. Am. Chem. Soc.* **2011**, *133* (23), 8838–8841.

(88) Widawsky, J. R.; Chen, W.; Vazquez, H.; Kim, T.; Breslow, R.; Hybertsen, M. S.; Venkataraman, L. *Nano Lett.* **2013**.

(89) Balachandran, J.; Reddy, P.; Dunietz, B. D.; Gavini, V. *J. Phys. Chem. Lett.* **2012**, *3* (15), 1962–1967.

(90) Yee, S. K.; Malen, J. A.; Majumdar, A.; Segalman, R. A. *Nano Lett.* **2011**, *11* (10), 4089–4094.

(91) Wang, H.; Ail, U.; Gabrielsson, R.; Berggren, M.; Crispin, X. **2015**, *5* (11), 1–6.

(92) Bidan, G. In *Electropolymerization: Concepts, Materials and Applications - Wiley Online Library*; Cosnier, S., Karyakin, A., Eds.; Wiley-VCH: Weinheim, Germany, 2010; pp 1–26.

(93) Vorotyntsev, M. A.; Zinovyeva, V. A.; Konev, D. V. In *Electropolymerization: Concepts, Materials and Applications*; Cosnier, S., Karyakin, A., Eds.; Wiley-VCH: Weinheim, Germany, 2010; pp 27–50.

(94) Culebras, M.; Uriol, B.; Gómez, C. M.; Cantarero, A. *Phys. Chem. Chem. Phys.* **2015**, *17* (23), 15140–15145.

(95) Diaz, A. F.; Castillo, J. I.; Logan, J. A.; Lee, W.-Y. *J. Electroanal. Chem. Interfacial Electrochem.* **1981**, *129*, 115–132.

(96) Diaz, A. F.; Logan, J. A. *J. Electroanal. Chem. Interfacial Electrochem.* **1980**, *111*, 111–114.

(97) Genies, E. M.; Tsintavis, C. *J. Electroanal. Chem. Interfacial Electrochem.* **1985**, *195*, 109–128.

(98) Tourillon, G.; Garnier, F. *J. Electroanal. Chem. Interfacial Electrochem.* **1982**, *135*, 173–178.

(99) Danieli, R.; Taliani, C.; Zamboni, R.; Giro, G.; Biserni, M.; Mastragostino, M.; Testoni, A. *Synth. Met.* **1986**, *13* (4), 325–328.

(100) Wudl, F.; Kobayashi, M.; Heeger, A. J. *J. Org. Chem.* **1984**, *49* (18), 3382–3384.

(101) Sotzing, G. A.; Reynolds, J. R.; Steel, P. J. *Chem. Mater.* **1996**, *8* (4), 882–889.

(102) Dietrich, M.; Heinze, J.; Heywang, G.; Jonas, F. *J. Electroanal. Chem.* **1994**, *369*, 87–92.

(103) Patra, S.; Barai, K.; Munichandraiah, N. *Synth. Met.* **2008**, *158* (10), 430–435.

(104) Xiao, Y. M.; Lin, J. Y.; Wu, J. H.; Tai, S. Y.; Yue, G. T. *Electrochim. Acta* **2012**, *83*, 221–226.

(105) Poverenov, E.; Li, M.; Bitler, A.; Bendikov, M. *Chem. Mater.* **2010**, *22* (13), 4019–4025.

(106) Taggart, D. K.; Yang, Y.; Kung, S. C.; McIntire, T. M.; Penner, R. M. *Nano Lett.* **2011**, *11* (1), 125–131.

(107) Culebras, M.; Gómez, C. M.; Cantarero, A. *J. Mater. Chem. A* **2014**, *2* (26), 10109–10115.

(108) Crispin, X.; Marciniak, S. *J. Polym. Sci. Part B Polym. Phys.* **2003**, *41* (21), 2561–2583.

(109) Shi, K.; Zhang, F.; Di, C.-A.; Yan, T.-W.; Zou, Y.; Zhou, X.; Zhu, D.; Wang, J.-Y.; Pei, J. *J. Am. Chem. Soc.* **2015**, *137* (22), 6979–6982.

(110) Glaudell, A. M.; Cochran, J. E.; Patel, S. N.; Chabinyc, M. L. *Adv. Energy Mater.* **2015**, *5* (4), 1401072.

(111) Li, W.; Albrecht, S.; Yang, L.; Roland, S.; Tumbleston, J. R.; McAfee, T.; Yan, L.; Kelly, M. A.; Ade, H.; Neher, D.; You, W. *J. Am. Chem. Soc.* **2014**, *136* (44), 15566–15576.

(112) Li, W.; Yang, L.; Tumbleston, J. R.; Yan, L.; Ade, H.; You, W. *Adv. Mater.* **2014**, *26* (26), 4456–4462.

(113) Uy, R. L.; Yan, L.; Li, W.; You, W. *Macromolecules* **2014**, *47* (7), 2289–2295.

(114) Price, S. C.; Stuart, A. C.; Yang, L.; Zhou, H.; You, W. *J. Am. Chem. Soc.* **2011**, *133* (12), 4625–4631.

(115) MacDiarmid, A. G.; Epstein, A. J. *Faraday Discuss. Chem. Soc.* **1989**, *88*, 317.

(116) Sichel, E. K.; Rubner, M. F.; Tripathy, S. K. *Phys. Rev. B* **1982**, *26* (12), 6719–6726.

(117) Ray, A.; Asturias, G. E.; Kershner, D. L.; Richter, A. F.; MacDiarmid, A. G.; Epstein, A. J. *Synth. Met.* **1989**, *29* (1), 141–150.

(118) Loponen, M. T.; Taka, T.; Laakso, J.; Väkiparta, K.; Suuronen, K.; Valkeinen, P.; Österholm, J.-E. *Synth. Met.* **1991**, *41* (1-2), 479–484.

(119) Chun-Guey, W.; Mei-Jui, C.; Yii-Chung, L. *J. Mater. Chem.* **1998**, *8* (12), 2657–2661.

(120) Wang, Y.; Rubner, M. F. *Synth. Met.* **1990**, *39* (2), 153–175.

(121) Yuan, Y.; Giri, G.; Ayzner, A. L.; Zoombelt, A. P.; Mannsfeld, S. C. B.; Chen, J.; Nordlund, D.; Toney, M. F.; Huang, J.; Bao, Z. *Nat. Commun.* **2014**, *5*, 1–9.

(122) Tseng, H.-R.; Phan, H.; Luo, C.; Wang, M.; Perez, L. A.; Patel, S. N.; Ying, L.; Kramer, E. J.; Nguyen, T.-Q.; Bazan, G. C.; Heeger, A. J. *Adv. Mater.* **2014**, *26* (19), 2993–2998.

(123) Ma, J.; Hashimoto, K.; Koganezawa, T.; Tajima, K. *Chem. Commun.* **2014**, *50* (27), 3627–3630.

(124) Ma, J.; Hashimoto, K.; Koganezawa, T.; Tajima, K. *J. Am. Chem. Soc.* **2013**, *135* (26), 9644–9647.

(125) LaJoie, T. W. Conjugated Polymer Brushes as Molecular Wires in Electronic Devices: Synthesis, Device Design, and Characterization, The University of North Carolina at Chapel Hill, 2015.

(126) Loo, Y.-L.; Lang, D. V.; Rogers, J. A.; Hsu, J. W. P. *Nano Lett.* **2003**, *3* (7), 913–917.

(127) Jiang, W.; Garfunkel, E.; Zhitenev, N.; Abusch-Magder, D.; Tennant, D.; Bao, Z. *Appl. Phys. Lett.* **2006**, *89* (11), 113107.

(128) Delamarche, E.; Schmid, H.; Michel, B.; Biebuyck, H. *Adv. Mater.* **1997**, *9* (9), 741–746.

(129) Hui, C. Y.; Jagota, A.; Lin, Y. Y.; Kramer, E. J. *Langmuir* **2002**, *18* (4), 1394–1407.

(130) Meitl, M. A.; Zhu, Z.-T.; Kumar, V.; Lee, K. J.; Feng, X.; Huang, Y. Y.; Adesida, I.; Nuzzo, R. G.; Rogers, J. A. *Nat. Mater.* **2005**, *5* (1), 33–38.

(131) Feng, X.; Meitl, M. A.; Bowen, A. M.; Huang, Y.; Nuzzo, R. G.; Rogers, J. A. *Langmuir* **2007**, *23* (25), 12555–12560.

(132) Oh, D.-W.; Kim, S.; Rogers, J. A.; Cahill, D. G.; Sinha, S. *Adv. Mater.* **2011**, *23* (43), 5028–5033.

(133) Niskala, J. R. Molecular Spintronics: Design, Fabrication, and Characterization, 2010.

(134) Menard, E.; Bilhaut, L.; Zaumseil, J.; Rogers, J. A. *Langmuir* **2004**, *20* (16), 6871–6878.

(135) Simmons, J. G. *J. Appl. Phys.* **1963**, *34* (6), 1793–1803.

(136) Tuccitto, N.; Ferri, V.; Cavazzini, M.; Quici, S.; Zhavnerko, G.; Licciardello, A.; Rampi, M. A. *Nat. Mater.* **2009**, *8* (1), 41–46.

(137) Ho Choi, S.; Kim, B.; Frisbie, C. D. *Science* **2008**, *320* (5882), 1482–1486.

(138) Kokil, A.; Yang, K.; Kumar, J. *J. Polym. Sci. Part B Polym. Phys.* **2012**, *50* (15), 1130–1144.

(139) Valaski, R.; Bozza, A. F.; Micaroni, L.; Hümmelgen, I. A. *J. Solid State Electrochem.* **2000**, *4* (7), 390–393.

(140) Shi, H.; Liu, C.; Xu, J.; Song, H.; Lu, B.; Jiang, F.; Zhou, W. **2013**.

(141) Kim, K. S.; Zhao, Y.; Jang, H.; Lee, S. Y.; Kim, J. M.; Kim, K. S.; Ahn, J.-H.; Kim, P.; Choi, J.-Y.; Hong, B. H. *Nature* **2009**, *457* (7230), 706–710.

(142) Zang, J.; Cao, C.; Feng, Y.; Liu, J.; Zhao, X. *Sci. Rep.* **2014**, *4*, 6492.

(143) Sekitani, T.; Noguchi, Y.; Hata, K.; Fukushima, T.; Aida, T.; Someya, T. *Science* **2008**, *321* (5895), 1468–1472.

(144) Sekitani, T.; Nakajima, H.; Maeda, H.; Fukushima, T.; Aida, T.; Hata, K.; Someya, T. *Nat. Mater.* **2009**, *8* (6), 494–499.

(145) Khang, D.-Y.; Jiang, H.; Huang, Y.; Rogers, J. A. *Science* **2006**, *311*, 208–212.

(146) Siegel, A. C.; Bruzewicz, D. A.; Weibel, D. B.; Whitesides, G. M. *Adv. Mater.* **2007**, *19* (5), 727–733.

(147) Wei, B.; Ouyang, L.; Liu, J.; Martin, D. C. *J. Mater. Chem. B* **2015**.

(148) Feldman, K. E.; Martin, D. C. *Biosensors* **2012**, *2* (3), 305–317.

(149) Tanase, C.; Blom, P. W. M.; de Leeuw, D. M. *Phys. Rev. B* **2004**, *70* (19), 193202.

(150) Liu, C.; Jang, J.; Xu, Y.; Kim, H.-J.; Khim, D.; Park, W.-T.; Noh, Y.-Y.; Kim, J.-J. *Adv. Funct. Mater.* **2015**, *25* (5), 758–767.

(151) Wakamiya, A.; Nishimura, H.; Fukushima, T.; Suzuki, F.; Saeki, A.; Seki, S.; Osaka, I.; Sasamori, T.; Murata, M.; Murata, Y.; Kaji, H. *Angew. Chem. Int. Ed. Engl.* **2014**, *53* (23), 5800–5804.

(152) Li, R.; Jiang, L.; Meng, Q.; Gao, J.; Li, H.; Tang, Q.; He, M.; Hu, W.; Liu, Y.; Zhu, D. *Adv. Mater.* **2009**, *21* (44), 4492–4495.

(153) O'Connor, B. T.; Reid, O. G.; Zhang, X.; Kline, R. J.; Richter, L. J.; Gundlach, D. J.; DeLongchamp, D. M.; Toney, M. F.; Kopidakis, N.; Rumbles, G. *Adv. Funct. Mater.* **2014**, *24* (22), 3422–3431.

(154) Malen, J. A.; Doak, P.; Baheti, K.; Tilley, T. D.; Segalman, R. A.; Majumdar, A. *Nano Lett.* **2009**, *9* (3), 1164–1169.

(155) Chang, W. B.; Mai, C.; Kotiuga, M.; Neaton, J. B.; Bazan, G. C.; Segalman, R. A. *Chem. Mater.* **2014**, *26*, 7229–7235.

(156) Bergfield, J. P.; Solis, M. A.; Stafford, C. A. *ACS Nano* **2010**, *4* (9), 5314–5320.

(157) Hüser, F.; Solomon, G. C. *J. Phys. Chem. C* **2015**, *119* (25), 14056–14062.

(158) Tan, A.; Balachandran, J.; Dunietz, B. D.; Jang, S.-Y.; Gavini, V.; Reddy, P. *Appl. Phys. Lett.* **2012**, *101* (24), 243107.

(159) Lee, W.; Kim, K.; Jeong, W.; Zotti, L. A.; Pauly, F.; Cuevas, J. C.; Reddy, P. *Nature* **2013**, *498* (7453), 209–212.